Istituto Universitario
di Studi Superiori di Pavia

Università degli Studi
di Pavia

ROSE School

EUROPEAN SCHOOL OF ADVANCED STUDIES IN
REDUCTION OF SEISMIC RISK

SHAPE-MEMORY ALLOY DEVICES IN EARTHQUAKE ENGINEERING: MECHANICAL PROPERTIES, CONSTITUTIVE MODELLING AND NUMERICAL SIMULATIONS

A Dissertation Submitted in Partial
Fulfilment of the Requirements for the Master Degree in

EARTHQUAKE ENGINEERING

By

Davide Fugazza

Supervisors: Prof. Ferdinando AURICCHIO
Dr. Alberto PAVESE
Dr. Lorenza PETRINI

Pavia, September 2003

The dissertation entitled "Shape-Memory Alloy Devices in Earthquake Engineering: Mechanical Properties, Constitutive Modelling and Numerical Simulations", by Davide Fugazza, has been approved in partial fulfilment of the requirements for the Master Degree in Earthquake Engineering.

Ferdinando Auricchio ______________________________

Alberto Pavese ______________________________

Lorenza Petrini ______________________________

Contents

Abstract

Shape-memory alloys (SMAs) are a class of solids showing mechanical properties not present in materials usually employed in engineering.
SMAs have the ability to undergo reversible micromechanical phase transition processess changing their cristallographic structure. This capacity results in two major features at the macroscopic level which are the superelasticity and the shape-memory effect.

Due to these unusual characteristics, materials made of SMAs lend themselves to innovative applications in many scientific fields ranging from biomedical devices, such as stents or orthodontic archwires, to apparatus for the deployment and control of space structures, such as antennas and satellites.

Experimental and numerical investigations have also shown the possibility of using such smart new materials in vibration control devices. In particular, they seem to be an effective mean of improving the response of buildings and bridges subjected to seismic loads.

Despite the availability of a large number of mechanical tests conducted by many authors, few works deal with their constitutive modelling for earthquake engineering applications. Also, their dynamic response under high-frequency loading conditions would need further studies. As a consequence, the main aim of the present work is to cover this lack of information.

The main objectives of the present dissertation are the following:

- To present and comment the mechanical properties of SMA materials with emphasis on their response under dynamic loading conditions.
- To study the constitutive modelling of SMAs for seismic applications.
- To implement a robust uniaxial constitutive model for superelastic SMAs.
- To understand the influence of the SMA's mechanical properties on their dynamic behavior through parametric analyses.

The dissertation is organized in 5 Chapters and 3 Appendices as follows:

Chapter 1 overviews the main features of SMAs and introduces their unique characteristics. It also explains the reason for the increasing interest in such new materials through a survey of the most important applications nowadays exploited.

Chapter 2 proposes a state-of-the-art on the use of SMA-based devices in earthquake engineering. Besides a description of the mechanical behavior of such materials, a classification of the most promising applications is given.

Chapter 3 focuses on the constitutive modelling of SMAs. The section is aimed at presenting the uniaxial models traditionally used for simulating the seismic response of SMA-based devices. Advantages and drawbacks of each model are highlighted and discussed.

Chapter 4 presents a uniaxial consitutive law for SMAs together with its algorithmic implementation. Numerical simulations performed to check the model ability to describe complex loading conditions as well as comparisons with experimental data are shown.

Chapter 5 studies the dynamic behavior of SMAs. Parametric analyses conducted on single-degree-of-freedom systems are performed for the understanding of the material parameters' influence on the mechanical response.

Appendix A recalls some basic results of linear structural dynamics related to single-degree-of-freedom oscillators. Problems related to systems undergoing sinusoidal excitations as well as free-vibration motions are considered.

Appendix B reviews the main concepts of nonlinear structural dynamics. The Newton-Raphson strategy as well as the Newmark method for the numerical solution of the equation of motion are proposed.

Appendix C deals with some basic topics of earthquake engineering. Concepts like elastic and inelastic spectra are briefly revisited and some numerical application is also presented.

Aknowledgements

I would like to express my gratitude to Professor Auricchio for his invaluable suggestions and comments.

I want to thank Dr. Lorenza Petrini for her help and for carefully reading the manuscript many times as well as Dr. Alberto Pavese for serving as dissertation advisor.

Finally, special thanks go to my family and to my closest for their infinite support during these years.

Pavia, September 2003

Chapter 1

General Aspects of Shape-Memory Alloys

1.1 Introduction

In the 1960s Buehler and Wiley developed a series of nickel-titanium alloys, with a composition of 53 to 57% nickel by weight, that exhibited an unusual effect: severely deformed specimens of the alloys, with residual strain of 8-15%, regained their original shape after a thermal cycle.
This effect became known as the *shape-memory effect*, and the alloys exhibiting it were named *shape-memory alloys*[1].
It was later found that at sufficiently high temperatures such materials also possess the property of *superelasticity* (also named *pseudoelasticity*), that is, the recovery of large deformations during mechanical loading-unloading cycles performed at constant temperature.
Due to these distinctive macroscopic behaviors, not present in most traditional materials, SMAs are the basis for innovative applications, ranging from devices for the correction of tooth malpositions (orthodontic arch-wires) to self-expanding microstructures for the treatment of hollow-organ occlusions (stents), from micro-actuators to devices for protecting buildings from structural vibrations.

[1]In the following the notation SMA is used to substitute the term "shape-memory alloy".

1.2 General characteristics

The peculiar properties of SMAs are related to reversible martensitic phase transformations, that is, solid-to-solid diffusionless[2] processes between a crystallographically more-ordered phase, the *austenite*, and a crystallographically less-ordered phase, the *martensite*. Typically, the austenite is stable at lower stresses and higher temperatures, while the martensite is stable at higher stresses and at lower temperatures. These transformations can be either thermal-induced or stress-induced ([22], [29]).

At relatively high temperatures a SMA is in its austenitic state. It undergoes a transformation to its martensitic state when cooled. The austenite phase is characterized by a cubic crystal structure, while the martensite phase has a monoclinic (orthorombic) crystal structure.
The transformation from austenite to martensite occurs through a displacive distortion precess, which do not imply, however, macroscopic changes in the shape of the specimen. This is because several differently oriented plates of martensite, generally called *variants*, form within a single grain of austenite. The martensite variants are arranged in self-accomodating groups at the end of the thermal-induced transformation, thus keeping unchanged the specimen shape.

In the stress-free state, a SMA is characterized by four transformation temperatures: M_s and M_f during cooling and A_s and A_f during heating. The former two (with $M_s > M_f$) indicate the temperatures at which the transformation from the austenite (also named as *parent phase*) into martensite respectively starts and finishes, while the latter two (with $A_s < A_f$) are the temperatures at which the inverse transformation (also named as *reverse phase*) starts and finishes.

1.3 Shape-memory effect and superelasticity

When a unidirectional stress is applied to a martensitic specimen (see Figure 1.1), there is a critical value whereupon the *detwinning* process of the martensitic variants takes place ([22]). This process consists in the spatial re-orientation of the original martensitic variants, i.e. if there is a preferred direction for the occurrence of the transformation, often associated with a state

[2]Solid state transformations are of two types: diffusional and displacive. *Diffusional tranformations* are those in which a new phase can only be formed moving atoms randomly over relatively long distances. Long range diffusion is required because the new phase is of a different chemical composition than the matrix from which it is formed. In contrast, displacive transformations do not require such long range movements. In these cases atoms are cooperatively rearranged into a new, more stable crystal structure, but without changing the chemical nature of the matrix.

of stress, only the most favorable variant is formed. The product phase is then termed *single-variant martensite* and it is characterized by a detwinned structure. During such a process, the stress remains practically constant, until the martensite is fully detwinned (theoretically having a single variant aligned with the strain direction). Further straining causes the elastic loading of the detwinned martensite. Upon unloading, a large residual strain remains. However, by heating above A_f, martensite transforms into austenite and the specimen recovers its initial undeformed shape. This shape is kept during cooling below M_f, when the material re-transforms into twinned martensite. This phenomenon is generally named as *shape-memory effect*.

When a unidirectional stress is applied to an austenitic specimen (see Figure 1.2) at a temperature greater than A_f, there is a critical value whereupon a transformation from austenite to detwinned martensite occurs. As deformation proceeds in isothermal conditions, the stress remains almost constant until the material is fully transformed. Further straining causes the elastic loading of the detwinned martensite. Upon unloading, since martensite is unstable without stress at temperature greater than A_f, a reverse transformation takes place, but at a lower stress level than during loading so that a hysteretic effect is produced. If the material temperature is greater than A_f, the strain attained during loading is completely and spontaneously recovered at the end of unloading. This remarkable process gives rise to an energy-absorption capacity with zero residual strain, which is termed *superelasticity* (or *pseudoelasticity*). If the material temperature is less than A_f, only a part of stress-induced martensite re-transforms into austenite. A residual strain is then found at the end of unloading, which can be recovered by heating above A_f. This phenomenon is generally referred to as *partial superelasticity*.

1.4 Commercial shape-memory alloys

Despite the fact that many alloy systems show the shape-memory effect, only few of them have been developed on a commercial scale (NiTi, NiTi-X, Cu-Zn-Al) for engineering applications.
Accordingly, in this section, we want to discuss some of the characteristics exhibited by those alloys that, so far, have had the strongest impact in today's market: the nickel-titanium alloys and the copper-based alloys.

Nickel-titanium alloys

The *nickel-titanium*[3] (NiTi) system is based on the equiatomic compound of nickel and titanium ([32], [44], [46], [52], [53], [56]).
Besides the ability of tolerating quite large amounts of shape-memory strain, NiTi alloys show high stability in cyclic applications, possess an elevate electrical resistivity and are corrosion resistant. They also have a moderate solubility range, enabling changes in composition and alloying with other elements to modify both the shape-memory and their mechanical characteristics.
For commercial exploitation, and in order to improve its properties, a third metal is usually added to the binary system. In particular, a nickel quantity up to an extra 1% is the most common modification. This increases the yield strength of the austenitic phase while at the same time depressing the transformation temperatures.
Manifacture of NiTi alloys is not an easy task and many machining techniques can only be used with difficulty. This facts explains the reason for the elevated cost of such a system. Anyway, despite this disatvantage, the excellent mechanical properties of NiTi alloys have made them the most frequently used SMA material in commercial applications.

Copper-based alloys

Copper-Zinc-Aluminum (CuZnAl) alloys are the first copper-based SMAs to be commercially exploited ([4], [52], [56]).
This alloy originally comes from the copper-aluminium binary alloy, a system that, despite its shape-memory characteristics, has transformation temperatures considered too high for practical use.
CuZnAl alloys have the advantage that they are made from relatively cheap metals using conventional metallurgical processes. These reasons make them among the cheapest of the commercial SMAs available, especially when compared to the NiTi system.
The major drawback with these alloys is that the martensitic phase is stabilized by long term ageing at room temperatures. This causes an increase in transformation temperature over time and a decomposition of their structure when exposed to temperatures in excess of 100 ^oC.
Compared to other SMAs, CuZnAl alloys have modest shape-memory properties with a maximum recoverable strain of approximately 5%. Also, without the addition of grain growth control additives, their grain size can be quite large leading to brittleness problems.

[3]Sometimes the nickel-titanium alloy is called Nitinol (pronounced night-in-all). The name represents its elemental components and place of origin. The “Ni” and “Ti” are the atomic symbols for nickel and titanium. The “NOL” stands for the Naval Ordinance Laboratory where it was discovered.

Copper-Aluminum-Nickel (CuAlNi) alloys have undergone extensive development and are now preferred to CuZnAl alloys ([4], [52], [56]).
They are very popular for their wide range of useful transformation temperatures and because they are the only SMAs that can be used above 100 ^oC.
The aluminium percentage strongly influences the alloys' transformation temperatures and, the reduction of its content to below 12%, can also improve their mechanical properties.
Despite CuAlNi alloys are again made from relatively inexpensive elements, their processing is particularly difficult to machine. In fact, it can only be hot worked, and the final heat treatment has to be tightly controlled to produce an alloy with the desired transformation temperatures. These difficulties have made this system more expansive than CuZnAl even if it is still cheaper than nitinol.

1.5 Applications

As described in the above, SMAs have unique properties which are not present in many materials traditionally used in engineering applications. Accordingly, their use gives new possibilities of introduction on the market of innovative commercial products based on their particular characteristics.
The present section reviews, through practical examples, the most important applications exploiting both the superelastic behavior and the shape-memory effect ([1], [4], [29], [30], [32]).

Actuators

SMA materials have mainly been used for on/off applications such as cooling circuit valves, fire detection systems and clamping devices.
For instance, commercial on/off applications are available in very small sizes such as *miniature actuators*, which are devices electrically actuated.
SMAs offer important advantages in actuation mechanisms: simplicity, compactness and safety. They also create clean, silent, spark-free and zero gravity working conditions. High power/weight (or power/volume) ratios can be obtained as well. Anyway some drawback on the use of SMA actuators should be considered, such as the low energy efficiency and the limited bandwidth due to heating and cooling restrictions.

Adaptive materials and hybrid composites (smart materials)

The use of a *torsion tube* for trailing the edge trim tab control on helicopter rotors is a typical example of the smart blade technology whose main task is the attenuation of noise and vibrations in the surrounding environment.

Another interesting application is the *smart wing* for airplanes. For similar reasons as in the helicopter rotor blades, the shape of the wing should be adaptive, depending for example on the actual speed of the plane, and able to improve the overall efficiency.

Medicine and Biomechanics

A number of products that have been brought to the market use the superelastic property of SMAs. The most important ones are medical guidewires, stents and orthodontic devices.

The *medical guidewire* is a long, thin, metallic wire passed into the human body through a natural opening or a small incision. It serves as a guide for the safe introduction of various therapeutic and diagnostic devices. The use of superelastic alloys may reduce the complications of the guidewire taking a permanent kink, which may be difficult to remove from the patient without injury.

Stent is the technical word indicating self-expanding micro-structures, which are currently investigated for the treatment of hollow-organ or duct-system occlusions. The stent is initially stretched out to reach a small profile, which facilities a safe, atraumatic insertion of the device itself. After being released from the delivery system, the stent self-expands to over twice its compressed diameter and exerts a nearly constant, gentle, radial force on the vessel wall.

During orthodontic therapy tooth movement is obtained through a bone remodeling process, resulting from forces applied to the dentition. Such forces are usually created by elastically deforming an *orthodontic wire* and allowing its stored energy to be released to the dentition itself over a period of time.

Applications based on the high damping capacity of SMAs

A Swiss ski producer is testing composite skis in which *laminated strips* made of CuZnAl alloys are embedded. Those strips have the martensitic transformation temperatures slightly above 0 ^oC. Once in contact with snow, the ski will cool down while the CuZnAl elements will transform into martensite. In this way, vibrations will be damped significantly giving the skis a much better performance.

Recent experimental and numerical investigations have also shown the possibillity of using such smart materials in innovative devices for the protection of civil engineering structures, such as buildings and bridges, against earthquake-induced vibrations. *Intelligent bracing systems* for framed structures and new *restrainer cables* for bridge systems seem to be the most promising applications.

Fashion, decoration and gadgets

In this area some of the applications are: *eyeglass frames* (bow bridges and temples), *frames for brasseries* and *antennas* for portable cellular telephones. All these items realize their goals and comfort by using the superelastic behavior.

Apart from lingerie, NiTi alloys are also applied in other *clothing parts* as, for instance, the use of a superelastic wire as the core wire of a wedding dress petticoat, which can be folded into a compact size for storage and transport.

An elegant application is the *lamp shade*. A shape-memory spring heated by an electrical light opens a lamp shade. This simple mechanism creates a sticking elegant movement of the object.

Another invention (gadget) is a *cigarette holder* of an ash-tray that drops a burning cigarette into the ash-tray preventing it falling at the other side on a table cloth when left in the cigarette holder on the ash-tray.

Alloy type	**Composition**	**Temp. range** $[^oC]$	**Hyst.** $[^oC]$
Ag-Cd	44/49 at. % Cd	-190 to -50	15
Au-Cd	46.5/50 at. % Cd	30 to 100	15
Cu-Al-Ni	14/14.5 at. % Al 3/4.5 wt. % Ni	-140 to 100	35
Cu-Sn	$\approx$ 15 at. % Sn	-120 to 30	
Cu-Zn	38.5/41.5 wt. % Zn	-180 to -10	10
In-Ti	18/23 at. % Ti	60 to 100	4
Ni-Al	36/38 at. % Al	-180 to 100	10
Ni-Ti	49/51 at. % Ni	-50 to 110	30
Fe-Pt	$\approx$ 25 at. % Pt	-130	4
Mn-Cu	5/35 at. % Cu	-250 to 180	24
Fe-Mn-Si	32 wt. % Mn, 6 wt. % Si	-200 to 150	100

Table 1.1: Chemical characteristics of alloys exhibiting the shape-memory effect ([52]).

Melting temperature	1300	$[^oC]$
Density	6.45	[g/cm^3]
Resistivity austenite	$\approx$ 100	$[\mu\Omega\, cm]$
Resistivity martensite	$\approx$ 70	$[\mu\Omega\, cm]$
Thermal conductivity austenite	18	[W/(cm^oC)]
Thermal conductivity martensite	8.5	[W/(cm^oC)]
Corrosion resistance	similar to Ti alloys	
Elasticity Modulus austenite	$\approx$ 80	[MPa]
Elasticity Modulus martensite	$\approx$ 20 to 40	[MPa]
Yield strength austenite	190 to 700	[MPa]
Yield strength martensite	70 to 140	[MPa]
Ultimate tensile strength	$\approx$ 900	[MPa]
Transformation tmperature	-200 to 110	$[^o]$
Shape memory strain	8.5	[%]

Table 1.2: Properties of binary NiTi SMAs ([52]).

Alloy type	**CuZnAl**	**CuAlNi**	
Melting temperature	950 to 1020	1000 to 1050	[^oC]
Density	7.64	7.12	[g/cm^3]
Resistivity	8.5 to 9.7	11 to 13	[$\mu\Omega\, cm$]
Thermal conductivity	120	30 to 43	[W/(cm^oC)]
Elasticity Modulus austenite	72 (*)	85 (*)	[MPa]
Elasticity Modulus martensite	70 (*)	80 (*)	[MPa]
Yield strength austenite	350	400	[MPa]
Yield strength martensite	80	130	[MPa]
Ultimate tensile strength	600	500 to 800	[MPa]
Transformation temperature	$\leq$ 120	$\leq$ 200	[^oC]
Shape memory strain	4	4	[%]

Table 1.3: Properties of copper-based SMAs ([52]). (*) The modulus of elasticity of SMAs becomes difficult to define between the M_s and the A_s. In fact, at these temperatures, the alloys exhibit nonlinear elasticity and the modulus is both temperature and strain dependent.

Property	**NiTi SMA**	**Steel**
Recoverable elongation [%]	8	2
Modulus of elasticity [MPa]	8.7x10^4 (A), 1.4x10^4 (M)	2.07x10^5
Yield strength [MPa]	200-700 (A), 70-140 (M)	248-517
Ultimate tensile strength [MPa]	900 (f.a.), 2000 (w.h.)	448-827
Elongation at failure [%]	25-50 (f.a.), 5-10 (w.h.)	20
Corrosion performace	Excellent	Fair

Table 1.4: Comparison of NiTi SMA properties with typical structural steel. Letters A and M stand for, respectively, austenite and martensite while abbreviations f.a. and w.h. respectively refer to the names “fully annealed” and “work hardened” which are two types of treatment ([14]).

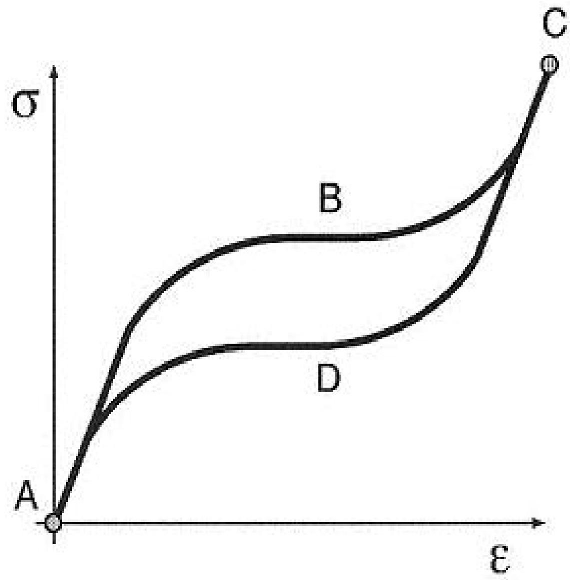

Figure 1.1: Superelastic effect. At a constant high temperature the material is able to undergo large deformations with zero final permanent strain. Note the hysteresis loop.

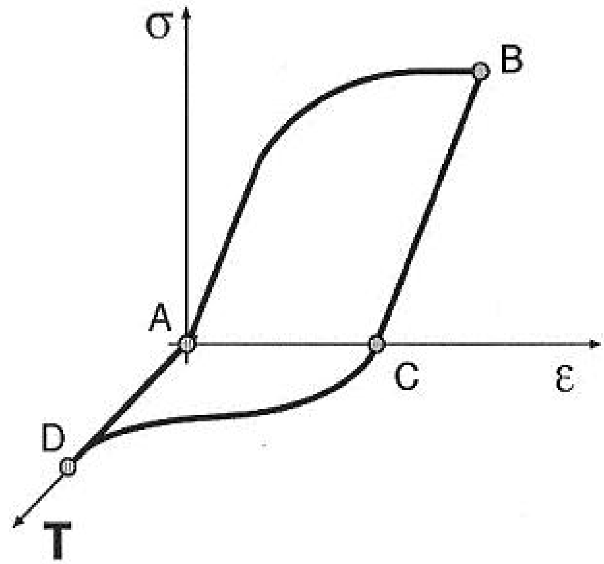

Figure 1.2: Shape-memory effect. At the end of a mechanical loading-unloading path (ABC) performed at a constant low temperature, the material presents residual deformation (AC), which can be recovered through a thermal cycle (CDA).

Chapter 2

Use of Shape-Memory Alloy Devices in Seismic Engineering

2.1 Introduction

In this Chapter we discuss the use of SMA devices in earthquake engineering. First, we propose an overview on the mechanical behavior of SMA elements, such as wires and bars, under static and dynamic loading conditions, then we present a state-of-the-art of the most promising investigations performed on SMA-based devices during the last years. Finally, we give two examples of existing structures seismically upgraded by using SMAs.

2.2 Mechanical behavior of SMA elements

Before a description of the mechanical behavior of SMA elements under static and dynamic loadings, we recall the meaning of some significant quantities usually employed in earthquake engineering to characterize the dissipation capability of the material under investigation. They are: the energy loss per cycle, the energy loss per unit weight, the maximum potential energy, the loss factor, the secant stiffness and the equivalent viscous damping. For additional details and examples of computation, the reader may refer to references [10], [11], [20] and [50].

- The *energy loss per cycle* is evaluated as the average area of the hysteresis loops with the same amplitude.
- The *energy loss per unit weight* is obtained by dividing the energy loss per cycle by the weight of the specimen. It expresses the effectiveness of the specimen in terms of energy dissipation capability.
- The *maximum potential energy* for a linear viscoelastic material with low damping is equal to $U = \frac{1}{2}\,\epsilon_{max}\,\sigma_{max}$, being ϵ_{max} and σ_{max} the maximum

strain and stress respectively. Anyway, for a nonlinear material, a more precise definition is given by $U = W - \frac{1}{2}\Delta W$ being W the maximum strain energy at ϵ_{max} (see Figure 2.1) and $\frac{1}{2}\Delta W$ the energy dissipated up to this point.

- The *loss factor* is defined by the relatioship $\eta = (1/2\pi)(2\,\Delta W/U)$. The value 2 at the numerator is justified by the fact that in cycling loadings the total dissipated energy is equal to twice the energy dissipated in tension only.

- The *secant stiffness* is computed through the expression $K_s = (F_{max} - F_{min})/(\delta_{max} - \delta_{min})$ where F_{max} and F_{min} are the forces attained for the maximum cyclic displacements δ_{max} and δ_{min}.

- The *equivalent viscous damping* expresses the effectiveness of the material in vibration damping. It is provided by the formula $\xi_{eq} = W_D/\,(2\pi\,K_s\,\delta^2)$ where W_D is the energy loss per cycle and δ is the maximum cyclic displacement under consideration.

The mechanical behavior of SMA elements, such as wires and bars, has been studied by many authors ([39], [45], [50], [54], [55], [57], [61]) in order to understand the response of such elements under various loading conditions.
In the following we present a bibliographical review of the most recent experimental investigations. Without the claim of being exhaustive, we focus only on papers dealing with a material characterization, useful before discussing the use of SMAs in earthquake engineering.

Lim and McDowell ([39]) analyze the path dependance of SMA during cycling loadings through experimental tests performed on 2.54 mm diameter wires. In particular they focus the attention on both the cyclic uniaxial tension behavior and the cyclic uniaxial tension-compression behavior. The most significant results they find are:

1. Under condition of cycling loading with a maximum imposed strain, the critical stress to initiate stress-induced martensite transformation decreases, the strain-hardening rate increases, residual strain accumulates and the hysteresis energy progressively decreases over many cycles of loading.

2. The stress at which either forward or reverse transformation occurs depends on the strain level prior to the last unloading event. This behavior is attributed to the distribution and configuration of austenite-martensite interfaces which evolve during transformation.

Moroni et al. ([45]) try to use copper-based SMAs as energy dissipation devices for civil engineering structures. Their idea is to design a new efficient beam-column connection incorporating those smart materials. They perform cyclic tension-compression tests on martensitic bars, with a diameter of 5 and 7 mm, characterized by different processing hystories (hot rolled or extrusion) and grain size composition. The experimental investigation is conducted both in strain and stress control at different frequencies of loading (from 0.1 to 2 Hz). On tha basis of the results, the researchers draw the following major conclusions:

1. The martensitic CuZnAlNi alloy dissipates substantial energy through repeated cycling then highlighting a possibile use as material able to dissipate seismic energy.
2. Damping is a function of strain amplitude and it tends to stabilize for large strains. Also, frequency (0.1-2 Hz) has a small influence on the damping values.
3. The considered mechanical treatments (rolling and extrusion) do not influence the bars' mechanical behavior.
4. Observed fractures are due to tensile actions and present a brittle intergranular morphology.

Piedboeuf and Gauvin ([50]) study the damping behavior of SMA wires. They perform more than 100 experiments on 100 μm diameter NiTi wires at three levels of amplitudes (2, 3 and 4% of strain), over four frequency values (0.01, 0.1, 1, 5 and 10 Hz) and at two different temperatures (25 and 35 ^{o}C). The main findings the researchers carry out are:

1. An increase in temperature causes a linear increase in transformation stresses and a shift of the stress-strain curves upward.
2. Up to a frequency of 0.1 Hz and for a fixed value of deformation of 4%, the stress difference between the two plateaus increases, producing an increase in the stress hysteresis and also in the dissipated energy. For higher frequencies, instead, the lower plateau deforms and rises causing a pronounced reduction of the hysteresis loop.
3. Frequency interacts with the deformation amplitude. In particular at 2% deformation, there is only a slight variation in the dissipated energy by varying frequency while, at 4%, the variation is more important and the maximum occurs at around 0.1 Hz. For higher values of frequency the dissipated energy decreases.
4. The loss factor decreases with an increase in temperature which, anyway, has no significant effect on the dissipated energy.

Strnadel et al. ([54]) test both NiTi and NiTiCu thin plates in their superelastic phase. Their study is mainly aimed at evaluating the cyclic stress-strain characteristics of the selected alloys. They also devote particular attention to the effect of the variation of the nickel content in the specimens' mechanical response. Interesting apects that the research group points out are:

1. Ternary NiTiCu alloys display lower transformation deformations and transformation stresses than binary NiTi alloys.
2. In both NiTi and NiTiCu alloys the higher the nickel content is, the lower is the growth rate of the residual deformation as the number of cycles increases.

Tamai et al. ([55]) observe the behavior of 1.7 mm diameter superelastic NiTi wires for a possible use of SMAs as brace and exposed-type column base for building structures. The experimental investigation consists of both monotonic and pulsating tension loading tests performed with constant, increasing and decreasing strain amplitudes, at a stroke speed of the test machine mantained equal to $0.074\% \cdot \mathrm{sec}^{-1}$ throughout all the expriments. As a result the observations they make are the following:

1. A spindle shaped hysteresis loop is observed showing a great deal of absorbed energy.
2. The stress which starts the phase transformation is very sensitive to ambient temperature. Further, wire temperature does vary during cyclic loading due its latent heat.
3. The residual deformation increment and dissipated energy decrement per cycle decreases with the number of loading cycles.
4. The rise and fall of the wire temperature during forward and reverse transformation have almost the same intensity. In particular forward transformation is exothermal whereas, conversely, reverse transformation is endothermal.

Tobushi et al. ([57]) investigate the influence of the strain rate (i.e. $\dot{\epsilon}$) on the superelastic properties of 0.75 mm diameter superelastic wires through tensile tests, conducted at strain rates ranging from $1.67 \cdot 10^{-3}\% \cdot \mathrm{sec}^{-1}$ to $1.67\% \cdot \mathrm{sec}^{-1}$. They also take into account the effects of the temperature variation on the wires's mechanical response. Their main considerations are:

1. When $\dot{\epsilon} \geq 1.67 \cdot 10^{-1}\% \cdot \mathrm{sec}^{-1}$, the larger $\dot{\epsilon}$ is, the higher is the stress at which the forward transformation starts and the lower is the stress at which the reverse transformation starts.

2. For each temperature level considered, the larger $\dot{\epsilon}$ is, the larger is the residual strain after unloading. Also, the higher the temperature is, the larger is the residual strain.

3. As the number of cyclic deformation increases, the stress at which forward and reverse transformation start decreases with a different amount of variation. Also the irrecoverable strain which remains after unloading increases.

4. For each temperature level considered, each transformation stress is almost constant for $\dot{\epsilon} \leq 3.33{\cdot}10^{-2}\% \cdot \sec^{-1}$. For $\dot{\epsilon} \geq 1.67{\cdot}10^{-1}\% \cdot \sec^{-1}$, instead, the the upper plateau stress level at which the forward transformation starts increases, while the one correlated to the lower plateau decreases with a lower amount of variation. The same trend is also observed when the wire has been subjected to mechanical training.

5. The strain energy increases with an increase in temperature, while the dissipated work slightly depends on the temperature variation. Also, at each temperature level, it is observed that both quantities do not depend on the strain rate for values of $\dot{\epsilon} \leq 3.33{\cdot}10^{-2}\% \cdot \sec^{-1}$. Instead, for values of $\dot{\epsilon} \geq 1.67{\cdot}10^{-1}\% \cdot \sec^{-1}$, the dissipated work increases and the strain energy decreases linearly.

Wolons et al. ([61]) test 0.5 mm diameter superelastic NiTi wires in order to understand their damping characteristics. They study in very great detail the effect of cycling, oscillation frequency (from 0 to 10 Hz), temperature level (from about 40 ^{o}C to about 90 ^{o}C) and static strain offset (i.e. deformation from which the cycling deformation starts). On the basis of the experimental data they observe that:

1. A significant amount of mechanical cycling is required for an SMA wire to reach a stable hysteresis loop shape. The amount of residual strain is dependent on both temperature and strain amplitude, but it is not a function of the cycling frequency.

2. The shape of hysteresis loop changes significantly with frequency. The reverse transformation from detwinned martensite to austenite is affected more than the forward transformation.

3. Energy dissipation is a function of frequency, temperature, strain amplitude and static strain offset (chosen in the range 2.9 to 4.7 %). The energy dissipated per unit volume initially decreases up to 1-2 Hz, then appears to approach a stable level by 10 Hz. Dissipation capacity at 6-10 Hz is about 50% lower than the corresponding one at very low frequencies. Moreover, it decreases as temperature increases above 50 ^{o}C.

4. By reducing the static strain offset the energy dissipated per unit volume increases.

5. Energy dissipation per unit volume of SMA wires undergoing cyclic strains at moderate strain amplitudes (about 1.5 %) is about 20 times bigger then typical elastomers undegoing cyclic shear strain.

DesRoches et al. ([16]) perform several experimental tests on NiTi superelastic wires and bars to assess thier potentiality for applications in seismic resistant design and retrofit. In particular, they study the effects of the cycling loading on the residual strain, forward and reverse transformation stresses and energy dissipation capability. Specimens are different in diameters (1.8, 7.1, 12.7 and 25.4 mm respectively) with nearly identical composition. The loading protocol is made of increasing strain cycles of 0.5%, 1% to 5% by increments of 1%, followed by four cycles at 6%. The research group considers two series of tests. The first one, in quasi-static condition, is performed at a frequency of 0.025 Hz while the second one is conducted at frequencies of 0.5 and 1 Hz in order to simulate dynamic loads. After carrying out the experiments, they propose the following observations:

1. Nearly ideal superelastic properties are obtained in both wires and bars. The residual strain generally increases from an average of 0.15% following 3% strain to an average of 0.65% strain following 4 cycles at 6% strain. It seems to independent on both the section size and the loading rate.

2. Values of equivalent damping range from 2% for the 12.7 mm bars to a maximum of 7.6% for the 1.8 mm wires and are in agreement with the values found by other authors ([18], [20]). Bars show a lower dissipation capability than wires.

3. Value of stress at which forward transformation starts when testing bars, is lower by about 30% in than the corresponding value in wires.

2.3 The Project MANSIDE (1995-1999)

As discussed in the previous section, many authors have carried out experimental tests on SMA elements but few of them have focused the attention on SMA devices subjected to earthquake-like or, more in general, dynamic loading conditions. For this reason we now prefer giving a summary of the results found out during the Project MANSIDE (1995-1999), a project co-funded by the European Commission within the Brite-Euram III Programme, aimed at the development and experimental validation of new seismic protection devices based on the properties of SMAs ([5], [9], [21], [49], [29], [59]).
Among its tasks, the most important ones were:

1. Study of SMA components for new devices fully exploiting the superelasticity and the high damping capability of such smart materials.

2. Design and testing of prototypes (seismic isolators and dissipating braces).

3. Proposal of guidelines for the design and utilization of new SMA-based devices, including reliability requirements.

In the following, we present a summary of the experimental investigations carried out during the project. After a description of each test, we propose both the final results and a discussion listing advantages and disadvantages on the use of SMAs as new materials for the mitigation of the seismic risk.

2.3.1 Tests on Martensite and Austenite NiTi bars

Dolce and Cardone ([18], [19]) investigate the mechanical behavior of several NiTi SMA bars through a large experimental test program. The SMA elements are different in size (bars with different diameters), shape (round and hexagonal bars) and physical characteristics (alloy composition, thermomechanical treatment and material phase). The experimental results are carried out by applying repeated cyclic deformations: strain rate, strain amplitude, temperature and number of cycles are considered as test parameters, and their values are selected taking into account the typical range of interest for seismic applications. SMA bars have a diameter of 7-8 mm (small size bars) and 30 mm (big size bars) and the research group devotes special attention on big size bars, being the most likely candidates for full scale seismic devices.
In the following a summary of all the tests performed on the specimens: the typical test sequence is characterized in terms of frequency (f), strain amplitude (γ) and number of cycles (n).

Torsional tests on martensite specimens

All experimental tests are carried out at room temperature ($\approx 25\ ^{o}$C) on only one big size martensite specimen in the order herein presented. Frequency of loading ranges from 0.01 to 1 Hz. Up to 24% maximum nominal tangential strain is attained:

- *Tests in normal working conditions*: four groups of cycles at 0.01, 0.1, 0.5 and 1 Hz, respectively, each group being made of 4 times 10 consecutive cycles, with γ equal to 3%, 6%, 9% and 11%. The aim is to evaluate the cyclic behaviour of the specimen as a function of strain rate and amplitude.

- *Fatigue tests*: groups of up to 1650 cycles, at 0.5 Hz and γ equal to 11%. The aim is to verify the fatigue behaviour, in terms of decay and resistance, of the specimen.

- *Tests in normal working conditions*: two groups of cycles at 0.1 and 0.5 Hz, respectively, each group being made of 4 times 10 consecutive cycles, with γ equal to 3%, 6%, 9% and 11%. The aim is to check the mechanical behaviour after the big number of cycles undergone by the specimen during the fatigue tests.
- *Test at very large strain amplitude*: one test at 0.1 Hz, made of 4 times 10 cycles with γ equal to 15%, 18%, 21%, 24%. The aim is to evaluate the cyclic behaviour of the specimen under extreme strain amplitude conditions.
- *Fatigue tests*: groups of 100 cycles, at 0.5 Hz and γ equal to 15% or 18%. The aim is to verify the fatigue resistance of the specimen under extreme strain amplitude conditions.

Torsional tests on austenite specimens

The tests are carried out on one big size austenite specimen at room temperature ($\approx$ 25 ^{o}C), frequencies of loading ranging from 0.01 to 1 Hz and cyclic amplitude up to 11% nominal tangent strain (γ) in the order herein presented:

- *Tests in normal working conditions*: four group of cycles at 0.01, 0.1, 0.5 and 1 Hz, respectively, each group being made of 4 times 10 consecutive cycles, with γ equal to 3%, 6%, 9% and 11%. The aim is to evaluate the cyclic behaviour of the specimen as a function of the strain rate and amplitude.
- *Fatigue tests*: two groups of several cycles (100 the first group, up to failure the second one), at 0.5 Hz and γ equal to 11%. The aim is to verify the fatigue behaviour, in terms of decay and resistance, of the specimen.
- *Tests in normal working conditions*: two groups of cycles at 0.1 and 0.5 Hz respectively, each group being made of 4 times 10 consecutive cycles, with γ equal to 3%, 6%, 9% and 11%. The aim is to check the mechanical behaviour after the big number of cycles undergone by the specimen during the fatigue test.

Results and final considerations

The most important findings of the experimental investigation can be summarized as follows:

1. The mechanical behaviour of SMA bars subjected to torsion is independent from frequency of loading in case of martensite elements, or slightly dependent on it in case of austenite elements.

2. The energy loss per unit weight increases more than linearly while increasing strain amplitude reaching, at relatively large strain amplitudes, values of the order of 0.5 J/g for martensite bars and of the order of 0.25 J/g for austenite bars.

3. The effectiveness in damping vibrations is good for martensite (up to 17% in terms of equivalent damping), but rather low for austenite (of the order of 5-6% in terms of equivalent damping).

4. Austenite bars present negligible residual deformations at the end of the action, being of the order of 10% of the maximum attained deformation.

5. The fatigue resistance under large strains is considerable for austenite bars (hundreds of cycles) and extraordinary for martensitic bars (thousands of cycles). In both cases, the cyclic behaviour is highly stable and repeatable, after the possible initial stabilization.

As a final result, the experimental tests prove that SMA bars subjected to torsion have a good potential for their use as kernel components in seismic devices. Martensite bars can provide large energy dissipation and outstanding fatigue resistance capabilities. Austenite bars, though having less energy dissipation capability, can undergo very large strains without any residual, conditioned upon a correct calibration of the transformation temperatures with respect to the operating temperature. The two different types of behaviour can be finalized at obtaining differently performing devices satisfying different needs in seismic protection problems.

2.3.2 Tests on Austenite NiTi wires

Within the same research program Dolce and Cardone ([19]) study the mechanical behavior of NiTi superelastic wires subjected to tension. The experimental tests are carried out on austenite wire samples with 1-2 mm diameter and 200 mm length. Several kinds of wires are considered, differing in alloy composition and/or thermomechanical treatment.
First of all, cyclic tests on pre-tensioned wires at room temperature ($\approx 20\ ^{o}$C), frequency of loading ranging from 0.01 to 4 Hz and strain amplitude up to 10% are performed. Subsequently, loading-unloading tests under temperature control, between 40 ^{o}C and 10 ^{o}C (step 10 ^{o}C), at about 7% strain amplitude and 0.02-0.2 Hz frequency of loading are conducted.
The authors deply investigate the superelastic behaviour, focusing on the dependence of the mechanical properties on temperature, loading frequency and number of cycles. The mechanical behaviour is described by means of four fundamental quantities, namely: secant stiffness, energy loss per cycle, equivalent damping and residual strain.

Results and final considerations

The most important results of the experimental tests can be summarized as follows:

1. The dependence on temperature of the tested materials appears compatible with the normal range of ambient temperature variations, if this is assumed to be of the order of 50 ^{o}C.

2. Loading frequency affects the behaviour of SMAs, especially when passing from very low frequency (0.01 Hz or even less) to the frequency range of interest for seismic applications (0.2-4 Hz). A considerable decrease of energy loss and equivalent damping occurs because of the increase of temperature. This is due to the latent heat of transformation which cannot be dissipated in case of high strain rates.

3. The number of undergone cycles considerably affects the superelastic behaviour of austenitic SMAs, worsening the energy dissipating capability and increasing the cyclic strain hardending.

4. A general consideration regards the low equivalent damping of the typical loading-unloading cycle of an austenite wire. This results in a better performance of SMAs when used in a recentring mechanism[1].

As a final conclusions, it is possible to state that the experimental results show how the characteristics of the superelastic wires are well suited for seismic applications, and that both the recentring and energy dissipating features of the devices can be easily obtained.
The cyclic behavior of superelastic wires is found to be stable after few cycles, whose number is of the same order as the number of cycles that would be experienced during an earthquake. To get a stable response, then, a device should be subjected to a pre-established initial training which, for example, could be a part of the testing programme for the qualification of the acceptance of the device. An alternative strategy could rely on the better energy dissipation properties of the virgin material, and then avoiding or limiting any preliminary training of the device before its use in a structural system.

2.4 Numerical tests on SMA-based devices

Among the huge literature dealing with SMA materials, few authors ([3], [8], [14], [15], [17], [60]) study the seismic behavior of civil engineering structures, such as frames and bridges, endowed with SMA-based devices.
In the following we present a review of the numerical applications where such

[1] With the term *recentring mechanism*, we mean a device with the ability to bring the structure back to its undeformed shape after the external solicitation is over.

new materials are used as both vibration control devices ([3], [8]) and isolation systems ([14], [15], [17], [60]).

Baratta and Corbi ([3], [13]) investigate the influence of SMA tendon elements collaborating to the overall strength of a simple portal frame model (see Figure 2.2) undergoing horizontal shaking. The basic structure they study, is assumed to exhibit a elastic-perfectly plastic material behaviour, while the tendons are supposed to behave according to a pseudoelastic model.
The performance of such a system is compared with the response of a similar structure, where the tendons are supposed to be fully elastic-plastic, as the main structure, or, alternatively, unilaterally plastic, i.e. unable to sustain compression forces, as in the case the tendons were slender.
The numerical results show that the structure endowed with pseudoelastic tendons decisively improve the dynamic response with respect to the case in which the tendons are made by elastic-plastic wires. In fact, in both cases, SMA tendons produce smaller maximum amplitude of the response and much smaller residual drift. Such a device yields an excellent performance in attenuation the P-Δ effect as well.

Bruno and Valente ([8]) present a comparative analysis of different passive seismic protection strategies, aiming at quantifying the improvement achievable with the use of innovative devices based on SMAs in place of traditional steel or rubber devices (i.e. bracing and base isolation systems).
To this end, the research group performs a large number of nonlinear seismic analyses augmenting the seismic intensity level. The structural typology they study is characterized by an appropriate structural scheme to be effectively protected either with base isolation or dissipation braces. They examine new and existing buildings, either protected or not, depending on whether seismic provisions are complied with in the building design or not. Base isolation and energy dissipation are equally addressed for both conventional and innovative SMA-based design.
As concerns the comparison between conventional and innovative devices, the researchers find that SMA-based devices are far more effective than rubber isolators in reducing seismic vibrations. On the other hand, the same conclusions cannot be drawn for SMA braces if compared to steel braces. Actually, in this latter case, the reduction of the structural response can be considered identical from a practical point of view. Anyway, the SMA braces prove preferable considering the recentring capabilities not possessed by the steel braces.
Furthermore, the use of such new smart systems, brings about better performances in the consideration of the reduced functional and maintenance requirements.

DesRoches at al. ([14], [15], [17]) consider the application of SMA restrainers to a multi-span bridge. The structure they study (see Figures 2.3 and 2.4)

consists of three spans supported on multi-column bents. Each bent has four columns and each span has 11 girders. The concrete slabs are supported by steel girders resisting on elastomeric bearings. The SMA restrainers (see Figure 2.5) are connected from the pier cap to the bottom flange of the beam in a manner similar to typical cable restrainers. They are used in a tension-only manner and they might be employed to act in both tension and compression by providing an adequate lateral bracing device.
The results they obtain show that the SMA restrainers reduce relative hinge displacements at the abutment much more effectively than conventional steel cable restrainers. The large elastic strain range of the SMA devices allows them to undergo large deformations while remaining elastic. In addition, the superelastic properties of the SMA restrainers result in energy dissipation at the hinges. Also, for unexpexted strong earthquakes, the increased stiffness they can provide at large strains, guarantees additional restraint to limit the relative openings in the bridge.

Wilde et al. ([60]) propose a smart isolation system which combines a laminated rubber bearing (LRB) with a device made of SMA bars.
In their study the authors consider the simplest configuration of the SMA device which consists of a set of two bars working in tension and compression attached to the pier and the superstructure. The design of the SMA device is performed on the Kobe earthquake record scaled to different amplitudes.
The SMA bars combined with a laminated rubber bearing can provide a damper with the desired variable characteristics based solely on the material properties of the alloy. Furthermore, the proposed device has an inherent centring ability due to superelastic behaviour of SMAs.
The new isolation system provides stiff connection between the pier and the deck for small external loading, while, for a medium size earthquake, the SMA bars increase the damping capacity of the isolation due to stress-induced martensitic transformation of the alloy. Also, for the largest considered earthquake, the SMA bars provide hysteretic damping and, in addition, act as a displacement controlling device due to hardening of the alloys after completeness of the phase transformation.
The researchers also compare the performance of the new proposed smart isolation system with the corresponding one of a conventional isolation system consisting of a lead LRB with an additional stopper device. Numerical tests show that the damage energy of the bridge endowed with the SMA isolation system is small although the input energy to the structure is large compared to a bridge isolated with LRB. Possible drawback is the need of additional devices to prevent the possible buckling of the long SMA bars used.

2.5 Experimental tests on SMA-based devices

In the following we present and discuss the most interesting experimental tests carried out on structures equipped with SMA-based devices. Basically we focus the attention on smart connections ([15], [48]) and brace systems for framed structures ([8], [20], [21], [26]) which seem to be the most promising applications in the field of earthquake engineering.

DesRoches at al. ([15], [48]) investigate the effectiveness of various types of partially-restrained connections as an alternative to fully restrained welded connections. As an extension to that research, they explore the use of innovative materials in connections. Their study look at the behaviour of a beam-column joint equipped with SMA tendons exhibiting the shape-memory effect (see Figure 2.7). The connection consists of a W24x94 beam connected to a W14x159 column. Four 381 mm long SMA tendons are threaded into anchorages specially designed to allow the tendons to resist load in both tension and compression. The tendons, circular 34.9 mm rods, are connected to the column from the top and bottom flanges of the beam, whose anchorage includes two rectangular tubes welded on three sides with a fillet to the beam flange. The research group tests the connection on a specially designed shear tab at increasing cycles up to 4% drift, showing the obtained stable and repeatable behaviour with significant energy dissipation. Following the test series, the SMA tendons are then reheated beyond their transformation temperature, and retested. The tendons are able to recover 80% of their original shape and the connection presents nearly identical behaviour to the first testing series.

Bruno and Valente ([8]), Dolce et al. ([20], [21]) study in very great detail the possibility of using special braces for framed structures employing SMA-based devices (see Figure 2.6). In fact, due to their extreme versatility, it is possible to obtain a wide range of cyclic behaviour (from supplemental and fully re-centring to highly dissipating) by simply varying the number and/or the characteristics of the SMA components. In particular they propose three categories of devices which are selected, designed, constructed and tested:

- *Supplemental re-centring devices (SRCD)*: typically based on the recentring group only, they present zero residual displacement at the end of the action and further capability to provide an auxiliary re-centring force, which compensates possible reacting forces external to the device, such as friction of bearings (for isolation system) or plastic forces of structural elements (for bracing systems).

- *Not re-centring devices (NRCD)*: based on the dissipating group only, they present large dissipation capabilities but also large residual displacement at the end of the action.

- *Re-centring devices (RCD)*: including both re-centring devices and dissipating group, they present zero or negligible residual displacement, but are not capable to recover the initial configuration if reacting forces external to the device exist.

The idea of using a SMA bracing system as damper device for the structural vibration control of a frame is also studied by Han at al. ([26]).
They carry out an experimental test on a two-storey steel frame installed with eight SMA dampers. The dimension of the structure are 2 m high, 1 m long and 0.25 m wide, loaded vertically with four blocks of 20 Kg each (two per floor). Each damper consists of one SMA wire (0.75 mm diameter) connected between two steel wires (7 mm diameter). The steel wire is 582 mm long and the SMA wire is 250 mm long. The researchers mainly focus the tests on the vibration decay history shown by the frame with and without the SMA dampers. It turns out that the uncontrolled frame (i.e the frame without the damper) takes about 45 seconds to reduce its initial displacement of 50%, while it tooks about 1 second when equipped with the damper. Finally, they perform finite element analyses of both the uncontrolled and controlled frame subjected to the El Centro ground motion, to show the effectiveness of the SMA damper in reducing the dynamic response of the structure.

2.6 Existing applications of SMA devices for seismic rehabilitation

SMAs as new materials for the seismic protection of structures, have also been used for the rehabilitation of monuments and historical buildings.
We now discuss two of the first known applications of SMA-based devices in existing structures, referring to the cases of the seismic upgrading of the Basilica of San Francesco in Assisi and of the bell tower of the church of San Giorgio in Trignano, two very old constructions both built in Italy.

The Basilica of San Francesco in Assisi ([42]) was severely damaged during the 1997 Umbria-Marche earthquake. The main challenge of the restoration was to obtain an adequate safety level, while mantaining the original concept of the structure. In order to reduce the seismic forces transferred to the tympanum, a connection between it and the roof was created using superelastic SMAs (see Figure 2.8). The SMA devices have demonstrated different structural properties for different horizontal forces. Under low horizontal forces they are stiff and allow for no significant displacements, under high horizontal actions, such as an earthquake, their stiffness reduces for controlled displacements of the masonry walls whereas under extremely intense horizontal loads their stiffness increases to prevent collapse.

Among other interventions, the one carried out on the bell tower of the church of San Giorgio in Trignano is worth mentioning ([17]).
The structure is very old (XIV century), it is made of masonry and it was seriuosly damaged during the 1996 Modena and Reggio Emilia earthquake.
The tower is 18.5 m high and has a square base with 3 m edge. It is surrounded on three edges by others buildings up to the height of 11 m. The masonry walls are 0.42 m thick close to the corners and 0.3 m in the central part. Four large windows closed using thin brick walls are present at 13 m level. Thus the corresponding section results quite weak and in fact it breaked during the seimic event. Following the earthquake, the tower was rehabilitated using SMAs. Four vertical prestressing steel bars in series with SMA devices (see Figure 2.9) were placed in the internal corners of the bell tower to increase its flexural strength. The smart devices were made up of 60 wires, 1 mm in diameter and 300 mm in length, anchored at the top and bottom of the tower, with the aim of limiting the forces applied to the masonry.

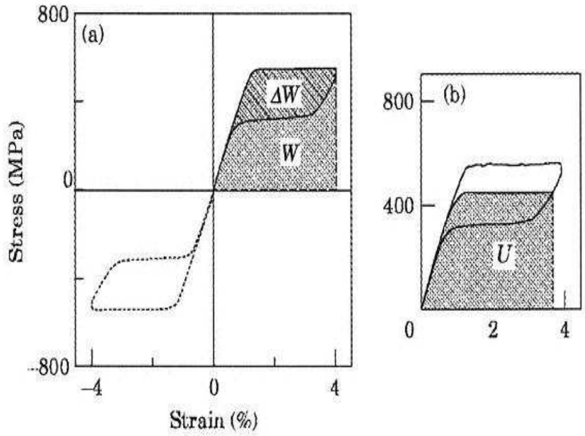

Figure 2.1: Superelastic effect in tension (continuous line) and in compression (dashed line): (a) ΔW and W are respectively the dissipated energy and the maximum strain energy in a tensile loading-unloading test while (b) U is the maximum potential energy in a tension-compression test ([50]).

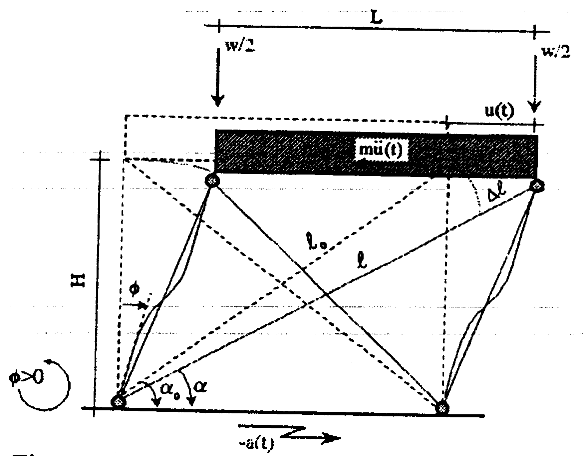

Figure 2.2: The framed structure equipped with SMA tendons considered by Baratta and Corbi ([3], [13]).

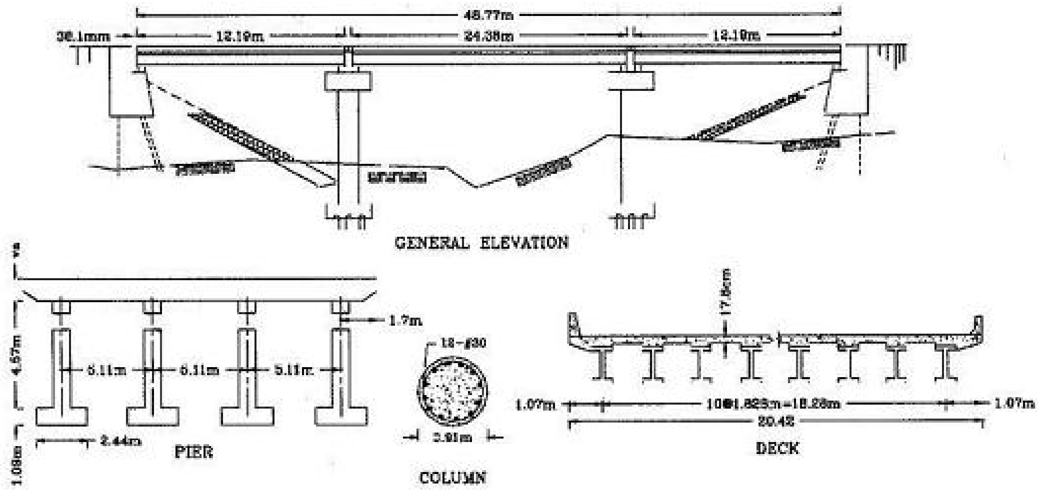

Figure 2.3: Geometry of the simply-supported multi-span bridge studied by DesRoches et al. ([14], [15]).

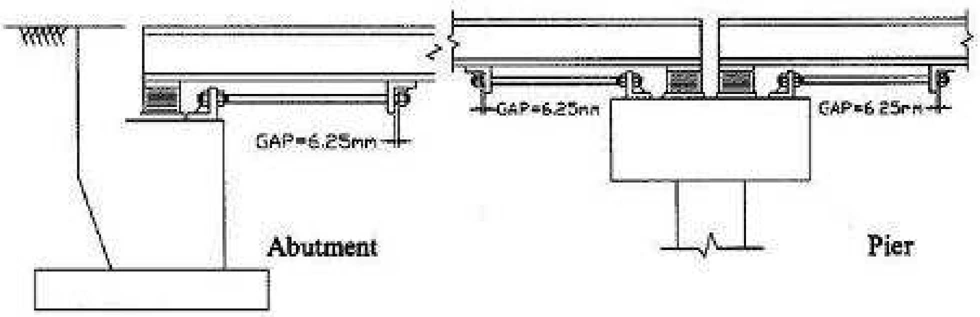

Figure 2.4: Seismic retrofit of the bridge studied by DesRoches et al. ([14], [15]) using superelastic restrainer cables: particular of the connection between deck and abutment and between deck and pier.

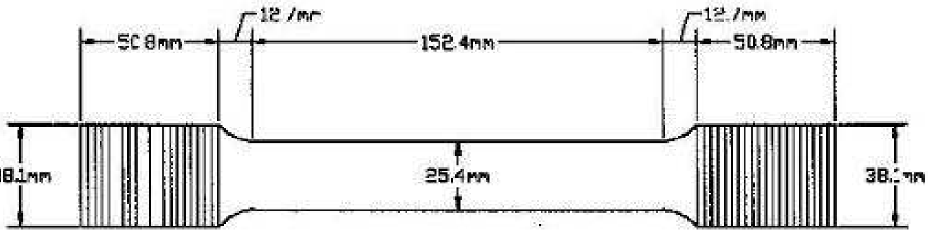

Figure 2.5: Particular of the superelastic restrainer used by DesRoches et al. for the seismic retrofit of bridges ([14], [15]).

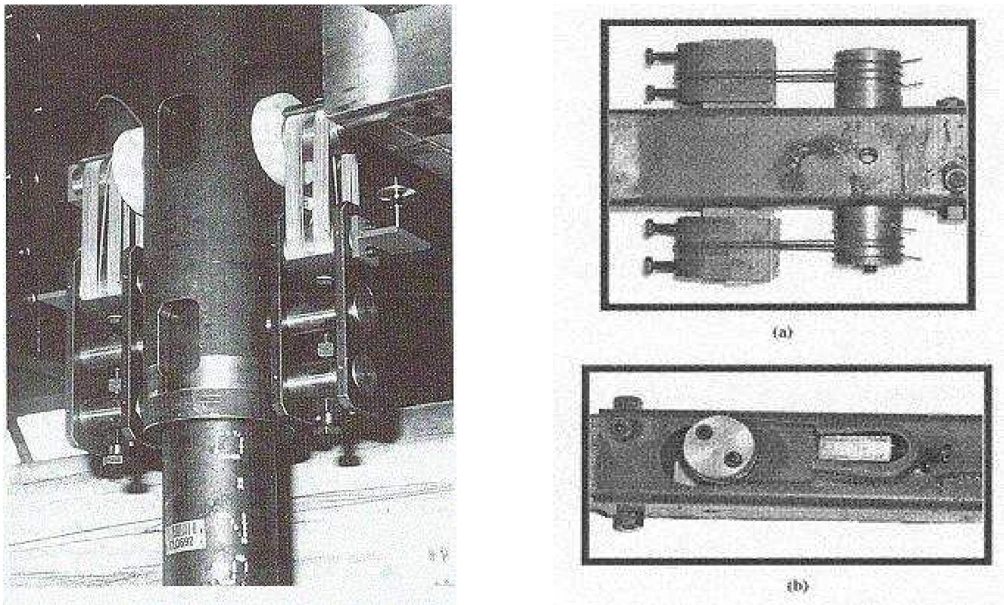

Figure 2.6: Particular of the brace systems studied by Dolce et al. ([18], [19], [20], [21])

.

Figure 2.7: The smart beam-to-column connection studied by DesRoches, Ocel et al. ([15], [48]).

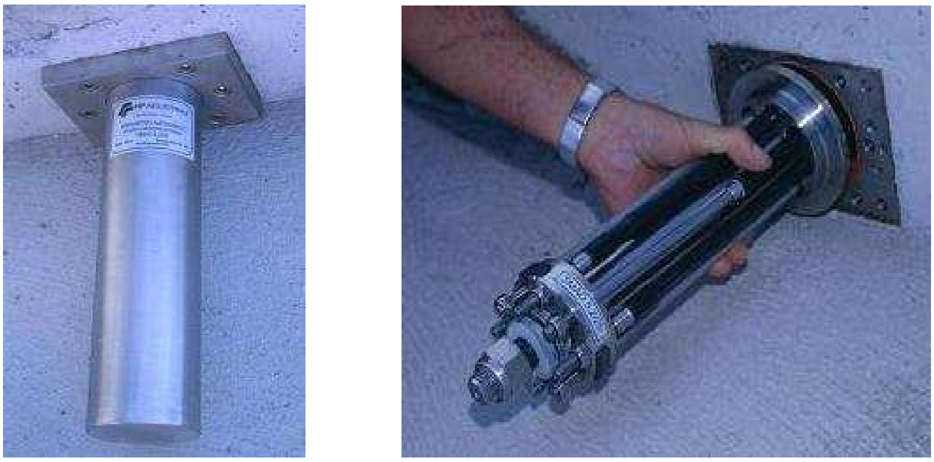

Figure 2.8: Seismic retrofit of the Basilica of San Francesco in Assisi: particular of the SMA devices.

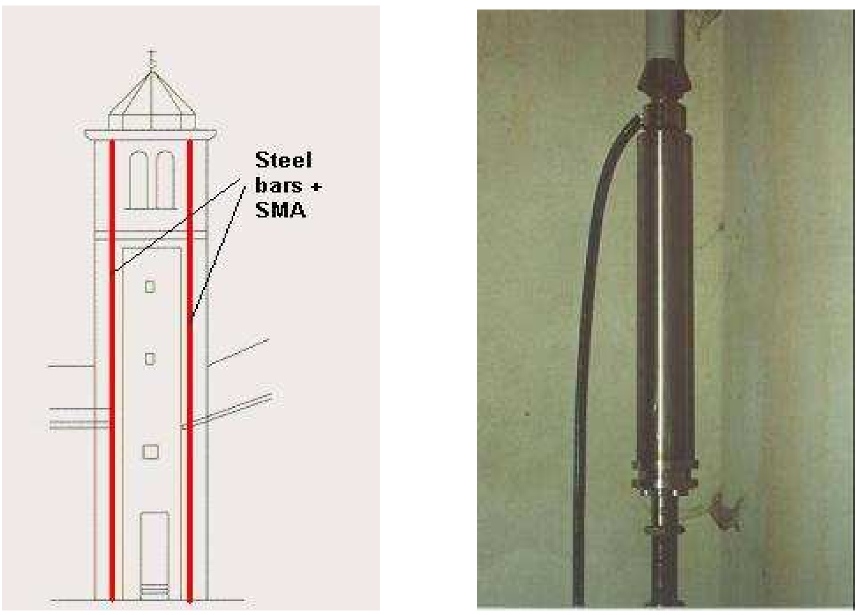

Figure 2.9: Seismic retrofit of the bell tower of the church of San Giorgio in Trignano: (left) elevation of the structure and (right) particular of the SMA rod used.

Chapter 3

Review of Shape-Memory Alloy Constitutive Models

3.1 Introduction

In this chapter we focus the attention on the constitutive modelling of SMAs. Since SMA devices are traditionally used in earthquake engineering as a combination of wires or bars ([18], [19], [20], [21], [60]), emphasis is given only to uniaxial models, which are the ones commonly employed in numerical tests. We analyze six constitutive laws which, according to the recent literature, seem to be the most used and efficient for simulating the seismic response of SMA-based devices. For each of them, we first start with a brief description recalling the expressions needed for the implementation into a finite element code, then we highlight advantages and disadvantages for a better understanding of their correct application.

3.2 Ozdemir model

The model introduced by Ozdemir ([25]) was proposed in 1976 and allows to study the mechanical response of materials showing hysteresis. Even if this formulation does not permit to capture the behavior exhibited by SMAs, it is instead needed to understand the Cozzarelli model, which follows this section. As a consequence, we do not discuss advantages and drawbacks, but we only remind the basic constitutive equations.
The mathematical expressions that describe it are the following:

$$\dot{\sigma} = E\left[\dot{\epsilon} - |\dot{\epsilon}|\left(\frac{\sigma-\beta}{Y}\right)^{n}\right] \tag{3.1}$$

$$\dot{\beta} = \alpha E\,|\dot{\epsilon}|\left(\frac{\sigma-\beta}{Y}\right)^{n} \tag{3.2}$$

with σ the one-dimensional stress, ϵ the one-dimensional strain, β the one-dimensional backstress, E the elastic modulus, Y the yield stress[1], α a constant controlling the slope of the σ-ϵ curve (given by $\alpha = E_y/E - E_y$ being E_y the slope of the σ-ϵ curve after yielding), n a constant controlling the sharpness of transition from elastic to plastic states and $(\cdot)$ the ordinary time derivative.
If we rearrange relationship (3.1), it follows that

$$\dot{\epsilon} = \frac{\dot{\sigma}}{E} + |\dot{\epsilon}| \left(\frac{\sigma - \beta}{Y} \right)^n \tag{3.3}$$

Examination of this equation reveals that the total strain is made up of two separate components: (1) a linear elastic component σ/E and (2) a nonlinear elastic component, ϵ^{in}, described by the rate expression $\dot{\epsilon}^{in} = |\dot{\epsilon}| \left[(\sigma - \beta) / Y \right]^n$. This inelastic component is a function of both the strain rate $\dot{\epsilon}$ and the over-stress σ - β. It would be possible to show that, for the model described by (3.1) and (3.2), the strain is independent of the applied rates of loading (i.e. not dependent on either $\dot{\sigma}$ or $\dot{\epsilon}$). By subtracting expression (3.2) from expression (3.1), we may obtain the following equation:

$$\dot{\sigma} - \dot{\beta} = E\dot{\epsilon} \left[1 - (1+\alpha) \left(\frac{\sigma - \beta}{Y} \right)^n \right] \tag{3.4}$$

which it is useful to rewrite in a more convenient differential form:

$$\mathrm{d}\epsilon = \frac{\mathrm{d}(\sigma - \beta)}{E \left[1 - (1+\alpha) \left(\frac{\sigma-\beta}{Y} \right)^n \right]} \tag{3.5}$$

Then, by integration, we get the solution for the total strain:

$$\epsilon = \frac{Y}{E(1+\alpha)^{1/n}} \int_0^{(\alpha-\beta)/Y} \frac{\mathrm{d}\xi}{1 - \xi^n} \tag{3.6}$$

We can easily observe that, the integral in (3.6) is a function only of the over-stress σ - β and that, equations (3.1) and (3.2), represent a rate-independent stress-strain behavior. Finally, for the spcial case where n = *1*, expression (3.6) specialize to:

$$\sigma = \frac{E\alpha}{1+\alpha}\,\epsilon + \frac{Y}{(1+\alpha)^2} \left\{ 1 - \exp\left[-\frac{E(1+\alpha)}{Y}\,\epsilon \right] \right\} \tag{3.7}$$

which further demonstrates the explicit nature of the rate independence.

[1] In case of SMA modelling, it is the beginning of the stress-induced transition from austenite to martensite.

3.3 Cozzarelli model

With the formulation introduced by Cozzarelli ([24], [25]), the mechanical characterization of SMA materials is accomplished by extending the rate-independent model due to Ozdemir.
In fact, we may account for the SMA twinning hysteretic and/or superelastic behavior by modifying equations (3.1) and (3.2). More precisely, by dividing (3.1) through by $\dot{\epsilon}$, we obtain the slope of the stress-strain constitutive curve:

$$\frac{d\sigma}{d\epsilon} = E\left[1 - \mathrm{sgn}(\dot{\epsilon})\left(\frac{\sigma - \beta}{Y}\right)^n\right] \tag{3.8}$$

where, with the notation sgn(), we indicate the so-called signum function:

$$\mathrm{sgn(x)} = \begin{cases} -1 & \text{if} \quad x < 0 \\ 0 & \text{if} \quad x = 0 \\ +1 & \text{if} \quad x > 0 \end{cases} \tag{3.9}$$

By examining expression (3.8), we can also observe that such a slope is constant during purely linear elastic loading and unloading or, in other words, when (σ - β)/Y $\ll$1. It is possible to modify the shape of the inelastic portion of the σ-ϵ curve by altering the expression for the backstress. In particular, we combine equations (3.1) and (3.2) and then we integrate. Assuming that the initial conditions on σ, β, and ϵ are all zero (i.e. an undeformed virgin material having no residual stress), the previous integration yields:

$$\frac{\beta}{E} = \alpha\left(\epsilon - \frac{\sigma}{E}\right) = \alpha\epsilon^{in} \tag{3.10}$$

From the previous expression we can immediately note that the backstress is a linear function of the inelastic strain ϵ^{in} and, since ϵ^{in} is an evolutionary variable, β is also evolutionary. Also, by modification of equation (3.10), we can describe the various aspects of the SMA behavior. Such a description is provided by adding another term to the inelastic strain in the previous formula:

$$\frac{\beta}{E} = \alpha\left\{\epsilon^{in} + f_T\,|\epsilon^c|\,\mathrm{erf}(\alpha\epsilon)\,[u(-\,\epsilon\dot{\epsilon})]\right\} \tag{3.11}$$

being f_T, α and c material constants controlling the recovery of the elastic strain during unloading. The notations u() and erf() are used to represent the unit step function and the error function which, respectively, are mathematically given by the following relationships:

$$[\mathrm{u(x)}] = \begin{cases} 0 & \text{if} \quad x < 0 \\ +1 & \text{if} \quad x \geq 0 \end{cases} \tag{3.12}$$

$$\mathrm{erf(x)} = \frac{2}{\sqrt{\pi}}\int_0^x e^{-t^2}\,dt \tag{3.13}$$

Equation (3.13) represents a smoothly changing function that passes through zero at the origin and has asymptotic limits of -1 and +1 at $x = +\infty$ and $x = -\infty$, respectively.
We also note how, in equation (3.11), the unit step function activates the added term only during unloading processes and how the ascending branches of the hysteresis loop are unaffected by it. However, when on a descending branch, the added term contributes to the backstress in a way that allows for SMA stress-strain description. The motivation for selecting this particular form of the backstress arises from the requirement of zero residual strain, which is necessary when describing superelastic material behavior.
Moreover, by proper choice of the material constants f_T, a and c, the inelastic strain can be fully recovered, upon complete unloading, to ϵ=0 thus producing the superelastic type of response. Finally, a one-dimensional model that can produce the general macroscopic stress-strain behavior of SMAs is given by equations (3.1) and (3.11) that we rewrite for clarity:

$$\dot{\sigma} = E\left[\dot{\epsilon} - |\dot{\epsilon}|\left(\frac{\sigma-\beta}{Y}\right)^n\right] \tag{3.14}$$

$$\beta = E\alpha\left\{\epsilon^{in} + f_T\,|\epsilon^c|\,erf(\alpha\epsilon)\,[u(-\,\epsilon\dot{\epsilon})]\right\} \tag{3.15}$$

The same model has been later extended to the three-dimensional case ([24]).

Finally, several considerations can be made after analyzing the proposed model. In particular it does have the following advantages:

- Ability to predict both the superelastic and the shape-memory effect.
- Simplicity to be extended to the three-dimensional case.
- Ability to describe sub-loops (i.e. partial transformation paths).

On the other hand, the main drawbacks of the model are:

- Rate and temperature independence;
- Unability to predict the behavior after that the transition from austenite to martensite is completed.
- Mathematical meaning of several model parameters which do not come from experimental data. They are also variable according to the case studied.

3.4 Modified Cozzarelli model

Since SMAs are intended to be used over a wide range of strain, the Cozzarelli model was extended by Wilde et al. ([60]) to represent the hardening of the material after that the transition from austenite to martensite is completed. In particular, as the load increases, the pure martensite follows the elastic response with elastic modulus E_m. Constitutive equations they present assume the following form:

$$\begin{aligned} \dot{\sigma} &= E\left[\dot{\epsilon} - |\dot{\epsilon}|\left(\frac{\sigma-\beta}{Y}\right)^n\right] u_I(\epsilon) + E_m\,\dot{\epsilon}\,u_{II}(\epsilon) \\ &+ \left(3\,a_1\dot{\epsilon}\,\epsilon^2 + 2\,a_2\,sgn(\epsilon)\,\dot{\epsilon}\,\epsilon + a_3\,\dot{\epsilon}\right) u_{III}\,(\epsilon) \end{aligned} \tag{3.16}$$

$$\beta = E\alpha\left\{\epsilon^{in} + f_T\,|\epsilon^c|\,erf(\alpha\epsilon)\,[u(-\,\epsilon\dot{\epsilon})]\right\} \tag{3.17}$$

where the functions $u_I(\epsilon)$, $u_{II}(\epsilon)$ and $u_{III}(\epsilon)$ are:

$$u_I(\epsilon) = (1 - u_{II}(\epsilon) - u_{III}(\epsilon)) \tag{3.18}$$

$$u_{II}(\epsilon) = \begin{cases} 1 & \text{if } |\epsilon| \geq \epsilon_m \\ 0 & \text{otherwise} \end{cases} \tag{3.19}$$

$$u_{III}(\epsilon) = \begin{cases} 1 & \text{if } \epsilon\dot{\epsilon} > 0 \text{ and } \epsilon_1 < |\epsilon| < \epsilon_m \\ 0 & \text{otherwise} \end{cases} \tag{3.20}$$

The term $E_m\dot{\epsilon}u_{II}(\epsilon)$ in formula (3.16) describes the elastic behavior of martensite which is activated when the strain is higher than ϵ_m (see Figure 3.1 for a graphical explanation). Such a value of deformation defines the point where the forward phase transformation from austenite to martensite is completed. The smooth transition from the curve of slope E_y to slope E_m is obtained by adding the last term in (3.16), which is evaluated only during loading and for strains in the range $\epsilon_I < |\epsilon| < \epsilon_m$. Also, the constants a_1, a_2 and a_3 control the curvature of the phase transition.

Finally, several considerations can be made after analyzing the proposed model. In particular it does have the following advantages:

- Ability to represent the SMA behavior after that the transition from austenite to martensite is completed.
- Ability to reproduce both the superelastic and the shape-memory effect.
- Ability to describe sub-loops (i.e. partial deformation paths).

On the other hand, the model accounts for the following drawbacks:

- Mechanical properties are not rate and temperature dependent.
- Mathematical meaning of several model parameters which do not come from experimental data. They are also variable according to the case studied.
- Difficulty to be extended to the three-dimensional case.

3.5 Tanaka model

The consitutive model proposed by Tanaka is considered by Han et al. ([26]) to study the dynamic response of a steel frame equipped with several SMA dampers. Besides the well-known austenite-to-martensite phase transformation (named from now on as M for simplicity), the model takes also into account the so-called R-phase transformation which, traditionally, is considered only by very refined formulations describing the micromechanics of SMAs[2]. On the basis of the analysis of thermo-mechanics and continuum mechanics, Tanaka presents the following consitutive relation:

$$\dot{\sigma} = D\dot{\epsilon} + \Theta\dot{T} + \Omega\dot{\xi} + \Psi\dot{\eta} \tag{3.21}$$

where σ, ϵ and T represent, respectively, stress, strain and temperature. The point above the symbols, again, shows the derivation with respect to time. Symbols D and Θ stand for, respectively, modulus of elasticity and modulus of thermo-elasticity, while relationships Ω/D and Ψ/D indicate, instead, the range of strain resulting from M- and R-phase transformation. Also, ξ and η, with the restrictions $0 \leq \xi \leq 1$, $0 \leq \eta \leq 1$ and $0 \leq \xi + \eta \leq 1$, give the volume percentage of M and R phases respectively. From the two quantities, it is also possible to compute the corresponding volume percentage of austenite phase which results from the expression $1 - (\xi + \eta)$.
We now focus the attention on the evolution of both M- and R-phase transformation, that is giving the mathematical expressions for ξ (M-phase transformation) and η (R-phase transformation).
The volume percentage of M transformation, ξ, can be written as:

$$\xi = 1 - \exp\left[b_M c_M (M_S - T) + b_M \sigma\right] \tag{3.22}$$

$$\xi = \exp\left[b_A c_A (A_S - T) + b_A \sigma\right] \tag{3.23}$$

where b_M, c_M, b_A, c_A are material coefficients. M_S and A_S represent, respectively, the initial and final temperature of the forward and reverse M-phase

[2]Depending on the alloy, upon cooling and before the transformation of martensite, slight crystallographic change might be observed. These martensite-like transformations are called *R-phase transformations* ([1]). Depending on the specific alloy and on its use, different techniques may be used to suppress such transformations.

transformation under conditions of no stress.
The volume percentage of R-phase, η, instead assume the form:

$$\eta = b_M^{'} c_M^{'} (T - M_S{'}) - b_M^{'} \sigma \quad (3.24)$$
$$\eta = 1 + b_A^{'} c_A^{'} (T - M_S{'}) - b_A^{'} \sigma \quad (3.25)$$

where $b_M^{'}$, $c_M^{'}$, $b_A^{'}$, $c_A^{'}$ are again material coefficients. Similarly, $M_S^{'}$ and $A_S^{'}$ represent, respectively, the initial and final temperature of the forward and reverse R-phase transformation under conditions of no stress.

Finally, several considerations can be made after analyzing the proposed model. In particular it does have the following advantages:

- Ability to account for the R-phase as well.
- Temperature dependence.

On the other hand, the model does not take ino account that:

- Material paramters D, Θ and Ω in reality do depend on both martensite fraction and temperature. The model is also rate independent.
- Stiffness before and after the forward trasformation differ.

3.6 Modified Tanaka model

On the basis of the mechanical properties exhibited by NiTi alloys during several experimental investigations, Tamai et al. ([55]) propose a uniaxial constitutive law starting from the basic equations of the Tanaka model.
In particular, they derive the following thermomechanical constitutive relations:

$$\dot{\epsilon} = \dot{\epsilon}_e + \dot{\epsilon}_t \quad (3.26)$$
$$\dot{\sigma} = D\,\dot{\epsilon} + \Omega\,\dot{\xi} \quad (3.27)$$
$$\xi = \xi(\sigma, T) \quad (3.28)$$

where σ is the Cauchy stress, T the material temperature, $\dot{\epsilon}$ the total strain velocity, $\dot{\epsilon}_e$ the elastic strain velocity, $\dot{\epsilon}_t$ the transformation strain velocity, ξ and $\dot{\xi}$ the volume fraction of martensite ($0 < \xi < 1$) and its velocity, D the elastic modulus and Ω a material parameter. Also, from the definition of elastic strain and by means of equations (3.26) and (3.27), the researchers provide the expressions:

$$\dot{\epsilon}_e = D^{-1}\,\dot{\sigma} \quad (3.29)$$
$$\dot{\epsilon}_t = -D^{-1}\,\Omega\,\dot{\xi} \quad (3.30)$$

They also assume an exponential form for the kinetics of the stress induced transformations under uniaxial stress. In particular, for forward and reverse transformation respectively, the following relationships hold:

$$\xi = \xi(\sigma, T) = 1 - \exp\ [a_M(M_S - T) + b_M\sigma] \tag{3.31}$$
$$\xi = \xi(\sigma, T) = \exp\ [a_A(A_S - T) + b_A\sigma] \tag{3.32}$$

where M_S and A_S are, respectively, the martensite and austenite start temperatures under zero external stress, while a_M, b_M, a_A and b_A are material parameters derived from experimental data. Furthermore, the research group elaborates the expressions related to the transformation conditions. More precisely, for forward transformation:

$$-a_M\dot{T} + b_M\dot{\sigma} \leq 0 \quad \text{for} \quad a_M(M_S - T) + b_M\sigma \leq 0 \tag{3.33}$$

while for reverse transformation:

$$-a_A\dot{T} + b_A\dot{\sigma} \leq 0 \quad \text{for} \quad a_A(A_S - T) + b_A\sigma \leq 0 \tag{3.34}$$

Parameters a_M, b_M, a_A and b_A (also called coefficients of transformational kinetics) are given by the following expressions:

$$\begin{aligned} a_M &= -2\ \log(10)/(M_S - M_f) \quad b_M = -2\ \log(10)/\Delta\sigma_M \\ a_A &= 2\ \log(10)/(A_f - A_s) \qquad b_A = 2\ \log(10)/\Delta\sigma_A \end{aligned} \tag{3.35}$$

being M_f and A_f the martensite and austenite finish temperature under zero externall stress and the stress differences $\Delta\sigma_M$ and $\Delta\sigma_A$ the isothermal stress width from start to finish of transformation. As a final result, integration of equation (3.26) from origin ($\xi = 0$) to a certain time ($\xi = 1$) gives,

$$\Omega = \sigma_{max} - D\ \epsilon_{max} \tag{3.36}$$

where ϵ_{max} and σ_{max} are the increment of strain and stress from $\xi = 0$ to $\xi = 1$ under monotonic loading.

Finally, several considerations can be made after analyzing the proposed model. In particular it does have the following advantages:

- Temperature dependence.
- Simplicity in the computer implementation because of the simple stress-strain relationship and evolutionary equations.

On the other hand the model does not take ino account that:

- Stiffness after completition of the forward phase transformation is different from the initial stiffness.

- Material properties D and Ω should be dependent on both martensite volume fraction and temperature. The model is also rate independent.

- The experienced maximum strain should be an internal variable in the kinetic of the reverse trasformation.

3.7 A temperature-dependent model

In this paragraph we present a constitutive relation ([5], [31], [49]) able to capture the rate-dependance of the response under arbitrary loads.
The model has extensively been used for the numerical investigations performed during the Project Manside, in order to predict the seismic response of framed structure equipped with SMA-based devices ([8], [59]).
SMAs are thougth as a mixture of two solid phases whose individual behavior is modelled as a linear isotropic thermoelastic material. The composition of such mixture is described by the scalar internal variable z which represents the mass fraction of marteniste phase with respect to the total mass.
The kinematic effect of the phase transformation is characterized by the local transformation strain arising from the different crystallographic structure between austenite and martensite. Such a local strain gives rise to a macroscopic deformation that, in this model, is assumed to be proportional to the martensite fraction by means of the factor Λ.
The thermodynamic properties of the mixture are described in terms of the Helmhotz free energy that, for this particular constitutive law, is assumed in the following polynomial form:

$$\psi = \psi_1 + (\psi_2 - \psi_1)\, z + A\, z\, (1 - z) \tag{3.37}$$

where ψ_α is the free energy of the pure phase α, with α=1 for austenite and with α=2 for martensite. The last additive term is representative of the elastic energy stored in the accomodation of the local strain associated with the phase transformation, being A a material constant. The explicit formula assumed for the considered free energy is:

$$\begin{aligned}\psi &= \frac{E(z)}{2\rho}\,\epsilon^2 - c(z)\,\theta\,\ln\frac{\theta}{\theta_0} + \left(\frac{E(z)\Lambda^2}{2\rho} - A\right)\, z^2 - \frac{3\alpha(z)}{\rho}\,\epsilon(\theta-\theta_0) \\ &- \frac{E(z)\Lambda}{\rho}\,\epsilon z + \frac{3\alpha(z)\Lambda}{\rho}\, z\,(\theta-\theta_0) + \eta_0(z)(\theta-\theta_0)A\, z + \psi_0 \end{aligned} \tag{3.38}$$

and it is written with respect to a reference state defined by ϵ_0=0, σ=0, $\theta = \theta_0$ and *z=0* (i.e. austenitic phase). $\eta_0(z)$ and ψ_0 are respectively the overall entropy and free energy at reference state. In the above expression *E(z)*, *c(z)* and $\alpha(z)$ are, respectively, the modulus of elasticity, the specific heat at constant strain and the thermal expansion modulus. The thermal and mechanical properties are all dependent on the internal variable to take into account their

variation during the phase transformation.
Along the lines of standard continuum thermodynamics, the consitutive equations for stress can be derived from (3.38). Moreover the phase transformation process turns out to be driven by the generalized thermodynamic force X. In particular we have:

$$\sigma = \rho \frac{\partial \psi}{\partial \epsilon} \qquad X = -\frac{\partial \psi}{\partial z} \tag{3.39}$$

In addition, the combination of the energy conservation and the entropy balance allows to derive the heat equation:

$$\rho \, c \, \dot{\theta} + (\rho \, \Delta\eta_0 + X)\dot{z} = \dot{Q} \tag{3.40}$$

where $\Delta\eta_0$ is the entropy difference between the phases at the reference state and Q is the rate of heat exchange with the surrounding environment.
Finally, the evolution of the phase transformation as a function of the applied loads is governed by the following ordinary differential equation:

$$\dot{z} = M_{11}(\epsilon, \theta, z) \, \dot{\theta} + M_{12}(\epsilon, \theta, z) \, \dot{\sigma} \tag{3.41}$$

where the terms M_{11} and M_{12} assume different expressions when the phase transformation takes place in forward (martensite formation) or reverse (austenite formation) direction.
Such terms characterize the dissipative properties of the material and, in particular, determine the capability of the model to account for arbitrary thermomechanical loads. Finally, we mention the evolutionary equations needed to describe both the forward and the reverse transformation. In particular in forward transformation we have:

$$\dot{z} = \frac{1 - z}{1 - G_{Fw}} \, \frac{dG_{Fw}}{d\beta} \, \dot{\beta} \tag{3.42}$$

while for reverse transformation the following expression yields:

$$\dot{z} = \frac{z}{G_{Rv}} \, \frac{dG_{Rv}}{d\beta} \, \dot{\beta} \tag{3.43}$$

In both cases, β is a proper function of the stress and temperature that can be seen as the part of the driving force X not dependent on z.
The functions G_{Fw} and G_{Rv} define the external hysteresis loop associated with complete forward and reverse phase transformation and depend only on β. By a proper assignment of the shape of such functions, we may embody in the activation conditions of the phase transformation in a smoothed way.

Finally, several considerations can be made after analyzing the proposed model. In particular it does have the following advantages:

- Dependence of thermal and mechanical properties on the volume martensite fraction to take into account their variation during the phase transformations.

- Ability to capture rate and temperature dependance under arbitrary loads.

- Ability to describe the SMA behavior for both partial and complete trasformation.

On the other hand the model possesses the following drawbacks:

- Difficulty in the computer coding for the not straightforward derivation of the analytical expressions for stress and evolutionary equations.

- Material parameters difficult to determine by means of classical experimental devices.

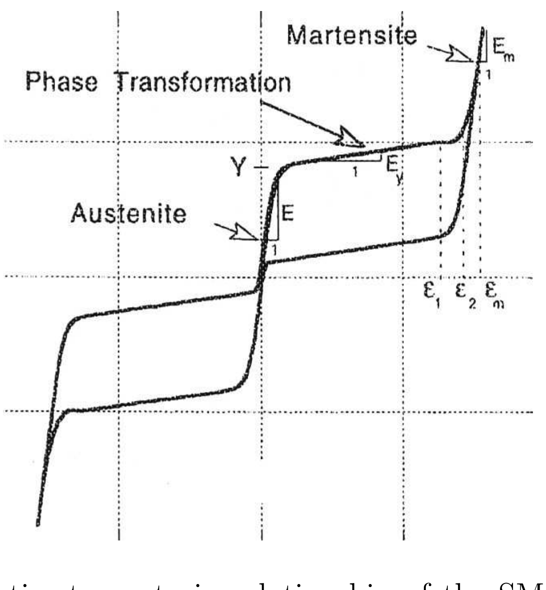

Figure 3.1: Schematic stress-strain relationship of the SMA model proposed by Wilde et al. ([60])

Chapter 4

Adopted Constitutive Model for Shape-Memory Alloys

4.1 Introduction

In this section we propose a uniaxial constitutive model for pseudoelastic SMAs. The basis of the formulation, developed under the hypothesis of small deformation regime, is the assumption that the relationship between strains and stresses is represented by a series of linear curves, whose form is determined by the extent of the transformation experienced.
Initially, we start describing the time-continuous model, then we focus on its integration tecnique, providing the evolutionary equations together with the expression of the consistent tangent modulus. Finally, after the numerical assessment, we check the ability of the model to simulate experimental data.

4.2 Time-continuous model

We assume to work with one scalar internal variable, ξ_S, representing the martensite fraction, and with two processes which may produce its variations:

- the conversion of austenite into martensite (A $\rightarrow$ S);
- the conversion of martensite into austenite (S $\rightarrow$ A).

Following experimental evidence ([2]), for both the processes we choose linear *kinetic rules* in terms of the uniaxial stress σ. In particular, the activation conditions for the conversion of austenite into martensite are:

$$\sigma_s^{AS} < |\sigma| < \sigma_f^{AS} \qquad \text{and} \qquad \dot{\overline{|\sigma|}} > 0 \tag{4.1}$$

where σ_s^{AS} and σ_f^{AS} are material parameters, $|\cdot|$ is the absolute value and a superpose dot indicates a time derivative[1]. The corrisponding evolution

[1]A superposed dot over a bar indicates that the whole quantity under the bar is derived.

equation is set equal to:

$$\dot{\xi}_S = -(1 - \xi_S)\frac{\dot{\overline{|\sigma|}}}{|\sigma| - \sigma_f^{AS}} \tag{4.2}$$

On the other hand, the activation conditions for the conversion of martensite into austenite are:

$$\sigma_f^{SA} < |\sigma| < \sigma_s^{SA} \qquad \text{and} \qquad \dot{\overline{|\sigma|}} < 0 \tag{4.3}$$

with σ_f^{SA} and σ_s^{SA} material parameters. The corresponding evolution equation is set equal to:

$$\dot{\xi}_S = \xi_S \frac{\dot{\overline{|\sigma|}}}{|\sigma| - \sigma_f^{SA}} \tag{4.4}$$

4.3 Strain decomposition and elastic relation

Limiting the discussion to a small deformation regime, we assume an additive decomposition of the total strain ϵ:

$$\epsilon = \epsilon^e + \epsilon_L \xi_S \mathrm{sgn}(\sigma) \tag{4.5}$$

where ϵ^e is the elastic strain, ϵ_L is the maximum residual strain and $\mathrm{sgn}(\cdot)$ is the sign function. The maximum residual strain ϵ_L, regarded as a material constant, is a measure of the maximum deformation obtainable only by a multiple-variant martensite detwinning, hence, a measure of the maximum deformation obtainable aligning all the multiple-variant martensites in one direction. Moreover, the presence of $\mathrm{sgn}(\sigma)$ in equation (4.5), indicates that the direction of the effect relative to the martensite fraction ξ_S is governed by the stress. The elastic stress is assumed to be linearly related to the stress:

$$\sigma = E\epsilon^e \tag{4.6}$$

with E the elastic modulus.

4.4 Time-discrete model

While during the development of the time-continuous model we assumed the stress as control variable, during the development of the time-discrete model we assume the strain as control variable. The choice is consistent with the fact that, from the point of view of the integration scheme, the time-discrete problem is considered strain-driven. Accordingly, we consider two time values, say t_n and t_{n+1}, such that t_{n+1} is the first time value of interest after t_n. Then, knowing the strain at time t_{n+1} and the solution at time t_n, we should compute the new solution at time t_{n+1}. To minimize the appearence of subscrits (and to make the equations more readable), we introduce the convention:

$$a_n = a(t_n), \qquad a = a(t_{n+1}) \tag{4.7}$$

where a is a generic quantity. Therefore, the subscript n indicates a quantity evaluated at time t_n, while no subscript indicates a quantity evaluated at time t_{n+1}.
We use a backward-Euler scheme to integrate the time-continuous evolutionary equations (4.2) and (4.4). Written in residual form and after clearing the fractions, the time-discrte evolutionary equations specialize to:

$$\mathcal{R}^{AS} = \lambda_S(|\sigma| - \sigma_f^{AS}) + (1 - \xi_S)(|\sigma| - |\sigma_n|) = 0 \tag{4.8}$$

$$\mathcal{R}^{SA} = \lambda_S(|\sigma| - \sigma_f^{SA}) + \xi_S(|\sigma| - |\sigma_n|) = 0 \tag{4.9}$$

where the martensite fraction increment λ_S is defined as:

$$\xi_S = \xi_{S,n} + \lambda_S \qquad \text{or} \qquad \lambda_S = \int_{t_n}^{t_{n+1}} \dot{\xi}_S dt \tag{4.10}$$

The quantity λ_S can be computed expressing the stress σ as a function of λ_S and requiring the satisfaction of the evolutionary equation corresponding to the active phase transformation.
Introduction of equation (4.6) into equation (4.5) indicates that:

$$\mathrm{sgn}(\sigma) = \mathrm{sgn}(\epsilon) \tag{4.11}$$

hence, equation (4.5) can be rewritten as:

$$\epsilon = \epsilon^e + \epsilon_L \xi_S \mathrm{sgn}(\epsilon) \tag{4.12}$$

Making use of equation (4.12), substitution of expression (4.6) into equations (4.8) and (4.9) transforms the time-discrete evolutionary equations in two equations which can be solved in terms of λ_S.

4.5 Algorithmic tangent modulus

In the following, we discuss the construction of the tangent modulus consistent with the time-discrete model. The use of a consistent tangent modulus preserves the quadratic convergence of the Newton method.
From the linearization of the equation (4.5) we get:

$$\mathrm{d}\sigma = E[\mathrm{d}\epsilon - \epsilon_L \mathrm{sgn}(\epsilon)\mathrm{d}\lambda_S] \tag{4.13}$$

Assuming that:

$$\mathrm{d}\lambda_S = H\mathrm{d}\epsilon \tag{4.14}$$

we can solve equation (4.13) in terms of $\mathrm{d}\sigma$, obtaining the relation:

$$\mathrm{d}\sigma = E^T \mathrm{d}\epsilon \tag{4.15}$$

where the tangent elastic modulus E^T is given by:

$$E^T = E[1 - \epsilon_L H \mathrm{sgn}(\epsilon)] \tag{4.16}$$

The quantity H is computed from the linearization of the discrete evolutionary equations corresponding to the active phase transformation. Then, from equations (4.8) and (4.9) we get:

$$\mathrm{d}\mathcal{R}^{AS} = (1 - \xi_{S,n})\mathrm{d}|\sigma| + \mathrm{d}\lambda_S[|\sigma_n| - \sigma_f^{AS}] = 0 \tag{4.17}$$

$$\mathrm{d}\mathcal{R}^{SA} = -\xi_{S,n}\mathrm{d}|\sigma| + \mathrm{d}\lambda_S[|\sigma_n| - \sigma_f^{SA}] = 0 \tag{4.18}$$

Since $\mathrm{d}|\sigma| = \mathrm{sgn}(\sigma)\mathrm{d}\sigma = \mathrm{sgn}(\epsilon)\mathrm{d}\sigma$, relation (4.13) allows to solve equations (4.17) and (4.18) in terms of $\mathrm{d}\lambda_s$ obtaining respectivly:

$$H = H^{AS} = \frac{-\mathrm{sgn}(\epsilon)\,(1 - \xi_{S,n})\,E}{(1 - \xi_{S,n})\,[-\mathrm{sgn}(\epsilon)\,E\,\epsilon_L] + \sigma_n - \mathrm{sgn}(\epsilon)\,\sigma_f^{AS}} \tag{4.19}$$

$$H = H^{SA} = \frac{\mathrm{sgn}(\epsilon)\,\xi_{S,n}\,E}{\xi_{S,n}\,[\mathrm{sgn}(\epsilon) E\,\epsilon_L] + \sigma_n - \mathrm{sgn}(\epsilon)\,\sigma_f^{SA}} \tag{4.20}$$

Also, substituting equation (4.13) into equations (4.8) and (4.9), it is possible to get the value of martensite fraction during the deformation history.
In particular, for the conversion of austenite into martensite we have:

$$\xi = \xi^{AS} = \frac{\xi_{S,n}\,E\,\epsilon - \mathrm{sgn}(\epsilon)\,\xi_{S,n}\,\sigma_f^{AS} - E\,\epsilon + \sigma_n}{-\mathrm{sgn}(\epsilon)\,\sigma_f^{AS} + \mathrm{sgn}(\epsilon)\,\xi_{S,n}\,E\,\epsilon_L - \mathrm{sgn}(\epsilon)\,E\,\epsilon_L + \sigma_n} \tag{4.21}$$

while for the conversion of martensite into austenite we have:

$$\xi = \xi^{SA} = \frac{\xi_{S,n}\,E\,\epsilon - \mathrm{sgn}(\epsilon)\,\xi_{S,n}\,\sigma_f^{SA}}{-\mathrm{sgn}(\epsilon)\,\sigma_f^{SA} + \mathrm{sgn}(\epsilon)\,\xi_{S,n}\,E\,\epsilon_L + \sigma_n} \tag{4.22}$$

4.6 Numerical assessment

We dedicate this section to the assessment of the presented model through several numerical tests. Obviously, we include only the most significant ones and, together with the investigation, we discuss advantages and disatvantages of the consitutive formulation.
For the numerical analyses we choose the following material properties:

$$\begin{aligned} E &= 40000\,\mathrm{MPa} \qquad & \epsilon_L &= 6\% \\ \sigma_s^{AS} &= 500\,\mathrm{MPa} \qquad & \sigma_f^{AS} &= 600\,\mathrm{MPa} \\ \sigma_s^{SA} &= 300\,\mathrm{MPa} \qquad & \sigma_f^{SA} &= 200\,\mathrm{MPa} \end{aligned}$$

In Figures 4.1 to 4.4 we see the plots of such analyses. It is then possible to observe the ability of the model to describe complex uniaxial loading histories (Figures 4.1 and 4.2) as well as to reproduce complete transformation paths under tensile and compressive deformations (Figures 4.3 and 4.4).

Finally, we highlight the main advantages of the adopted SMA model:

- Robustness and simplicity of implementation. The first characteristics is particularly important in view of future dynamic applications, because allows to reduce the integration step with a consequent decrease of computational effort.
- Simplicity in obtaining the material parameters. They simply come from classical uniaxial tests conducted on either wires or bars.
- Simplicity to be extended in such a way to define a different behavior between tension and compression, as in reality.
- Simplicity to be extended in such a way to account for the different elastic properties between austenite and martensite.
- Ability to reproduce partial (i.e. sub-loops) and complete transformation paths (i.e. from fully austenite to fully martensite).

Neverthless, the model is affected by the following drawbacks:

- Rate and temperature independence. In reality, SMA materials' behavior is strongly affected by both frequency of loading and thermal variations (see Chapter 2 for further explanations).
- Inability to reproduce the shape-memory effect. This is evident from the fact that the SMA model has been chosen in such a way to reproduce the superelastic effect only.
- Inability to account for the different elastic properties between austenite and martensite.

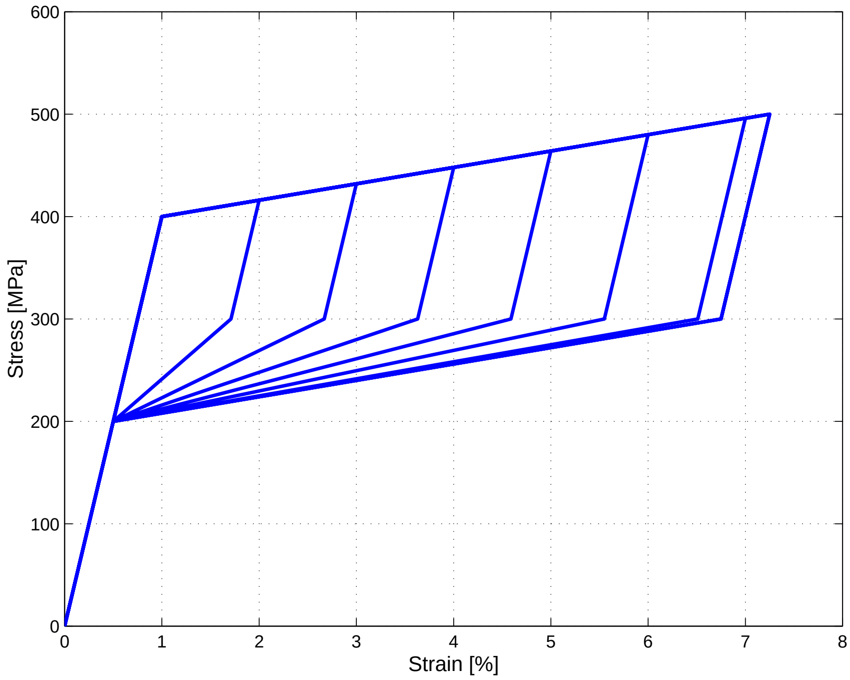

Figure 4.1: Uniaxial test: numerical simulation of multiple stress cycles. A complete transformation path is followed by partial loading and complete unloading.

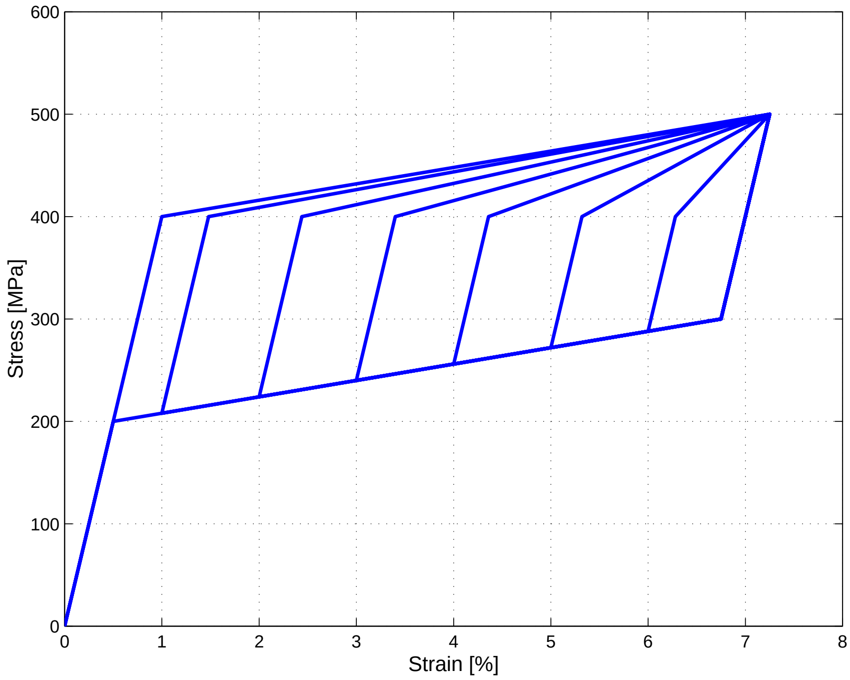

Figure 4.2: Uniaxial test: numerical simulation of multiple stress cycles. A complete transformation path is followed by complete loading and partial unloading.

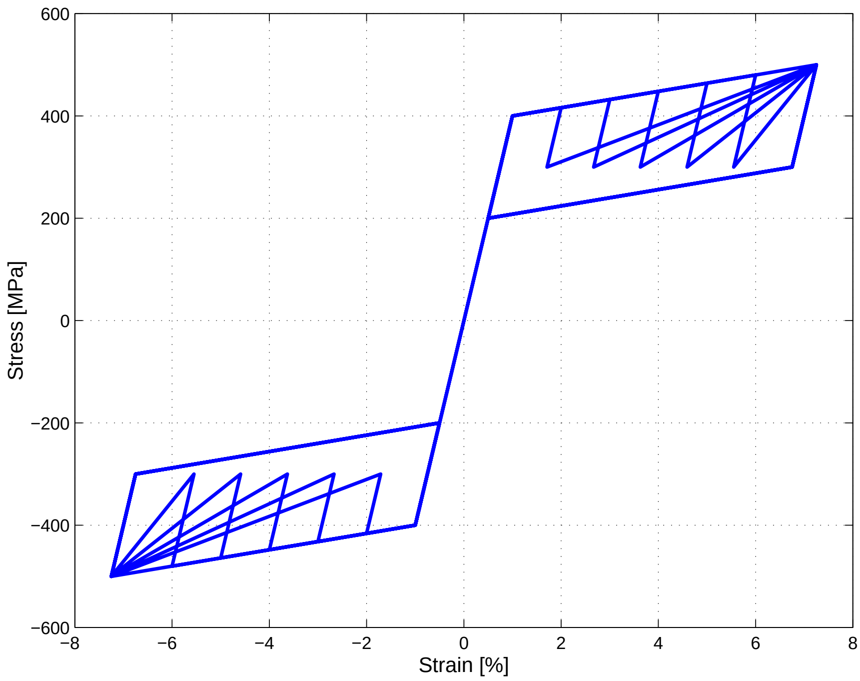

Figure 4.3: Uniaxial test: numerical simulation of multiple tension-compression stress cycles. A complete transformation path is preceeded by partial unloading and complete loading.

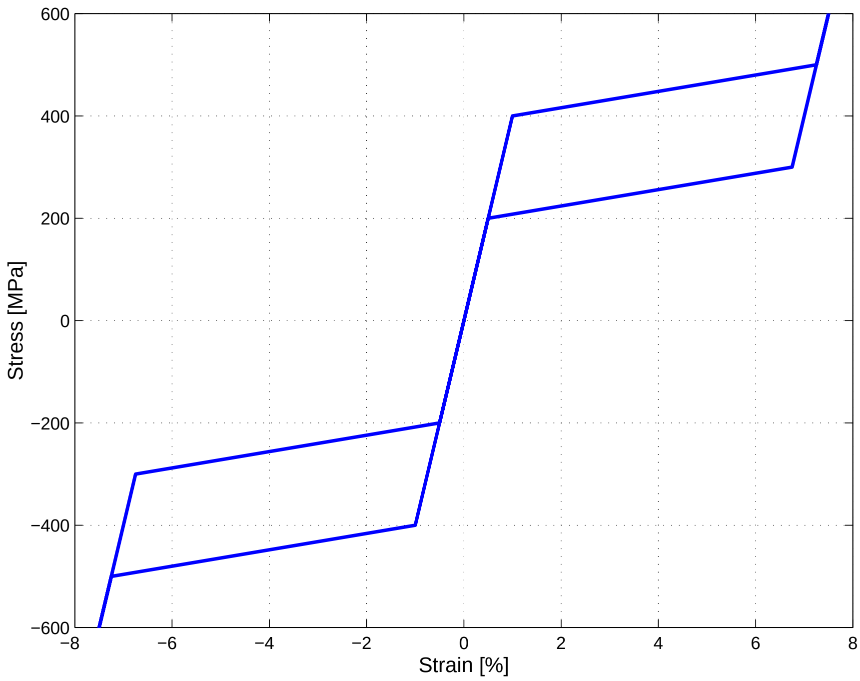

Figure 4.4: Uniaxial test: numerical simulation of the complete tension-compression transformation cycle.

4.7 Comparison with experimental data

We now want to assess the ability of the model to predict the typical SMA superelastic stress-strain response of wire elements. We focus on experimental data relative to nickel-titanium alloys which, nowadays, are the shape-memory material most frequently used in commercial applications.

NDC NiTi alloy

We consider the experimental data presented in reference [2] and here reported with continuous lines in Figures 4.5 and 4.6. The material, provided by Nitinol Devices & Components ([46]), is a commercial superelastic NiTi straight wire with circular cross section of diameter 1.49 mm.
From the inspection of the experimental stress-strain curves the following material parameters are chosen for the model:

$$\begin{aligned} E &= 60000\,\mathrm{MPa} & \epsilon_L &= 8\% \\ \sigma_s^{AS} &= 520\,\mathrm{MPa} & \sigma_f^{AS} &= 600\,\mathrm{MPa} \\ \sigma_s^{SA} &= 240\,\mathrm{MPa} & \sigma_f^{SA} &= 200\,\mathrm{MPa} \end{aligned}$$

GAC NiTi alloy

We consider the experimental data presented in reference [2] and here reported with continuous lines in Figure 4.7. The material, provided by GAC International Inc., is a commercial superelastic NiTi straight wire with rectangular cross section of dimensions 0.64 mm x 0.46 mm.
From the inspection of the experimental stress-strain curves the following material parameters are chosen for the model:

$$\begin{aligned} E &= 47000\,\mathrm{MPa} & \epsilon_L &= 8\% \\ \sigma_s^{AS} &= 350\,\mathrm{MPa} & \sigma_f^{AS} &= 350\,\mathrm{MPa} \\ \sigma_s^{SA} &= 125\,\mathrm{MPa} & \sigma_f^{SA} &= 125\,\mathrm{MPa} \end{aligned}$$

FIP NiTi alloy

We consider the experimental data provided by FIP Inc. and here reported with continuous lines in Figure 4.8. The material is a commercial superelastic NiTi straight wire with circular cross section of diameter 2.01 mm.
From the inspection of the experimental stress-strain curves the following material parameters are chosen for the model:

$$\begin{aligned} E &= 80000\,\mathrm{MPa} & \epsilon_L &= 8\% \\ \sigma_s^{AS} &= 590\,\mathrm{MPa} & \sigma_f^{AS} &= 670\,\mathrm{MPa} \\ \sigma_s^{SA} &= 250\,\mathrm{MPa} & \sigma_f^{SA} &= 200\,\mathrm{MPa} \end{aligned}$$

Figures 4.5 to 4.8 show the comparison between experimental data (obtained from tests performed in static conditions) related to SMA wires and numerical predictions. In the following a discussion of the results:

- Figures 4.5, 4.6 and 4.8 show the good capacity of the model to fit experimental data. In particular, during the loading phase (i.e. $A \rightarrow S$ phase transformation) numerical results are in very good agreement with the experimental ones. During the unloading phase (i.e. $S \rightarrow A$ phase transformation), instead, the model overestimates the material's stiffness and consequently the hysteresis loop generated is fatter. This, in effect, is what we expected because the implemented SMA model does not take into account the different elastic properties between austenite and martensite. As a consequence, the loading and unloading branches have the same stiffness. As already discussed previously, in reality SMA materials do present a different elastic modulus between the two phases ([2]). Tipically the Young's modulus of the martensitic phase is lower than that of the austenitic phase and, during the phase transformation, it is a combination of the two values.

- Figure 4.7 highilights the excellent capability of the model to simulate the stress-strain behavior of SMA specimens characterized by horizontal plateaus. Only a small negligible discrepancy between experimental data and numerical values is observed during the unloading phase (i.e. $S \rightarrow A$ phase transformation) and, again, it is due to an overestimation of the elastic properties of the martensitic phase.

4.8 Final remarks

Despite the ability of the model to describe the material response also for complex uniaxial loading histories (full forward and reverse phase transformations, partial loading-unloading patterns with the description of internal hysteresis loops), it seems evident that a more complete set of experimental data should be required to get a reliable evaluation of the material parameters. In particular, under dynamic loads, the material parameters are different with respect to the same values related to static load conditions. Obvioulsy, to overcome these problems, a more complex rate-dependent consitutive law would be required and it will be the topic of future works. Anyway, the advantages of the presented model are the simplicity, the possibility of implementing a robust solution algorithm and the ability to successfully reproduce the complex superelastic behavior for different SMA materials.

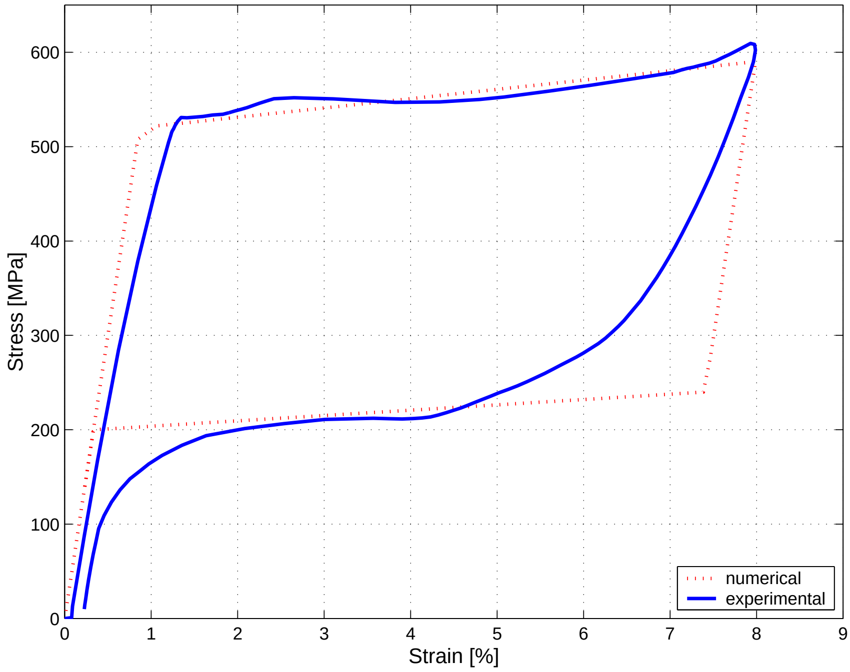

Figure 4.5: NDC NiTi alloy. Uniaxial tension stress-strain response. Experimental data and numerical simulation.

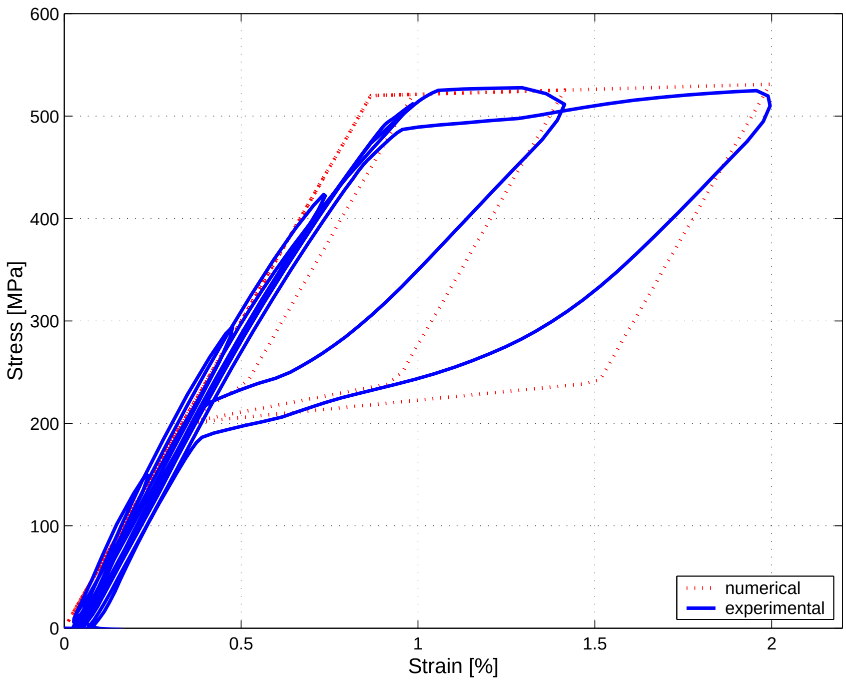

Figure 4.6: NDC NiTi alloy. Uniaxial tension stress-strain response. Experimental data and numerical simulation.

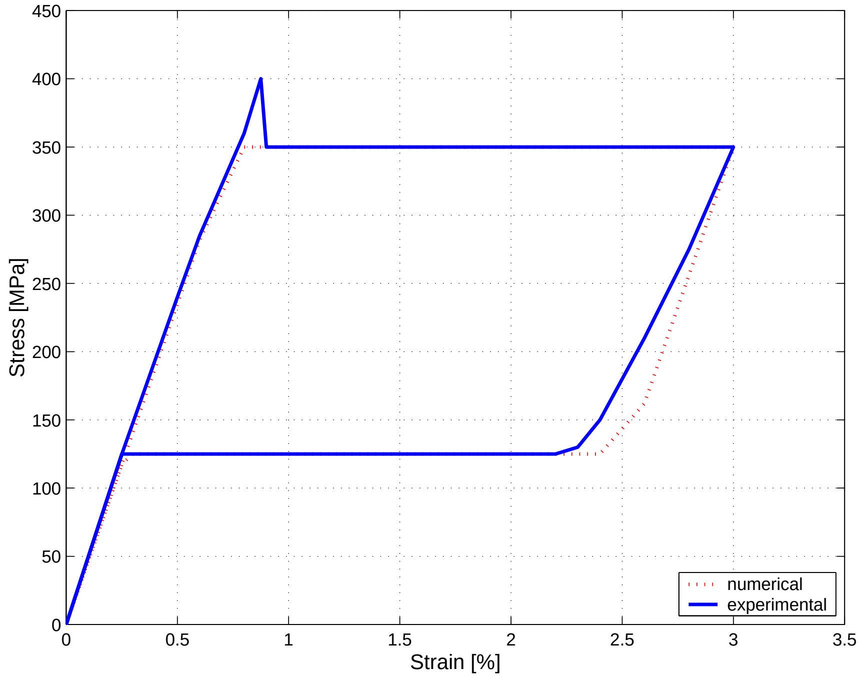

Figure 4.7: GAC NiTi alloy. Uniaxial tension stress-strain response. Experimental data and numerical simulation.

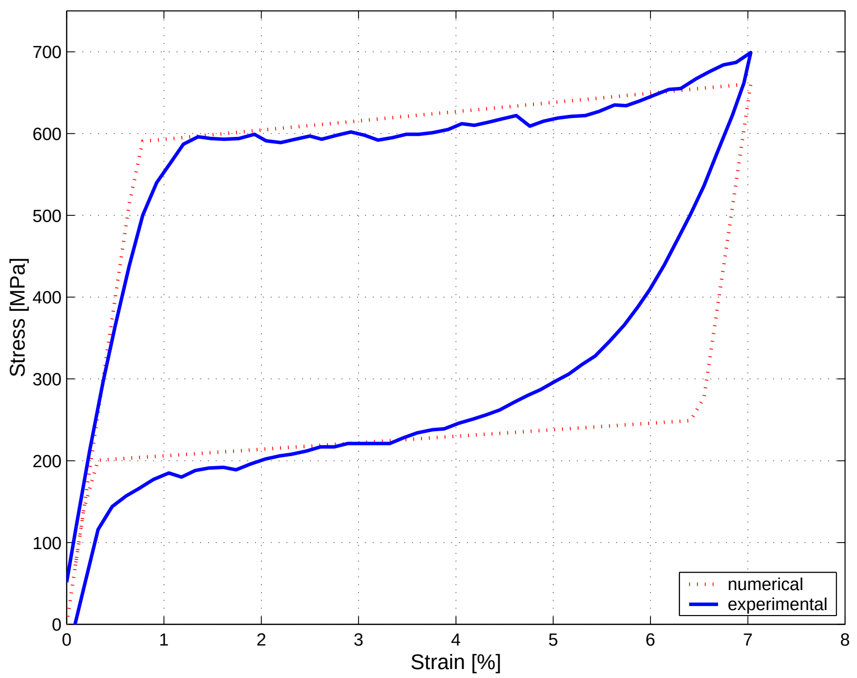

Figure 4.8: FIP NiTi alloy. Uniaxial tension stress-strain response. Experimental data and numerical simulation.

Parameters	**NDC**	**GAC**	**FIP**
E [MPa]	60000	47000	80000
ϵ_L [%]	8	8	7
σ_s^{AS} [MPa]	520	350	590
σ_f^{AS} [MPa]	600	350	670
σ_s^{SA} [MPa]	240	125	250
σ_f^{SA} [MPa]	200	125	200

Table 4.1: Summary of the mechanical properties of the considered SMA wires.

1. Detect loading or unloading

If $|\,\epsilon - \epsilon_n| > 0 \Rightarrow$ loading
If $|\,\epsilon - \epsilon_n| < 0 \Rightarrow$ unloading

2. Check phase transformation

If loading then
  check A $\rightarrow$ S phase transformation (Table 4.3)
else if unloading then
  check S $\rightarrow$ A phase transformation (Table 4.4)
end if

3. Algorithmic tangent

Compute tangent

Table 4.2: Overall strain-driven solution algorithm.

If $|\,\epsilon - \epsilon_n| > 0$ then $\Rightarrow$ loading

$$\begin{aligned} \epsilon_s^{AS} &= sgn(\epsilon)\,\frac{\sigma_s^{AS}}{E} + sgn(\epsilon)\,\xi_{S,n}\,\epsilon_L \\ \epsilon_f^{AS} &= sgn(\epsilon)\,\frac{\sigma_s^{AS}}{E} + sgn(\epsilon)\,\epsilon_L \end{aligned}$$

if $-|\,\epsilon_s^{AS}| < |\,\epsilon| < |\,\epsilon_s^{AS}|$

$$\begin{aligned} \xi &= \xi_{S,n} \\ H &= 0 \end{aligned}$$

else if $|\,\epsilon_s^{AS}| < |\,\epsilon| < |\,\epsilon_f^{AS}|$

if $|\,\sigma_n| < \sigma_s^{AS}$

$$\begin{aligned} \xi &= \frac{\xi_{S,n}\,E\,\epsilon - sgn(\epsilon)\,\xi_{S,n}\,\sigma_f^{AS} - E\,\epsilon + sgn(\epsilon)\,\sigma_s^{AS}}{-sgn(\epsilon)\,\sigma_f^{AS} + sgn(\epsilon)\,\xi_{S,n}\,E\,\epsilon_L - sgn(\epsilon)\,E\,\epsilon_L + sgn(\epsilon)\,\sigma_s^{AS}} \\ H &= \frac{-sgn(\epsilon)\,(1-\xi_{S,n})\,E}{(1-\xi_{S,n})\,[-sgn(\epsilon)E\,\epsilon_L] + sgn(\epsilon)\,\sigma_s^{AS} - sgn(\epsilon)\,\sigma_f^{AS}} \end{aligned}$$

else

$$\begin{aligned} \xi &= \frac{\xi_{S,n}\,E\,\epsilon - sgn(\epsilon)\,\xi_{S,n}\,\sigma_f^{AS} - E\,\epsilon + \sigma_n}{-sgn(\epsilon)\,\sigma_f^{AS} + sgn(\epsilon)\,\xi_{S,n}\,E\,\epsilon_L - sgn(\epsilon)\,E\,\epsilon_L + \sigma_n} \\ H &= \frac{-sgn(\epsilon)\,(1-\xi_{S,n})\,E}{(1-\xi_{S,n})\,[-sgn(\epsilon)\,E\,\epsilon_L] + \sigma_n - sgn(\epsilon)\,\sigma_f^{AS}} \end{aligned}$$

end if

else

$$\begin{aligned} \xi &= 1 \\ H &= 0 \end{aligned}$$

end if

$$\begin{aligned} \sigma &= E\,[\epsilon - sgn(\epsilon)\,\xi\,\epsilon_L] \\ E^T &= E\,[1 - sgn(\epsilon)\,\epsilon_L\,H] \end{aligned}$$

end if

Table 4.3: Solution scheme for $A \rightarrow S$ phase transformation.

If $\mid \epsilon - \epsilon_n \mid < 0$ then $\Rightarrow$ unloading

$$\begin{aligned}
\epsilon_s^{SA} &= sgn(\epsilon)\,\frac{\sigma_s^{SA}}{E} + sgn(\epsilon)\,\xi_{S,n}\,\epsilon_L \\
\epsilon_f^{SA} &= sgn(\epsilon)\,\frac{\sigma_f^{SA}}{E}
\end{aligned}$$

if $-\mid \epsilon_s^{SA}\mid > \mid \epsilon\mid > \mid \epsilon_s^{SA}\mid$

$$\begin{aligned}
\xi &= \xi_{S,n} \\
H &= 0
\end{aligned}$$

else if $\mid \epsilon_f^{SA}\mid < \mid \epsilon\mid < \mid \epsilon_f^{SA}\mid$

if $\mid \sigma_n\mid > \sigma_s^{SA}$

$$\begin{aligned}
\xi &= \frac{\xi_{S,n}\,E\,\epsilon - sgn(\epsilon)\,\xi_{S,n}\,\sigma_f^{SA}}{-sgn(\epsilon)\,\sigma_f^{SA} + sgn(\epsilon)\,\xi_{S,n}\,E\,\epsilon_L + sgn(\epsilon)\,\sigma_s^{SA}} \\
H &= \frac{sgn(\epsilon)\,\xi_{S,n}\,E}{\xi_{S,n}\,[sgn(\epsilon)\,E\,\epsilon_L] + sgn(\epsilon)\,\sigma_s^{SA} - sgn(\epsilon)\,\sigma_f^{SA}}
\end{aligned}$$

else

$$\begin{aligned}
\xi &= \frac{\xi_{S,n}\,E\,\epsilon - sgn(\epsilon)\,\xi_{S,n}\,\sigma_f^{SA}}{-sgn(\epsilon)\,\sigma_f^{SA} + sgn(\epsilon)\,\xi_{S,n}\,E\,\epsilon_L + \sigma_n} \\
H &= \frac{sgn(\epsilon)\,\xi_{S,n}\,E}{\xi_{S,n}\,[sgn(\epsilon)\,E\,\epsilon_L] + sgn(\epsilon)\,\sigma_n - sgn(\epsilon)\,\sigma_f^{SA}}
\end{aligned}$$

end if

else

$$\begin{aligned}
\xi &= 0 \\
H &= 0
\end{aligned}$$

end if

$$\begin{aligned}
\sigma &= E\,[\epsilon - sgn(\epsilon)\,\xi\,\epsilon_L] \\
E^T &= E\,[1 - sgn(\epsilon)\,\epsilon_L\,H]
\end{aligned}$$

end if

Table 4.4: Solution scheme for $S \rightarrow A$ phase transformation.

Chapter 5

Numerical Simulations

5.1 Introduction

In this section we study the dynamic behavior of SDOF superelastic systems under different types of loading conditions.
In the existing literature few works deal with such numerical problems ([6], [23], [51]) and a small number of studies on the influence of the mechanical characteristics of SMAs in dynamics appear. For this reason the following numerical investigation is aimed at providing an effort to overcome this lack of information.
We consider several cases focusing the attention on the quantities which are of most interest in the field of earthquake engineering. In particular the response of such systems in terms of displacements, velocities and accelerations as well as their dissipation capacity is monitored through a large number of parametric analyses.

5.2 Organization of the numerical tests

We take into consideration different inputs having an increasing level of complexity. In particular, we want both to check in detail the adopted uniaxial model and to understand the mechanical response of SMA systems under dynamic loadings. Accordingly, we numerically study the oscillator subjected to the following conditions:

1. Free vibrations.

2. Pulse loads with fixed frequency and different amplitude levels.

3. Sinusoidal loads with different frequencies and fixed amplitude level.

4. Combined exponential-sinusoidal loads with different amplitude levels.

5. El Centro record scaled to different values of peak ground acceleration.

Besides a discussion, for each case we include several graphs which plot the quantities under investigation. Obviously, in order to be coincise, we present only the ones of most interest.

The SDOF system under consideration is a simple oscillator, axially deforming, with a mass at the free end and a restoring superelastic element connecting the fixed end and the mass itself. In particular, we consider the system with a mass of 100 kg and with a SMA wire of length 1000 mm and diameter equal to 1 mm. We also assume the simplified but very common hypothesis that the restoring element follows the same adopted constitutive rule both in tension and compression, thus ingnoring any problems involving buckling ([6], [23], [35], [34] [41], [51]). In order to have physically understandable results, the chosen geometric and mechanical properties are compatible with those representing a smart bracing system installed in a reduced-scale frame and that we can model as a SDOF structure ([10]).

Mathematically, we need to solve the following nonlinear equation of motion:

$$m\ddot{x} + c\dot{x} + f_s = -m\,\ddot{u}_g$$

being m the mass of the system, c the viscous damping (i.e. $c = 2m\xi\omega$ with ξ the damping ratio and ω the natural frequency of the system) and f_s the restoring force provided by the nonlinear spring element. Obviously, the quantity $\ddot{u}_g$ represents the base acceleration that we are considering. Due to the nonlinear term, the previous equation may be solved thorugh an iterative procedure that links the Newton-Raphson strategy with a numerical method providing the SDOF response in terms of displacements, velocities and accelerations.
For this reason, Appendix B, is completely dedicated to accurately describe all the algorithms needed for the solution of the previous equation. In particular, we implement the simulations in the MATLAB environment using the Newmark predictor-corrector implicit algorithm as integration scheme. To improve the completeness of the parametric study, we also focus the attention on the influence of the SMA's mechanical properties on their dynamic response. In particular, what we want to understand is the effect of both the plateau length and the stress transformation levels. For this reason we basically consider two different types of alloys:

- Alloys exhibiting constant dissipation capacity.
- Alloys exhibiting increasing dissipation capacity.

The first type of alloys is characterized by the same lower plateau stress level, chosen equal to 100 MPa, and with an increasing upper plateau stress level ranged from 300 MPa to 600 MPa with a step interval of 100 MPa.
The second type of alloys, instead, is characterized by increasing values of both

plateau stress levels (from 100 MPa to 400 MPa for the lower one and from 300 MPa to 600 MPa for the upper one respectively) separated by a constant value of stress equal to 200 MPa.
Characteristics[1] of the considered alloys are summarized in Tables 5.1 and 5.2 as well as in Figures 5.1 and 5.2.

Finally, we list the main objectives of the numerical investigation:

- To study the effects of different loading conditions on the dynamic response of pseudoelastic systems.
- To study the influence of the damping ratio as well as to compare the different performance offered by alloys with constant and increasing dissipation capacity.
- To investigate the influence of both the upper plateau stress level and the plateau length.
- To understand the complex nonlinear dynamics resulting from the analysis of such particular hysteretic systems.
- To show the possibility of using SMAs in both recentring and recentring-dissipating devices for seismic applications.

[1] All the mechanical properties assumed for the numerical investigation are absolutely realistic because directly taken from experimental tests conducted on SMA elements reported in the literature and already discussed in Chapter 2.

Alloys	**E** [MPa]	$\boldsymbol{\sigma_s^{AS}}$ [MPa]	$\boldsymbol{\sigma_f^{AS}}$ [MPa]	$\boldsymbol{\sigma_s^{SA}}$ [MPa]	$\boldsymbol{\sigma_f^{SA}}$ [MPa]
SMA 100-300	70000	300	300	100	100
SMA 100-400	70000	400	400	100	100
SMA 100-500	70000	500	500	100	100
SMA 100-600	70000	600	600	100	100

Table 5.1: Mechanical properties of SMAs with constant dissipation capacity.

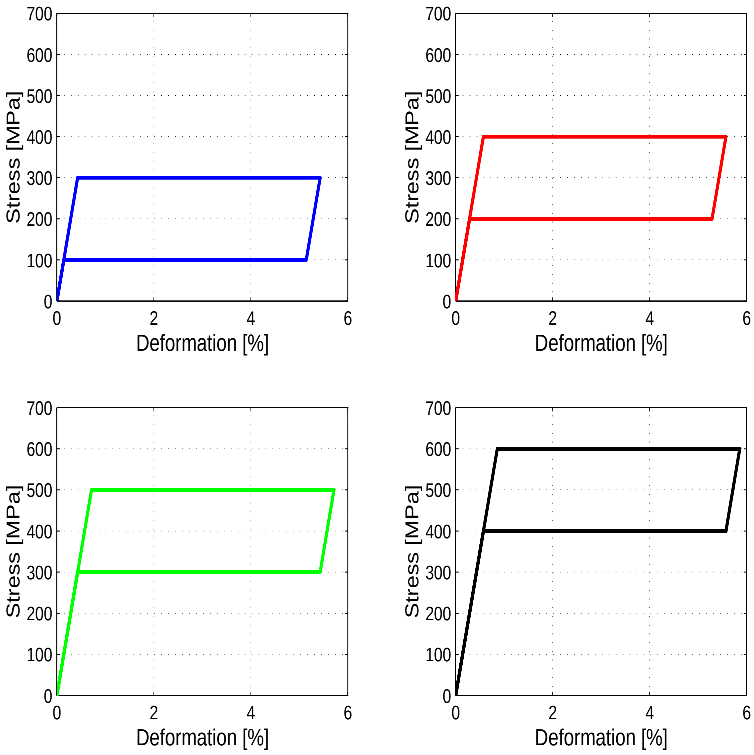

Figure 5.1: Stress-strain relationships of SMAs with constant dissipation capacity. As an example, the plateau length has been considered equal to 5%.

Alloys	**E** [MPa]	σ_s^{AS} [MPa]	σ_f^{AS} [MPa]	σ_s^{SA} [MPa]	σ_f^{SA} [MPa]
SMA 100-300	70000	300	300	100	100
SMA 200-400	70000	400	400	200	200
SMA 300-500	70000	500	500	300	300
SMA 400-600	70000	600	600	400	400

Table 5.2: Mechanical properties of SMAs with increasing dissipation capacity.

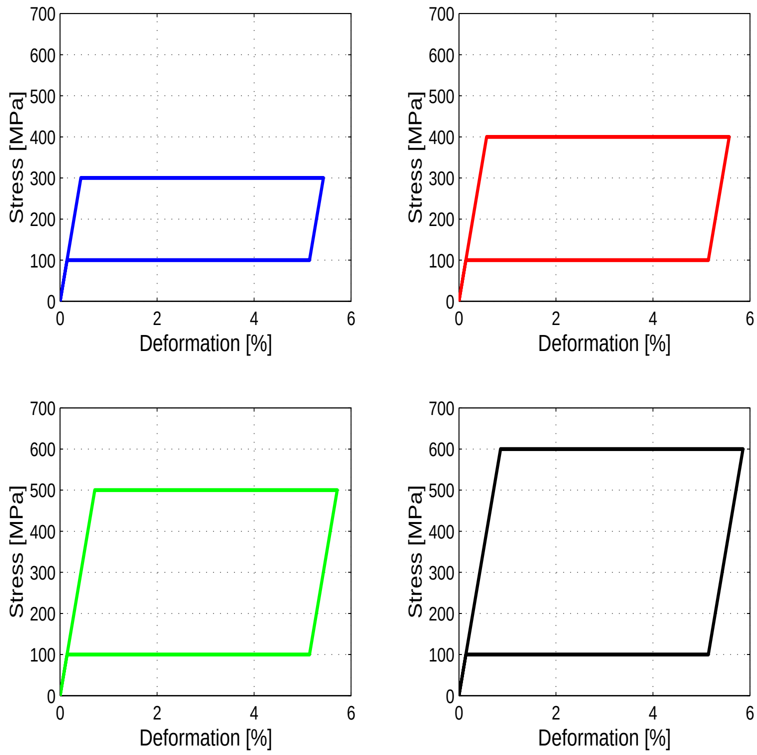

Figure 5.2: Stress-strain relationships of SMAs with increasing dissipation capacity. As an example, the plateau length has been considered equal to 5%.

5.3 Analysis of free vibrations

In this section we study the free vibrations of the SMA superelastic system under investigation. In particular, we impose an initial displacement and we consider no external force acting on it. The level of the given deformation is such that it corresponds to a value of martensite fraction equal to 50%, where the plateau length has been considered equal to 8%. In such a way, we can clearly highlight the ability of the oscillator in attenuating the vibrations through energy dissipation, since it starts its motion just in the middle of the austenite-to-martensite phase transformation. Moreover, we take into account six different values of damping ratio (starting from $\xi = 0$) to study the influence of the dashpot in the response modification. Among the analyzed cases, we restrict our presentation to SMA 100-600 and SMA 400-600 alloys even if many more cases have been considered. The choice of such an upper plateau stress level relies on the fact that it is very common for high strength SMAs ([53]), a class of alloys with mechanical characteristics particularly suitable for applications in earthquake engineering.

As a support of the numerical tests, we present different kinds of plots. First we show the deformation time-history experienced by the oscillator after the release of the imposed displacement (Figures 5.3 and 5.4) then we propose the so called *phase-portrait* (Figures 5.5 and 5.7), which is the phase-space diagram correlating deformation (represented in the x-axis) and velocity (represented in the y-axis) of the system. Finally, we plot the corresponding stress-strain relationships (Figures 5.6 and 5.8) together with the performance of the considered SMAs in attenuating the dynamic response (Figures 5.9 and 5.10).

On the basis of the results we are able to provide the following comments:

- In Figures 5.3 and 5.4 we observe that, as expected, the higher is the value of the damping ratio, the higher is the attenuation of the free oscillations over the considered time period. Moreover, we correctly note that, when the damping ratio is set equal to 0% and after a brief transient response, the system shows a never ending sinusoidal response with the same period of the SDOF system, in perfect agreement with the theoretical solution (see Appendix A for the analytical expression).

- From the same Figures previously considered, it is very evident how alloys exhibiting larger dissipation capacity may strongly attenuate the oscillations than alloys with constant dissipation capacity and with same upper plateau stress level. This feature, which is very important in view of seismic applications, is better seen in Figure 5.9 where we compare the maximum absolute deformation reached by both types of alloys after the release of the initial displacement. The same characteristic is even clearer in Figure 5.10 where we compute the ratio of such values. As we can observe, this factor ranges from a value of about 2.2 to a value of almost 2.5 according to the values of damping ratio chosen for these analyses. By means of this information, we can then hypothize that the value of ξ has little influence on the dissipation capacity of the alloys. More precisily, we may say that the damping effect due to the hysteresis dominates that of the viscous force provided by the dashpot. The previous consideration is in agreement with that proposed by Feng and Li ([23]) during their studies on the dynamic behavior of a SDOF superelastic system.

- The pseudoelastic effect exhibited by the alloys is very evident in Figure 5.7. From the phase-space diagram we note, after the oscillations due to the imposed displacement, no residual deformation then encouraging the use of SMAs for recentring devices. This behavior, instead, might not be exhibited by other metallic materials such as steel, where plastic deformations can never be recovered. Instead, we note a different trend in Figure 5.5 where the motion approaches a limit cycle instead of decaying to zero. This is due to choice of the damping ratio which, for this analysis, has been set equal to zero and that makes the structure vibrate indefinitely. Finally, we observe how the shape of the proposed graphs is in very good agreement with the ones proposed by Seelecke ([51]) who studies the torsional free-vibrations of a SMA bar[2].

- In Figures 5.5 and 5.7 we may still appreciate the different deformation attenuation offered by the compared alloys. It is also possible to note how the graphs are well described, meaning that both the chosen time step and the robustnees conditions of the adopted constitutive material model guarantee a precise numerical integration.

[2]The equation of motion of a SDOF system subjected to torsional free-vibration motions is formally identical to that of the same system experiencing oscillations due to an imposed displacement. The unkwnown function for the former problem is its angle of rotation response while for the latter one is its deformation response.

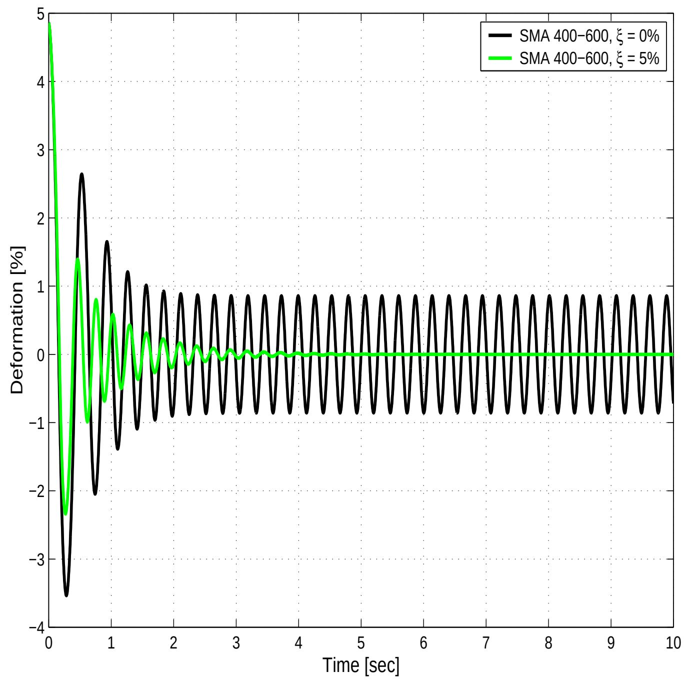

Figure 5.3: Analysis of free vibrations: deformation time-history of the SDOF system for selected values of damping ratio.

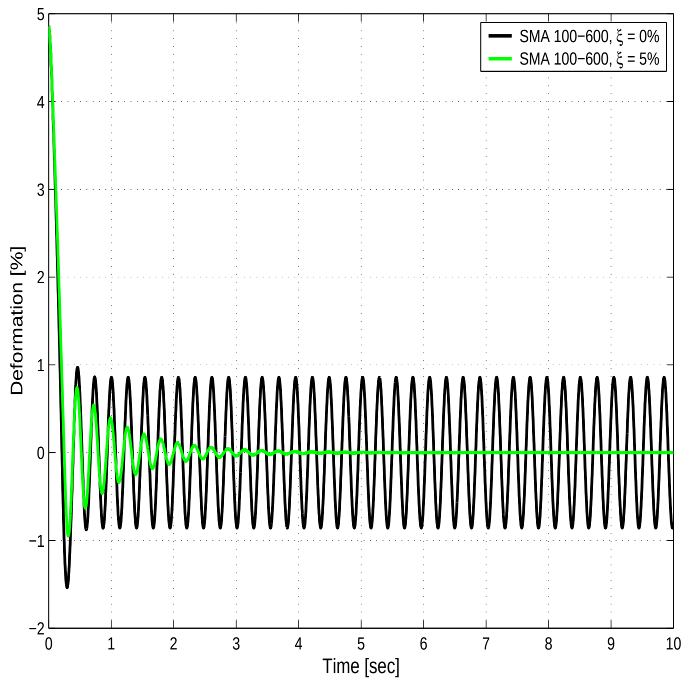

Figure 5.4: Analysis of free vibrations: deformation time-history of the SDOF system for selected values of damping ratio.

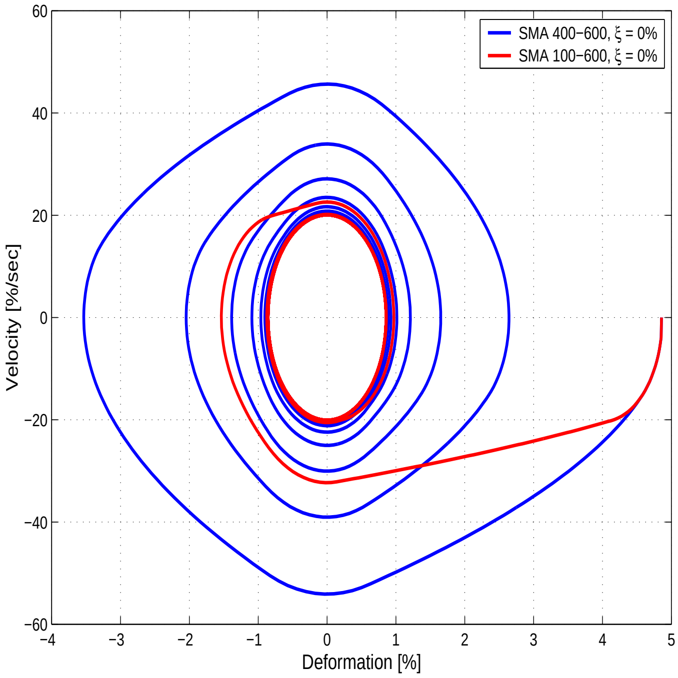

Figure 5.5: Analysis of free vibrations: phase portrait-plot. The value of damping ratio is set equal to 0%.

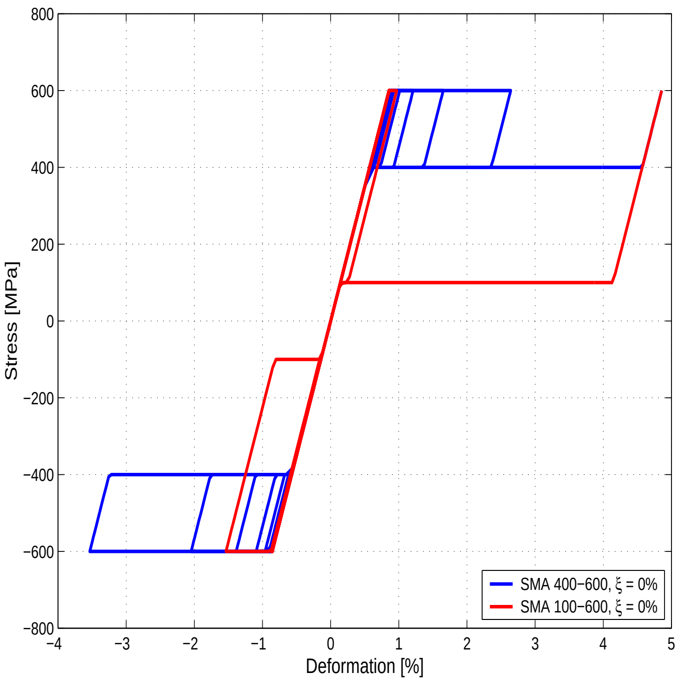

Figure 5.6: Analysis of free vibrations: stress-strain relationship. The value of damping ratio is set equal to 0%.

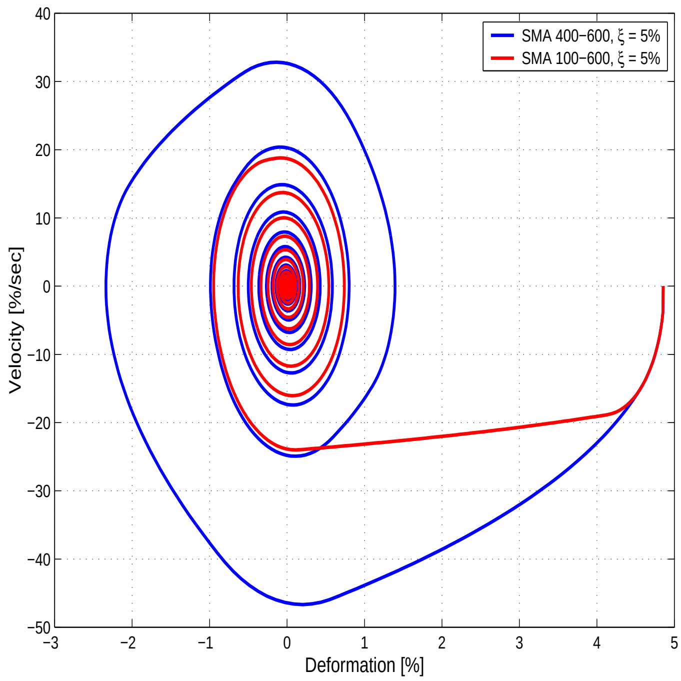

Figure 5.7: Analysis of free vibrations: phase-portrait plot. The value of damping ratio is set equal to 5%.

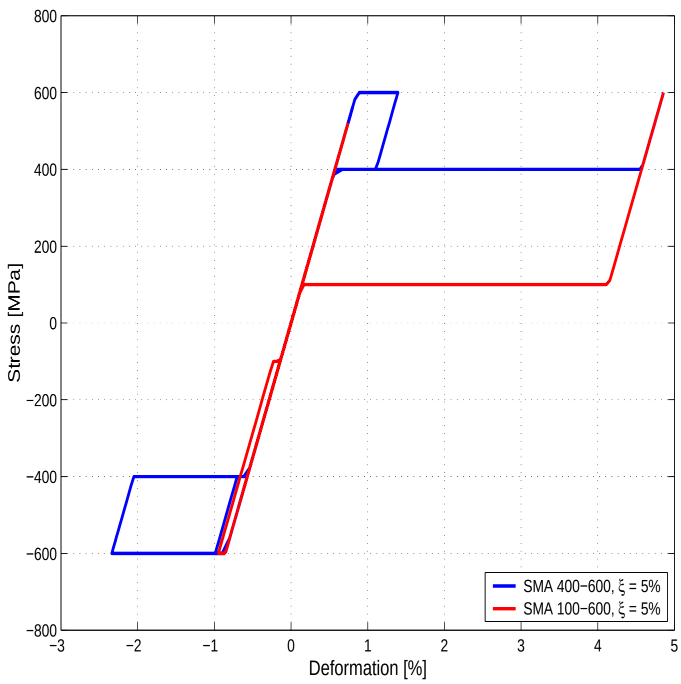

Figure 5.8: Analysis of free vibrations: stress-strain relationship. The value of damping ratio is set equal to 5%.

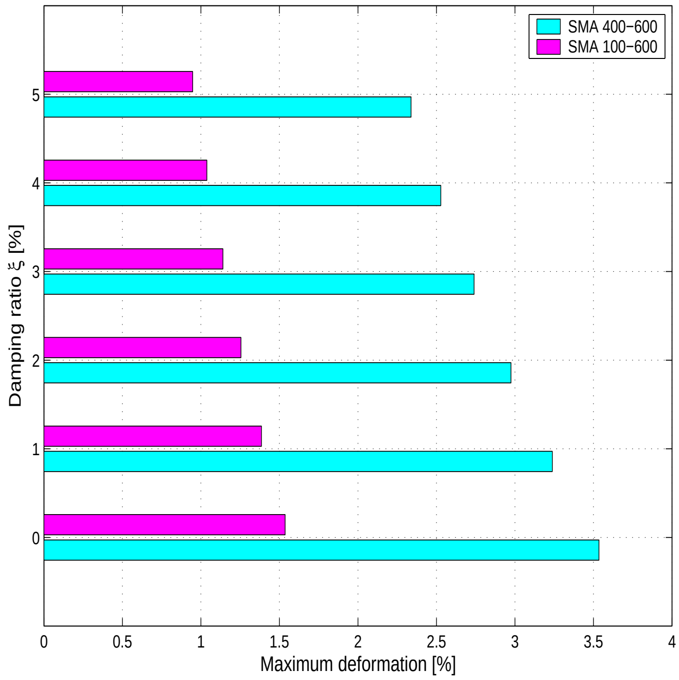

Figure 5.9: Analysis of free vibrations: selected values of damping ratio vs. maximum deformation reached by the SDOF system after releasing the imposed displacement.

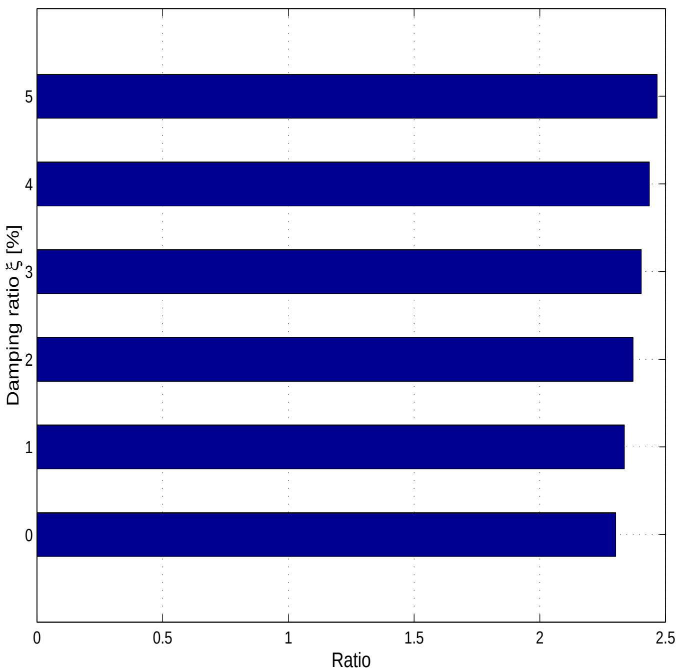

Figure 5.10: Analysis of free vibrations: selected values of damping ratio vs. ratio between maximum deformations reached by the SDOF system after releasing the imposed displacement. Comparison between SMA 400-600 and SMA 100-600 alloys.

5.4 SDOF under pulse loads

In this section we study the response of the SDOF superelastic system subjected to pulse loads. The excitation has an amplitude acceleration level ranging from 0.2g to 0.5g, with a step increment of 0.02g and a duration of 0.5 seconds. As a consequence, the load frequency is 2 Hz (i.e. $\omega = 4\pi$ rad/sec) with a vibration period equal to 0.5 seconds. The adopted choice of load parameters is compatible with the corresponding one selected by other researchers ([16], [18], [20]) studying the dynamic behavior of SMA wires and bars under cyclic loadings. For these analyses we consider five different values of plateau length in order to evaluate the effect of its variation. More precisely, we choose an interval of ϵ_L ranged from 4 to 8%. Also, since we have noticed that the effect of the damping ratio is not so relevant in the energy dissipation mechanism provided by the system, we assume for all analyses a value of ξ equal to 5%, in agreement with that considered by Feng and Li ([23]) for their dynamic studies on a SMA superelastic bar.

In the following we include the most significant graphs examining different quantities under investigation. First, we show the considered load condition for three selected values of peak ground acceleration (Figure 5.11) then we correlate the maximum absolute deformation attained by the system according to both the considered acceleration levels and plateau lengths (Figures 5.12 and 5.13). Lastly, as an example, we show the deformation ratio of the peak response reached by SMA 300-500 and SMA 100-500 alloys (Figure 5.14) as well as their ductility demand (Figures 5.14 and 5.16).

After analyzing the obtained results we propose the following observations:

- Alloys with increasing dissipation capacity do provide larger response attenuation. This phenomenon is clearly seen in Figure 5.13 where we note that the maximum deformation level reached during the pulse load is lower for such SMAs. In particular, we observe that the higher is the acceleration level, the higher is the ability of the SMA element to reduce its motion. Furthermore, as we expected, for very low load amplitudes, we identify an almost coincidence of each pair of curves. This fact happens because, in such a range, the SMA element is hardly stretched or compressed and behaves, in practice, elastically. We observe this feature for all different plateau lengths considered which, obviously, do not affect the overall behavior for such low acceleration levels. Important characteristic to note, is the slope change of all curves for high amplitude levels of excitation. This is due to the fully transformation of the material in martensite which provides additional stiffness then limiting the deformation. This peculiarity may be very useful in seismic applications in order to have a complete displacement control when dealing with unexpected strong earthquakes. Finally, we notice that the longer is the plateau length, the higher is the deformation level. In such cases the complete transformation from austenite to fully martensite origins later and consequently the slope change is less evident.

- In Figure 5.14 we present a three-dimensional plot highlighting the different energy dissipation performance exhibited by the considered alloys. As an example, we only refer to SMA 300-500 and SMA 100-500 alloys, because for the other types the same considerations yield. We introduce the term displacement ratio, meaning the ratio between the maximum absolute deformation value undergone by SMAs with constant dissipation capacity and the corresponding one related to alloys with increasing dissipation capacity and with the same upper plateau stress level. We may observe that the higher is the plateau stress level, the larger is the amplitude range for which the ratio is equal to one. This feature is to be attributed to the influence of the upper plateau stress level, which may keep the system moving elastically for low intensity loads. Obviously, in this particular case, the energy dissipation capacity of the alloys do not influence the dynamic response because both SMA families never experience inelastic deformations. Neverthless, we can notice remarked reductions in the displacement ratio through a discontinuity observed in the plots. By comparison with the graphs related to the other alloys that, again, we do not include for brevity, we may note that this discontinuity seems to move towards higher amplitude values of the external acceleration as the upper plateau stress level considered increases. The explanation is not easy to give but should be connected to the different volume of martensite fraction generated during the excitation. In fact, it seems that the ratio between the maximum deformations undergone by alloys which are in their fully martensitic phase is lower than the corresponding ratio related to alloys where the phase transformation may be not complete. Physically, this characteristic appears correct, because for the same value of force increment acting on the mass, the consequent deformation will be much lower for an alloy in its fully martensitic phase than that of an alloy in its pseudoelastic state.

- Figures 5.15 and 5.16 show how the amplitude excitation level and the different plateau lengths considered influence the ductility demand. With the term ductility we mean the ratio between the maximum absolute deformation experienced by the oscillator during its motion and the corresponding value at which the forward transformation starts. We note that the ductility demand is always higher for alloys with constant dissipation capacity than for the other type of alloys, confirming what already discussed in the previous point. In fact, SMAs with such characterics allow for larger values of deformation response.

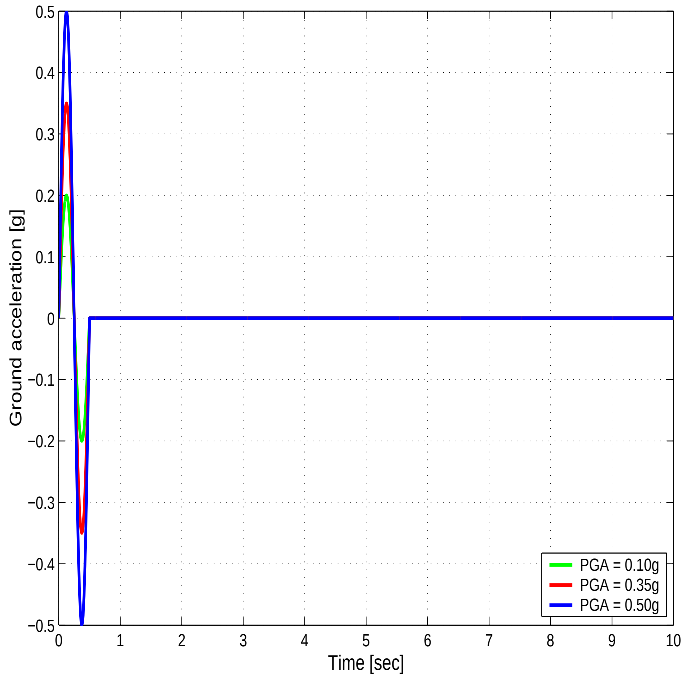

Figure 5.11: Examples of acceleration time-histories of the pulse load condition.

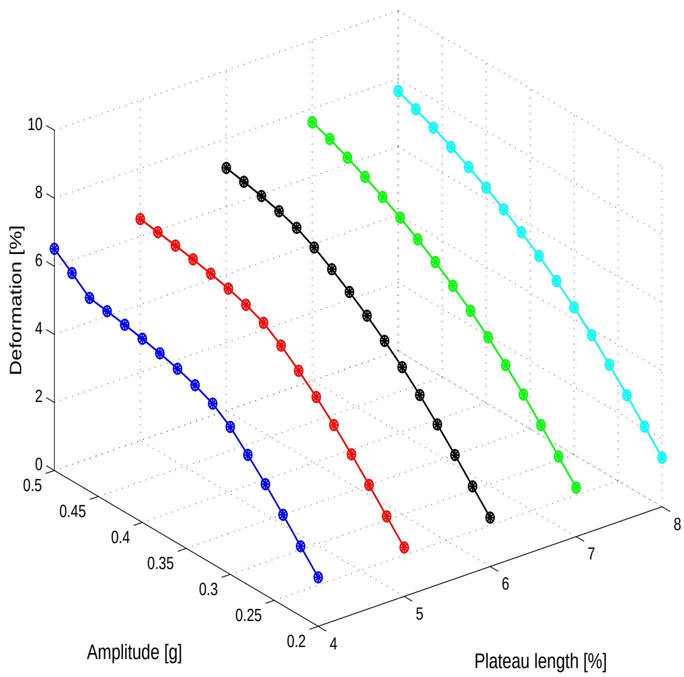

Figure 5.12: SDOF system under pulse loads: maximum deformation levels of SMA 100-300 alloys.

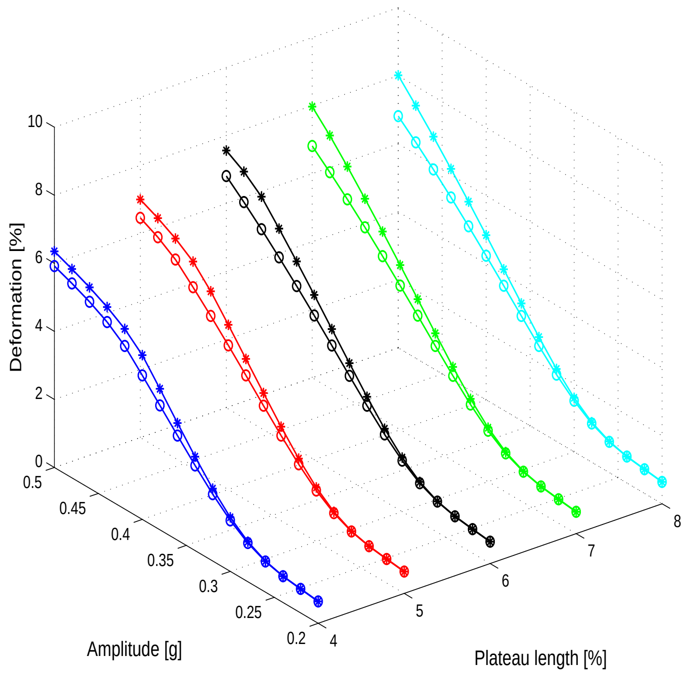

Figure 5.13: SDOF system under pulse loads: maximum deformation levels of SMA 100-500 alloys (lines with circles) and of SMA 300-500 alloys (lines with asterisks).

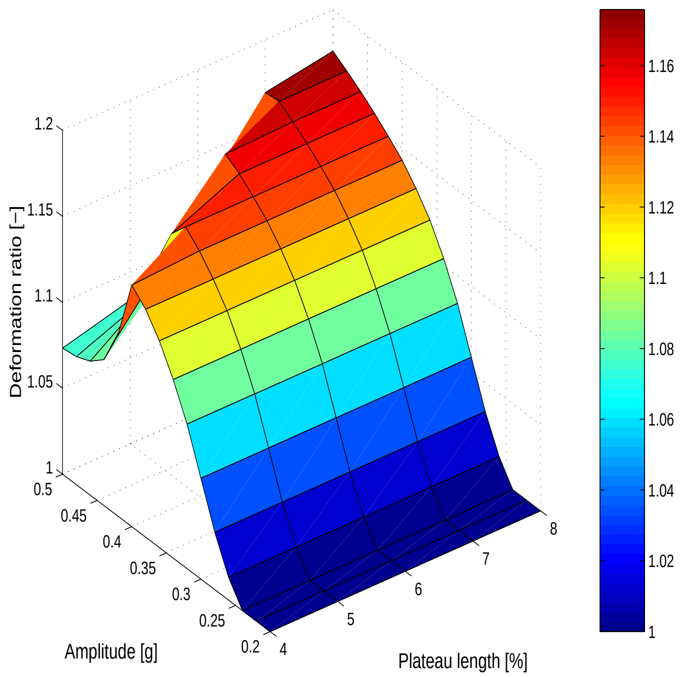

Figure 5.14: SDOF system under pulse loads: deformation ratio between SMA 300-500 and SMA 100-500 alloys.

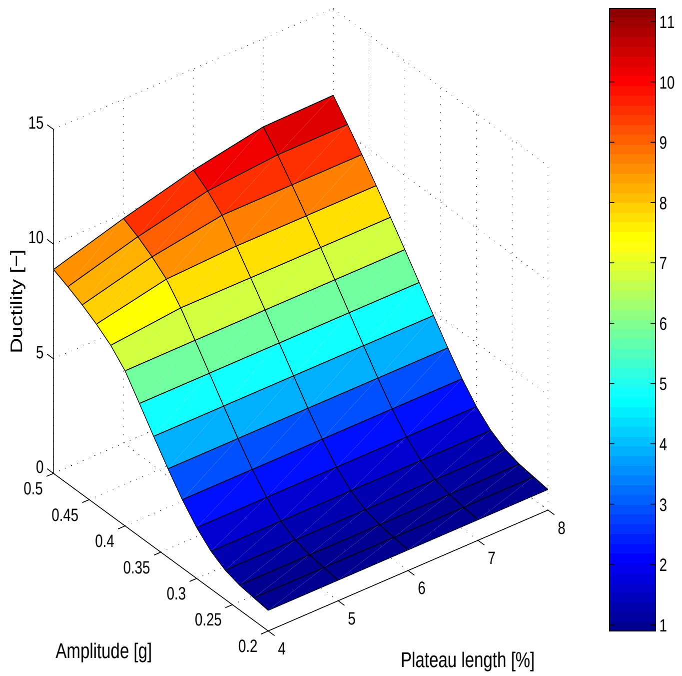

Figure 5.15: SDOF system under pulse loads: ductility demand of SMA 300-500 alloys.

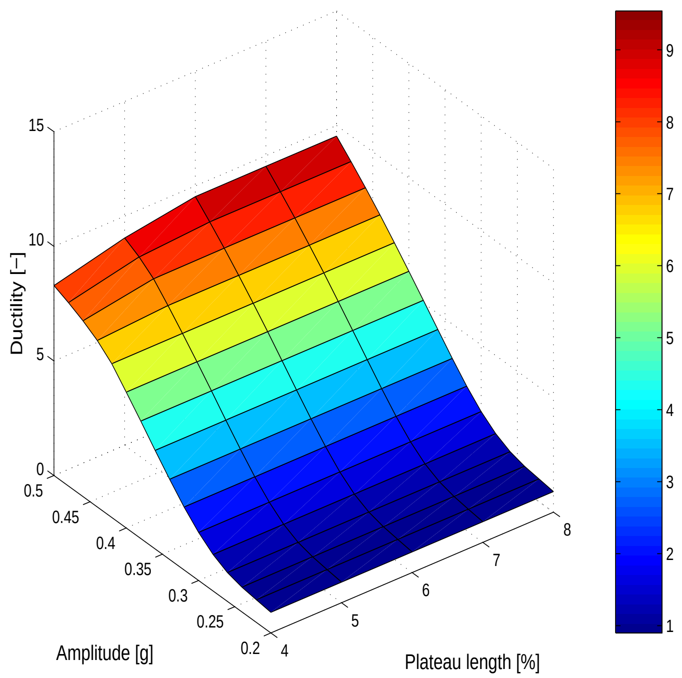

Figure 5.16: SDOF system under pulse loads: ductility demand of SMA 100-500 alloys.

5.5 SDOF system under sinusoidal loads

In the following, we consider the SDOF system as excited by sinusoidal accelerations (i.e the load is obviously still sinusoidal) of different period. In particular we consider a period interval ranged from 0.1 to 2 seconds and a signal amplitude of 0.1g. Since we do not have any specific information regarding the damping ratio, we choose ξ equal 5% which is the same value considered by Feng and Li ([23]) to solve very similar dynamic problems.

Besides two examples of ground accelerations (Figure 5.17) and the different energy dissipation ability offered by the two families of the considered alloys (Figure 5.18), for the load condition under study we tipically present spectrum-like graphs. In particular, we plot maximum absolute displacements (Figures 5.19 and 5.20), velocities (Figure 5.21 and 5.22) and accelerations (Figures 5.23 and 5.24) in terms of normalized values as functions of the acceleration periods. More precisely, the acceleration periods are scaled by the period of the SDOF system and the response quantities are divided by the maximum ones of the corresponding linear system. Also, to avoid dealing with results particularly affected by the transient response (which strongly influences the dynamic behavior of a system), we only concentrate on the steady-state response which for sinusoidal loads is still sinusoidal ([10], [11]).

We now list and explain the most important considerations made after analysis of the results:

- In all simulations we note jumps in the response, a phenomenon connected to the presence of *saddle points*. In fact, in such points, for the same value of acceleration period we find two different stable solutions. This mathematical characteristics has also been observed by other authors studying very similar problems ([6], [23], [40]). Bifurcations of the response (i.e. coexistence of multiple solutions) have also been experimentally noted after performing torsion tests on SMA wires ([58]) and flexural tests on a SMA beam ([12]). Furthermore, the available literature ([6], [40]) demonstrates that the numerical results of such problems are in excellent agreement with the corresponding ones obtained using more complicated methods such as the *harmonic balance method* or the *equivalent linearization method*, which have also the ability to capture the unstable branches of the solution.

- We observe that at high acceleration periods the numerical results agree with the linear theory. This because, in such a range, the inertia of the mass is negligible and the SMA element is hardly stretched or compressed. The same behavior is also noticed for very low acceleration periods.

- Looking at the graphs concerning the normalized displacements (Figures 5.19 and 5.20), we see a shift of the peak response towards the longer period region. This effect is due to the reduction of stiffness experienced by the material during the phase transformation from austenite to martensite, where it appears to be softer. Also, as expected, the higher is the strength of the material (i.e. higher upper plateau stress level), the smaller is the shift because of the increase of the equivalent stiffness[3].

- SMAs with increasing dissipation capacity and SMAs with constant dissipation capacity do show differences in the displacement response (see again Figures 5.19 and 5.20). More precisely, for the same upper plateau stress level the former have the ability to reduce the oscillation level up to about 20% with respect to the latter. This feature is obviously connected to the larger hysteresis loops that such alloys may provide. The same observation can be made for the velocity response as well where, as in the previous case, the higher is the upper plateau stress level, the stronger is the attenuation. On the other hand, we note a different trend when considering the acceleration response. In particular, we observe that both types of alloys give a peak value very similar. This is better seen in Figure 5.18 where, for each considered quantity, we compute the ratio of the maximum absolute values provided by the two families of alloys under study.

[3]The term *equivalent stiffness* is usually employed in earthquake engineering applications when dealing with materials showing an elasto-plastic constitutive law. In particular, once a target displacement has been imposed, the slope of the line connecting the origin of the force-displacement relationship with the force value associated to the fixed displacement is called equivalent stiffness. In our case, even the material model is quite different, we give that terminology the same meaning. It would be very easy to show that, given two SMA materials with a different value of upper plateau stress level and once a particular value of displacement is chosen, the alloy with a lower forward transformation stress exhibits a lower value of equivalent stiffness and consequently a longer vibration period.

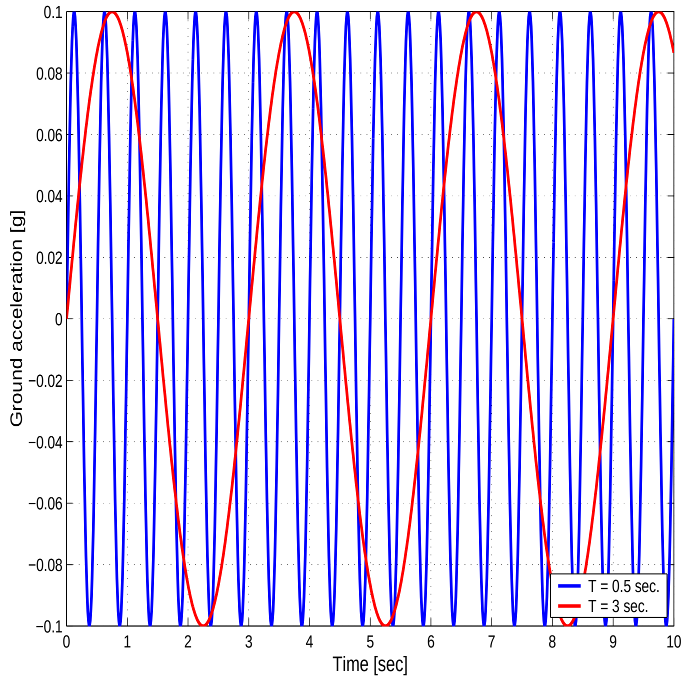

Figure 5.17: Examples of acceleration time-histories of the sinusoidal load condition.

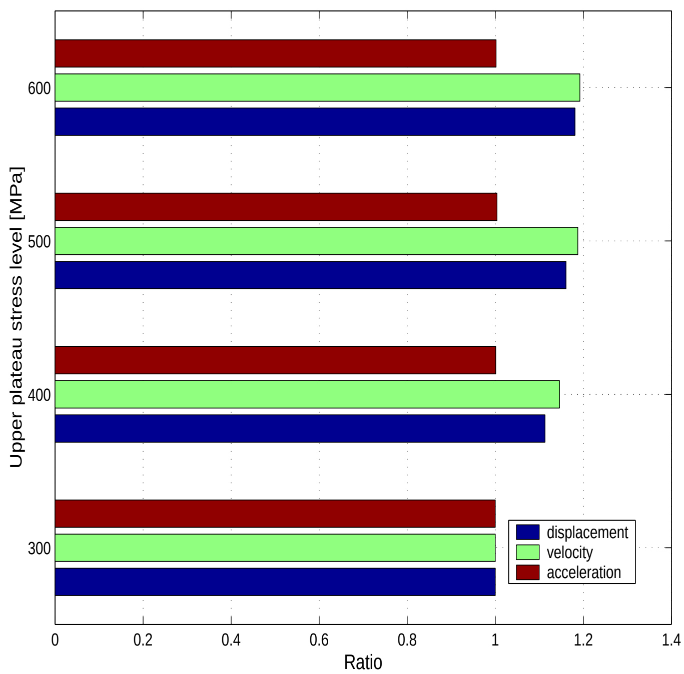

Figure 5.18: SDOF system under sinusoidal loads: upper plateau stress level vs. response peak value ratio between SMAs with constant dissipation capacity and SMAs with increasing dissipation capacity.

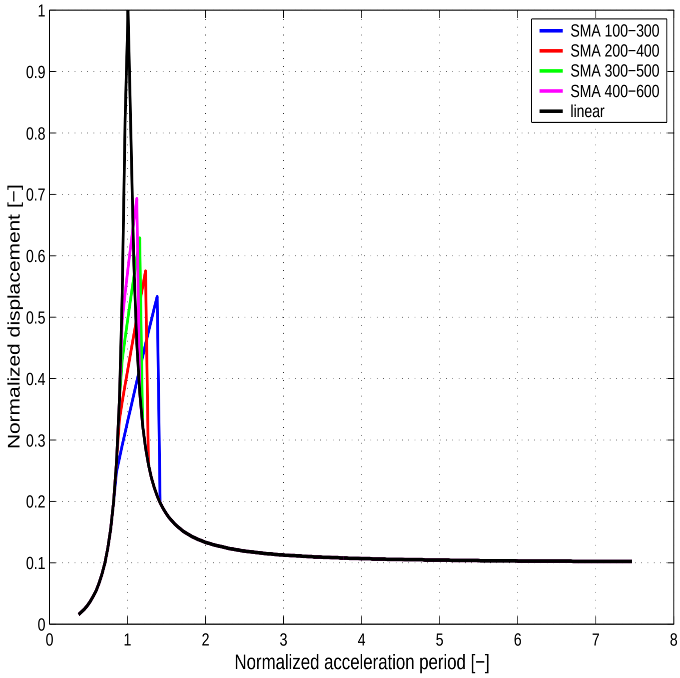

Figure 5.19: SDOF system under sinusoidal loads: normalized displacement vs. normalized load period. Simulations related to SMAs with constant dissipation capacity.

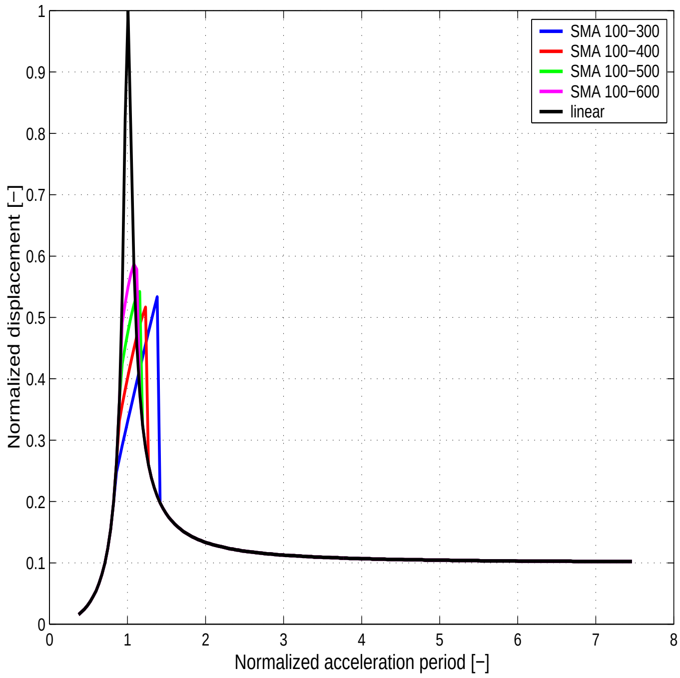

Figure 5.20: SDOF system under sinusoidal loads: normalized displacement vs. normalized load period. Simulations related to SMAs with increasing dissipation capacity.

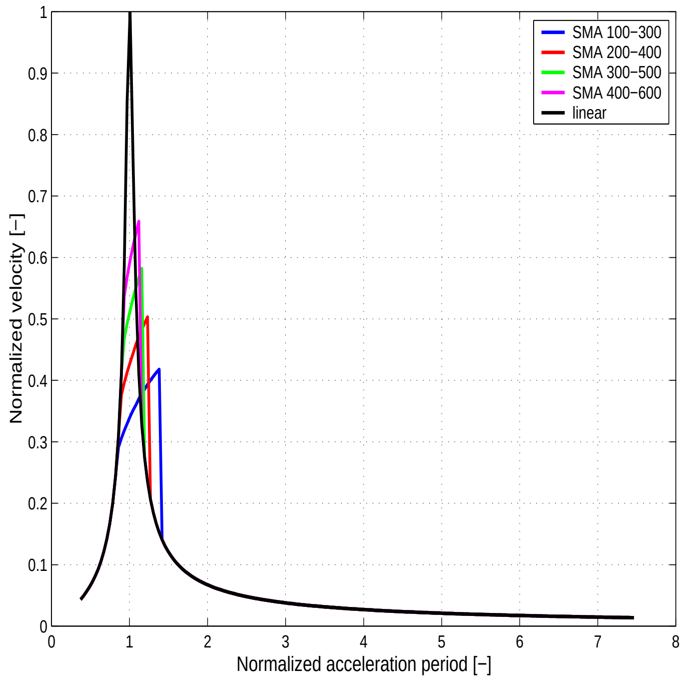

Figure 5.21: SDOF system under sinusoidal loads: normalized velocity vs. normalized load period. Simulations related to SMAs with constant dissipation capacity.

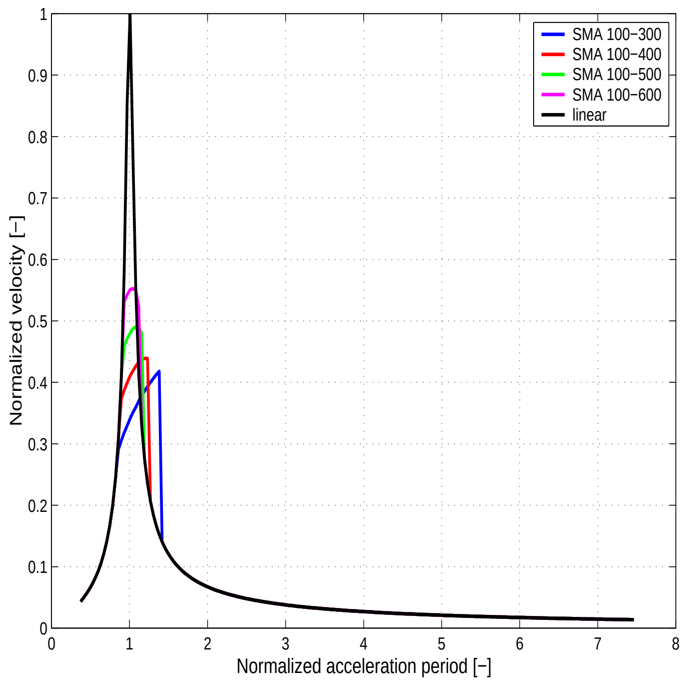

Figure 5.22: SDOF system under sinusoidal loads: normalized velocity vs. normalized load period. Simulations related to SMAs with increasing dissipation capacity.

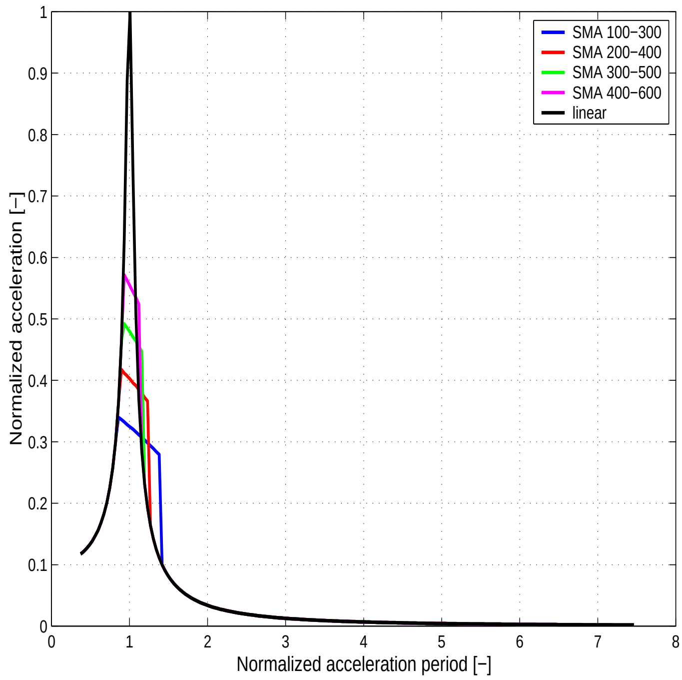

Figure 5.23: SDOF system under sinusoidal loads: normalized acceleration vs. normalized load period. Simulations related to SMAs with constant dissipation capacity.

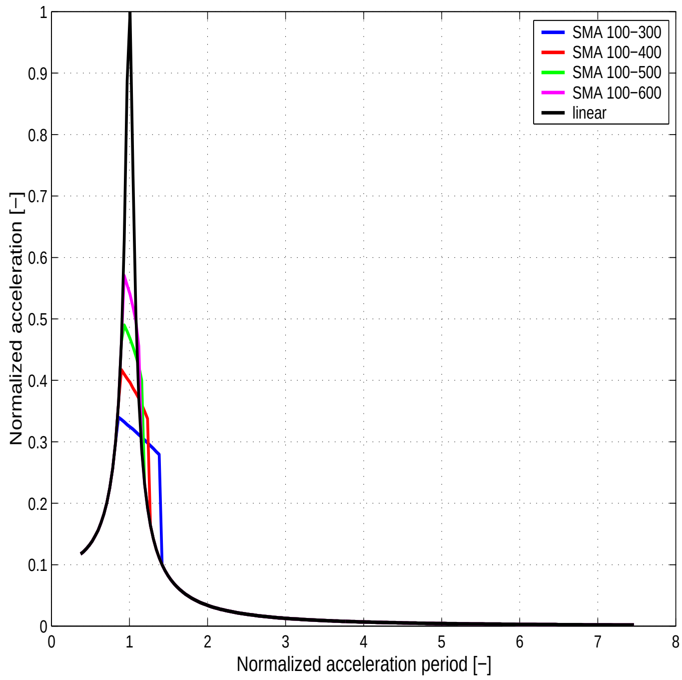

Figure 5.24: SDOF system under sinusoidal loads: normalized acceleration vs. normalized load period. Simulations related to SMAs with increasing dissipation capacity.

5.6 SDOF under exponential-sinusoidal loads

In this section we cosider the SDOF system subjected to exponential-sinusoidal loads of different amplitude levels. Following Corbi ([13]), for the base excitation we choose:

$$\ddot{u}_g = \alpha\, g\, (\sin \omega_1\, t + \sin \omega_2\, t) \exp\left(-\lambda\, t\right)$$

with $\omega_1 = 10$ rad/sec, $\omega_2 = 10$ rad/sec, $\lambda = 5/T$ and T = 5 seconds.
We consider the parameter α (dimensionless) as ranging from 0.1 to 1 with a step increment of 0.1. In [13] it only assumes a value equal to 0.5 to which corresponds a value of peak ground acceleration of about 0.28g. As in the previous section, we restrict our parametric investigations by considering a value of damping ratio equal to 5%. Moreover, for comparison purpose, we also focus the attention on the deformation response of elastic-perfectly-plastic members made of steel (we choose a modulus of elasticity of 210000 MPa), with the same inelastic stress level of the SMA ones (i.e. the upper plateau stress level) and with the same mass. We also consider both systems as having the same vibration period (i.e. the same axial stiffness).

Form the numerical tests, we present different graphs to better point out the most important considerations. Besides three cases of acceleration time-histories (Figure 5.25) and the relationship between α and the peak ground acceleration (Figure 5.26), we show the maximum absolute deformation reached by the system during the shaking (Figures 5.27 and 5.28). Moreover, for the presented example, we consider the ductility demand (Figures 5.29 and 5.30) and the corresponding stress-strain relationship (Figures 5.31 and 5.32). Finally, we show the evolution of the martensite fraction during the ground motion (Figure 5.33) as well as the displacement time-history (Figure 5.34).

In the following, we report the most important points of discussion:

- From Figures 5.27 and 5.28 we see that, when the load amplitude is low, all curves related to SMAs are coincident with the linear case. This behavior is due to the fact the the alloys have not started the phase transformation yet and consequently they are only moving on the linear branch of their constitutive model. On the other hand, elasto-plastic systems (i.e. indicated with the acronym EPP) go to the inelastic phase even for extremely low values of excitation levels with permament deformations which keep accumulating. Also, as expected, the bigger is the damping ratio, the more pronounced is the attenuation response.

- The response offered by SMA elements does not always follow a predictable trend and this feature is probably inferred by the complex dynamics of such hysteretic materials. Anyway, we still find that alloys with increasing dissipation capacity may attenuate the oscillations, especially for high load amplitude levels. With respect to elasto-plastic elements, the overall behavior of such types of SMAs is excellent for low values of peak ground acceleration and good for high values. In fact, in the first case the deformation is strongly reduced while in the second one is quite similar. Anyway, it is important to remind that for any kind of base acceleration applied to the system, only pseudoelastic devices may guarantee the recentring of the structure.

- The plateau length influences the dynamic response especially for high values of load amplitudes. In agreement with the expectations, the higher is the value of ϵ_L, the larger is the maximum deformation and the lower is the martensite fraction generated inside the material. For this reason, the additional stiffness provided by the fully martensite behavior activates later with a consequent increase in displacement.

- In Figures 5.29 and 5.30 we plot the ductility demand (for the definition the reader may refer to page 67) required by the considered SMAs according to different acceleration levels and plateau lengths. Alloys with increasing dissipation capability require less ductility demand, which is more prounced as the upper stress plateau level increases. This behavior is due to their higher energy dissipation mechanism which make the structure experience lower deformation levels. Also, as highlighted by Figure 5.34, they have the ability to substantially reduce the overall time-history response if compared to alloys with constant dissipation capacity and with the same upper plateau stress level.

- We report an example of stress-strain relationship exhibited by SMAs and steel in Figures 5.31 and 5.32. For the selected characteristics, both types of oscillators undergo a very similar value of maximum absolute displacement even if, as clearly visible, the energy dissipation mechanism (i.e. the shape of the hysteresis loops) is very different. Finally, in Figure 5.33, we once again may observe the different performance offered by the two families of SMAs (for brevity we have included only one picture). The martensite fraction generated in alloys with constant dissipation capacity is higher than that possessed by the other set of SMAs because of their reduced ability to damp the oscillations.

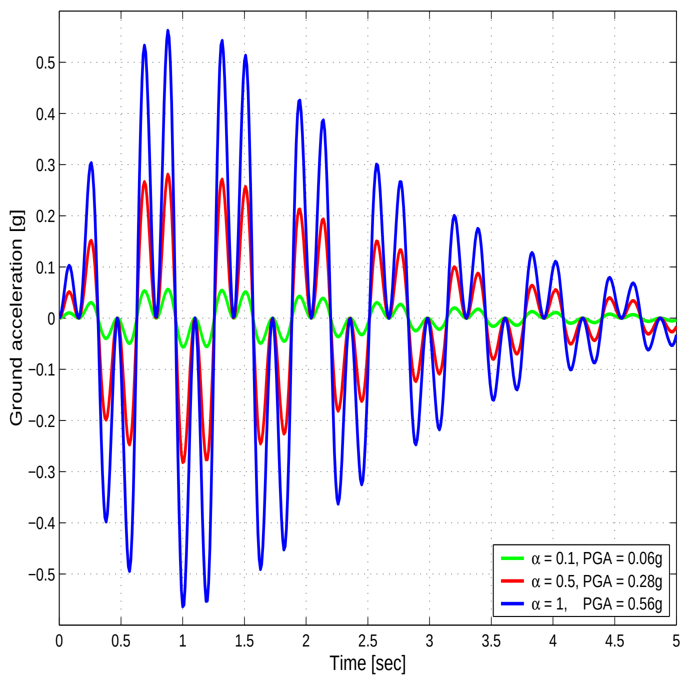

Figure 5.25: Examples of acceleration time-histories of the exponential-sinusoidal load condition.

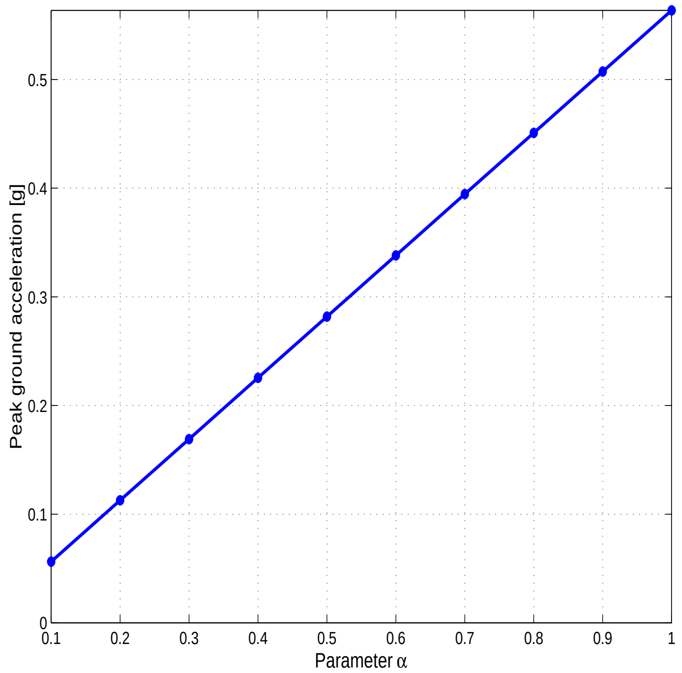

Figure 5.26: Relationship between parameter α and peak ground acceleration.

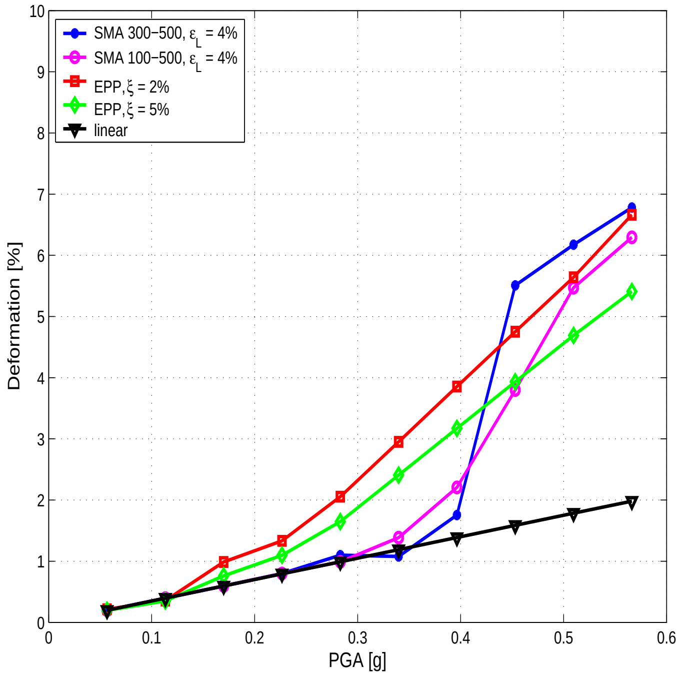

Figure 5.27: SDOF system under exponential-sinusoidal load: maximum deformation reached during the ground excitation.

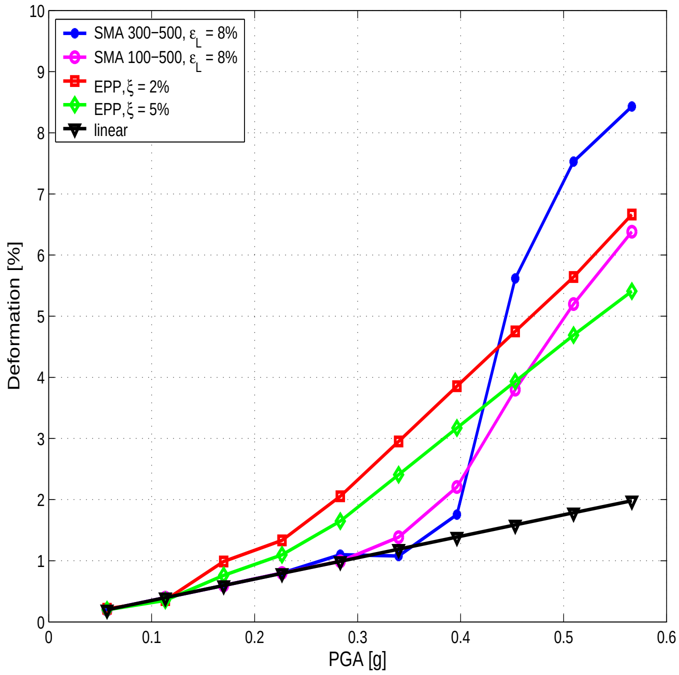

Figure 5.28: SDOF system under exponential-sinusoidal load: maximum deformation reached during the ground excitation.

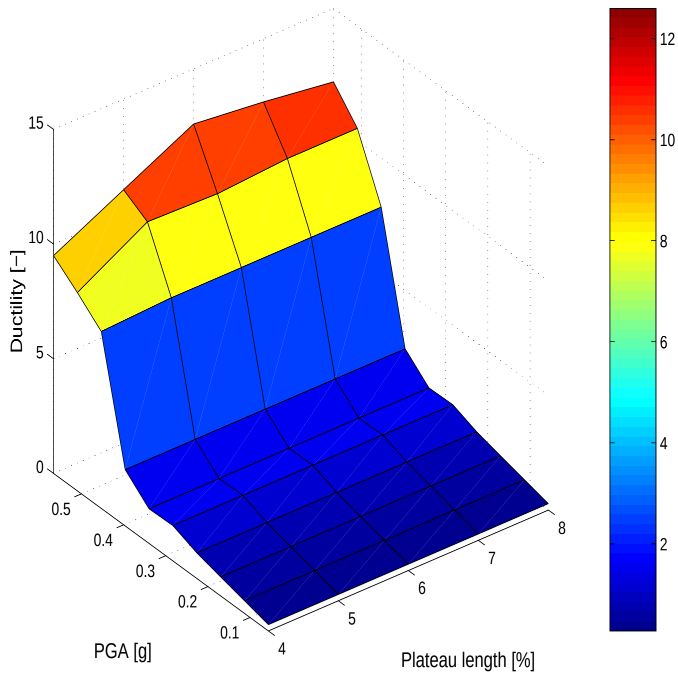

Figure 5.29: SDOF system under exponential-sinusoidal loads: ductility demand of SMA 300-500 alloys.

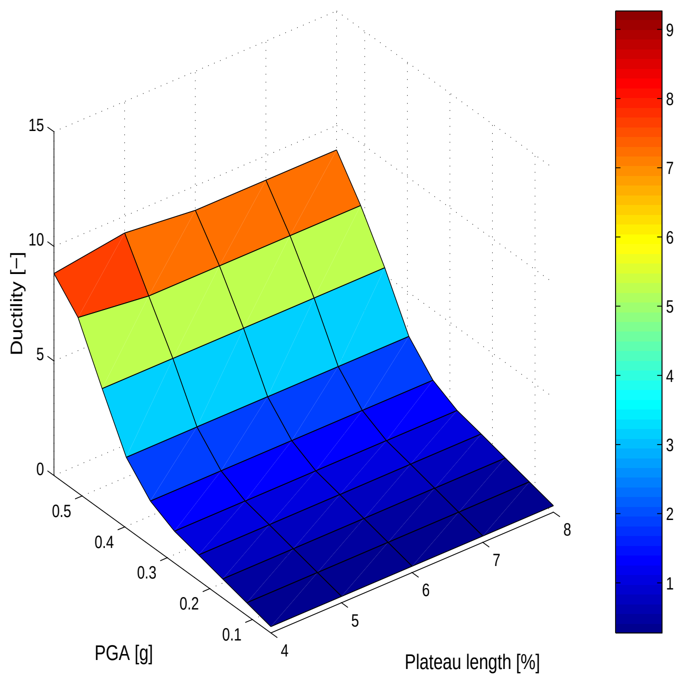

Figure 5.30: SDOF system under exponential-sinusoidal loads: ductility demand of SMA 100-500 alloys.

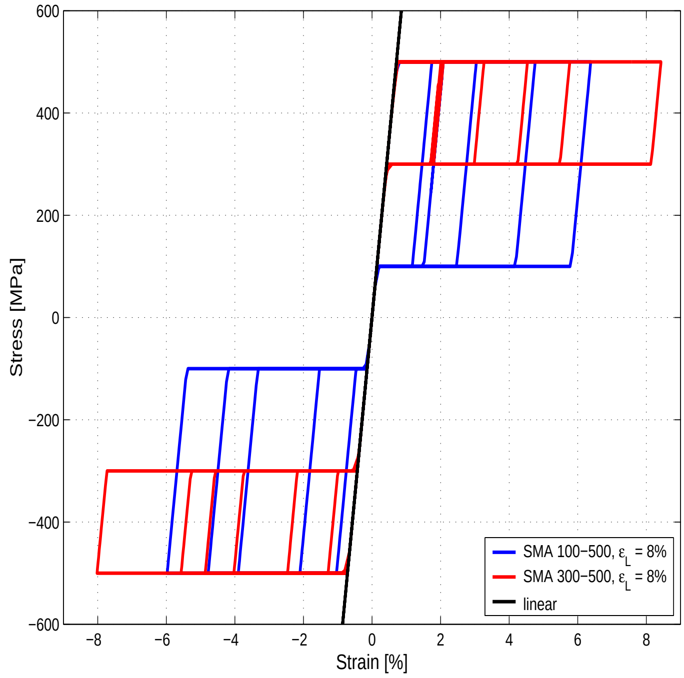

Figure 5.31: SDOF system under exponential-sinusoidal loads: example of stress-strain relationship obtained by imposing $\alpha = 1$.

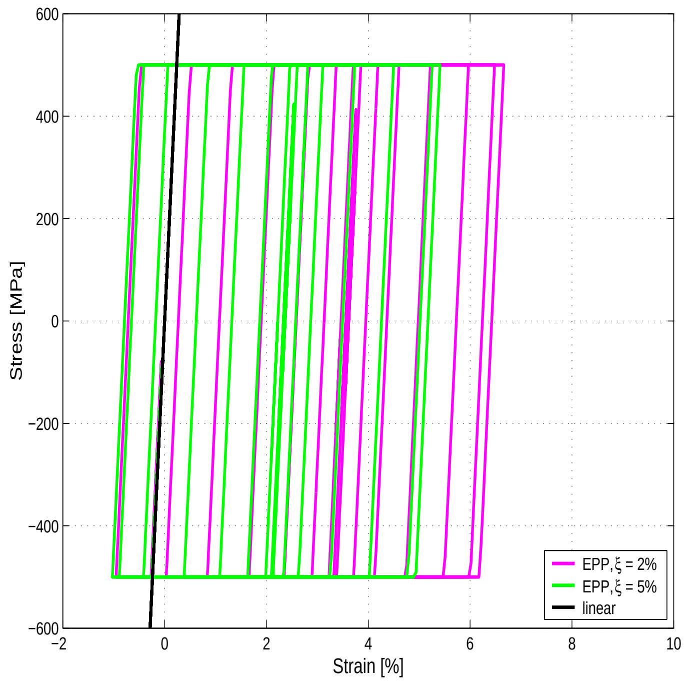

Figure 5.32: SDOF system under exponential-sinusoidal loads: example of stress-strain relationship obtained by imposing $\alpha = 1$.

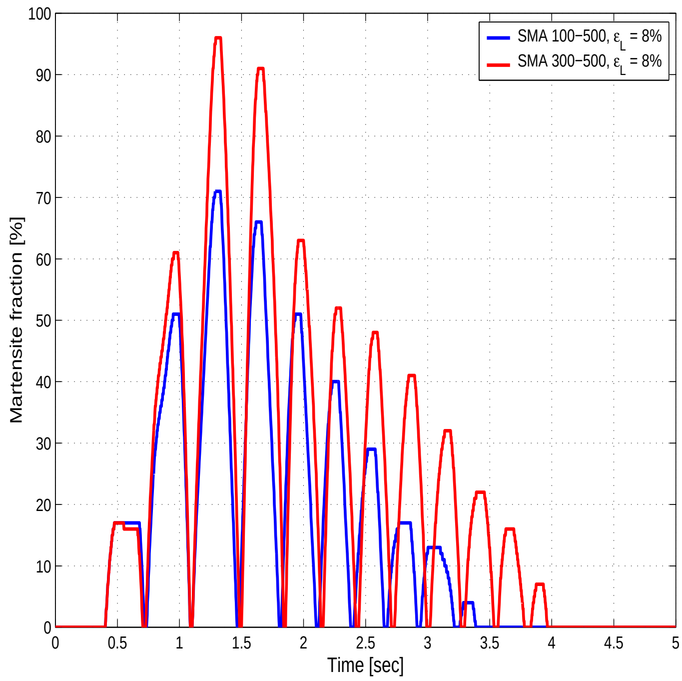

Figure 5.33: SDOF system under exponential-sinusoidal loads: evolution of the martensite fraction obtained by imposing $\alpha = 1$.

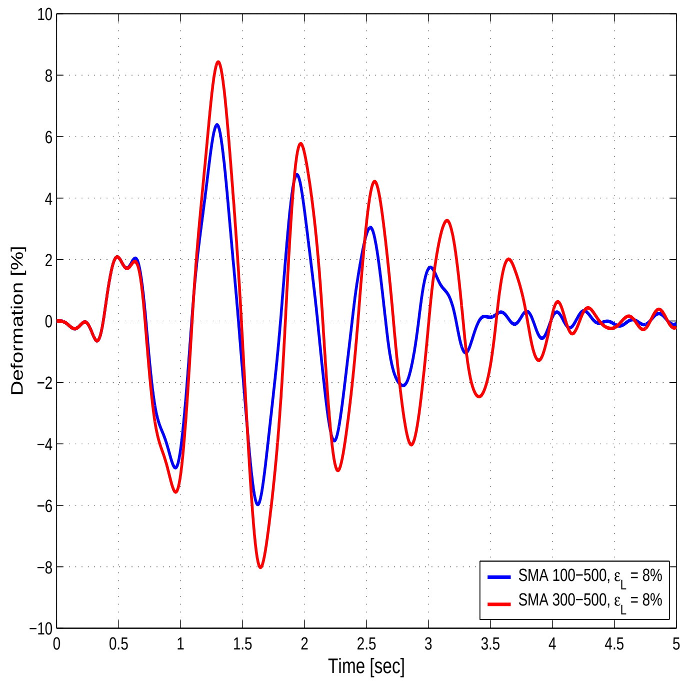

Figure 5.34: SDOF system under exponential-sinusoidal loads: deformation time-history obtained by imposing $\alpha = 1$.

5.7 SDOF under El Centro ground motion

In this section we evaluate the seismic response of pseudoelastic systems under the very well known El Centro ground motion ([10]) scaled to different values of peak ground acceleration. In particular, we consider an amplitude interval ranged fron 0.2g to 0.4g with increments of 0.05g. For such tests we assume a unique value of plateau length equal to 4%, which is intentionally chosen low to guarantee a good displacement control in case of very high seismic forces. Again, the value of damping ratio is considered equal to 5% as in the previous analyses.

From the performed tests we present, as ususal, different plots. We first show one of the considered acceleration time-history (Figure 5.35) and then we provide an example of stress-strain relationship exhibited by the oscillator during the shaking (Figure 5.36). Finally, for both sets of alloys, we include the maximum absolute deformation (Figures 5.37 and 5.38) and the corresponding martensite fraction (Figures 5.39 and 5.40) of the system for the selected levels of peak ground acceleration.

After the analysis of the numerical results, we give the main conclusions in the following:

- From Figures 5.37 and 5.38, as already noticed in the previous section, we see that SMAs with increasing dissipation capacity better attenuate the deformation response than alloys with constant dissipation capacity. This characteristic is very evident for the highest values of excitation levels considered, while it is not so remarked for the lowest ones. The explanation could be attributed to the small hysteresis loops generated during the shaking and such that it does not permit to distiguish the different capacities provided by SMAs to dissipate energy. We also justify this hypothesis by looking at Figures 5.39 and 5.40. It is clearly seen that, for low load amplitudes, all alloys possess, in practice, a very small percentage of martensite.

- When we consider high values of peak ground acceleration, we note that the upper plateau stress level plays an important role in the energy dissipation mechanism. Obviously, for the same load amplitude, the higher is this level, the lower is the possibility of the martensitic phase to form. By still looking at the Figures 5.37 and 5.38, it appears that when, either the considered alloys possess a high stress value to initiate their forward transformation, or the load amplitude is particularly small, the hysteresis does not affect the response attenuation too much. As an example, we can focus the attention on the case in which the peak ground acceleration is 0.35g. There seems to be no difference in considering the system deformation using SMA 300-500 or SMA 100-500 alloys as well as SMA 100-600 or SMA 400-600 alloys. This effect is in agreement with the consideration we have given at the beginning of this section. For this base acceleration level, the upper plateau stress is the first responsible for the response attenuation despite the fact that SMA 100-500 and SMA 100-600 alloys may provide a larger dissipation loop. To further proof this phenomenon, we also present in Figure 5.36 a graph showing the hysteresis cycles created, for the same amplitude of 0.35g. It is possible to observe the good description of each path, meaning that the time step chosen for the integration is small enough to capture the correct behavior of the material model without losing accuracy.

- As easily comprensible, not always the plateau length does provide change in the response. In fact, for the range of peak ground acceleration chosen for this investigation, the plateau length does not affect the results. More precisely, with the choice of ϵ_L made for the tests, the system never transformates in fully martensite (see again Figure 5.37 and 5.38) and consequently other analyses with higher values would have been meaningless. Anayway, in order to better clarify this behavior, some of them have been run. Apart from the obvius reduction of martensite fraction for increasing level of plateau length, we have not noted any difference in the analyzed quantities.

- As a final comparison, even if we have not included the plots for brevity, we have also taken into consideration the use of a steel system with the same vibration period and with an yielding value equal to the upper plateau stress level of the corresponding SMA. Again, despite the larger dissipation capacity of a material exhibiting an elasto-plastic consitutive model, we observe high values of permament deformation which cannot be recovered. For this reason, in view of seismic applications, it is possible to think of a protection device which relies on steel for the better dissipation capacity and on the superelastic properties of SMA to provide structural recentring.

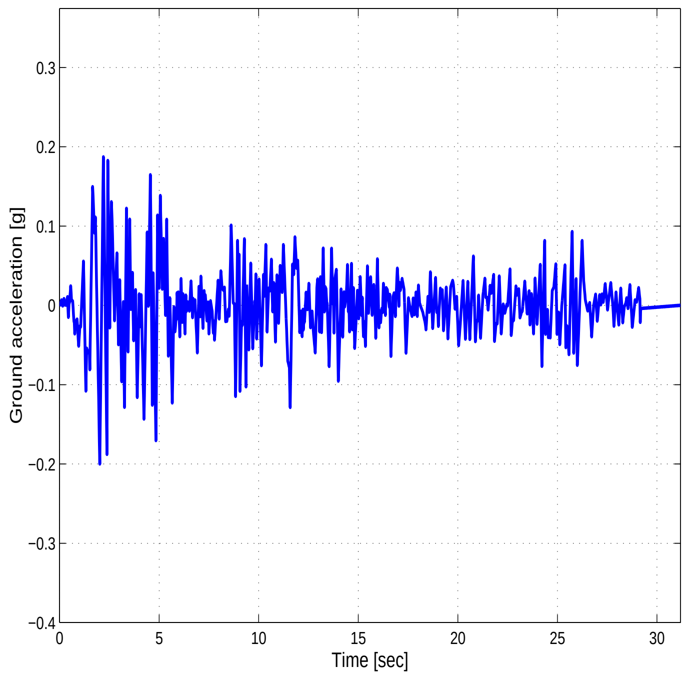

Figure 5.35: Acceleration time-history of the El Centro ground motion scaled to a value of peak ground acceleration of 0.2g.

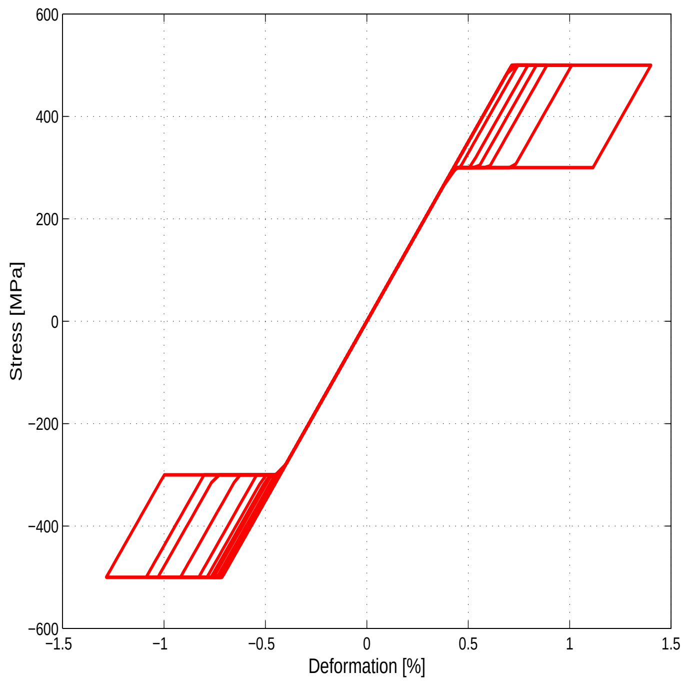

Figure 5.36: SDOF system under El Centro ground motion: stress-strain relationship exhibited by SMA 300-500 alloys for a value of peak ground acceleration of 0.35g.

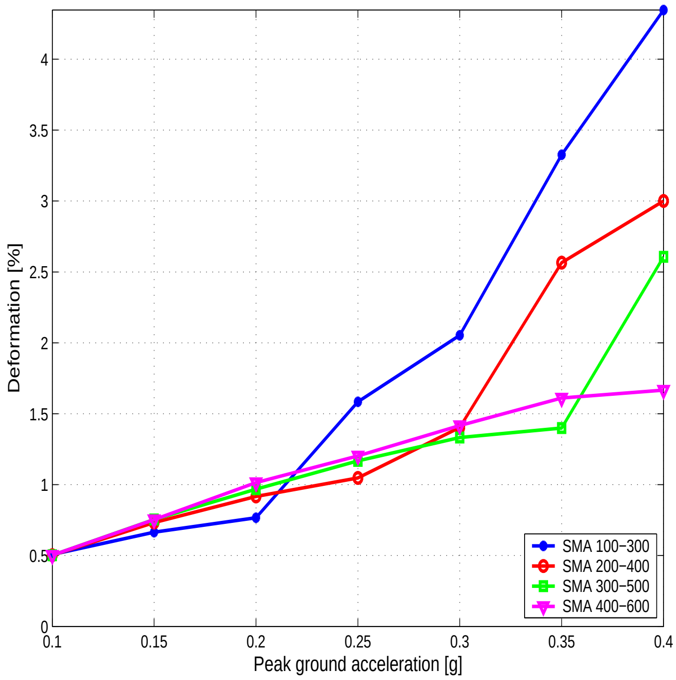

Figure 5.37: SDOF system under El Centro ground motion: maximum deformation versus peak ground acceleration.

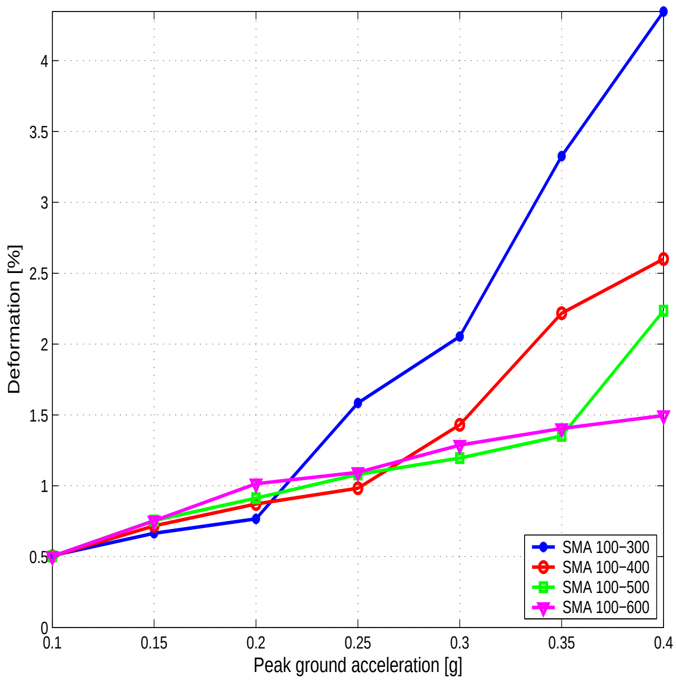

Figure 5.38: SDOF system under El Centro ground motion: maximum deformation versus peak ground acceleration.

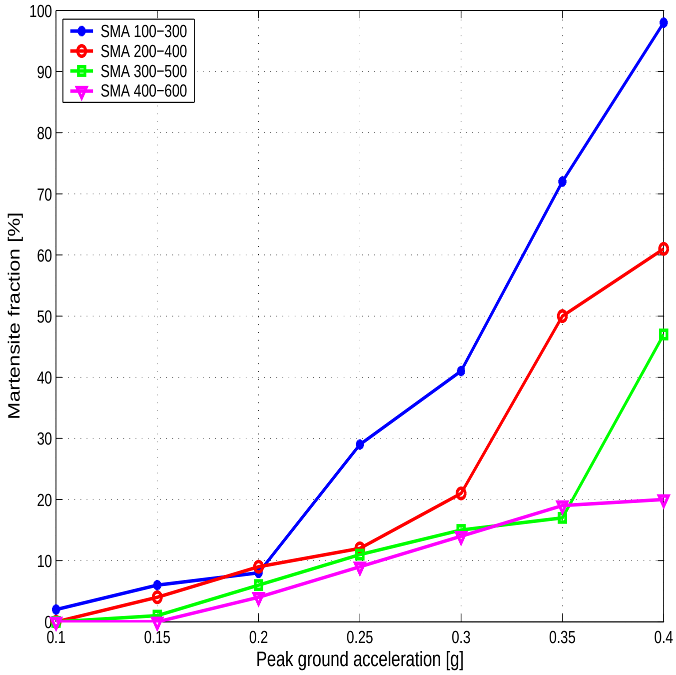

Figure 5.39: SDOF system under El Centro ground motion: maximum martensite fraction versus peak ground acceleration for SMAs with increasing dissipation capacity.

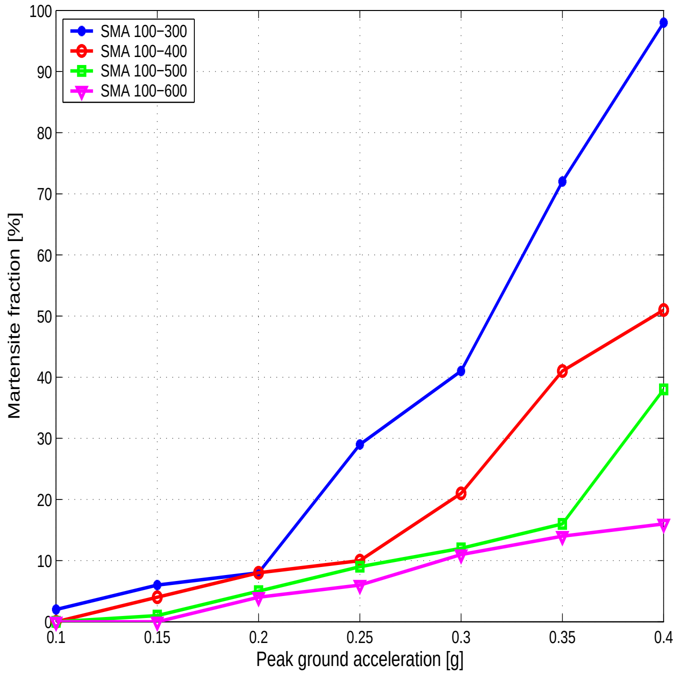

Figure 5.40: SDOF system under El Centro ground motion: maximum martensite fraction versus peak ground acceleration for SMAs with increasing dissipation capacity.

5.8 Final remarks

In this Chapter we have studied the dynamic behavior of pseudoelastic SDOF systems. In particular we have taken into consideration different type of loading conditions, presented in increasing order of complexity. We have focused the attention on two sets of SMAs possessing different dissipation capacity, in order to compare the different ability to attenuate structural vibrations.

In the following we list and briefly review the most important considerations made after analyzing the numerical results:

- The value of damping ratio does not seem to affect the results too much. As a consequence, the material ability to dissipate energy is mainly provided by the hysteresis.
- The plateau length is a very important material parameter, strongly affecting the ductility demand required. The smaller is the value, the faster is the activation of the martensitic behavior.
- The presence of a martensitic phase after completition of the phase transformation provides additional stiffness then guaranteeing good displacement control in case of unexpected strong earthquakes.
- The stress transformation levels are responsible for the energy dissiaption capacity. The longer is the distance between the upper and the lower plateau, the higher is the ability of the system to attenuate the dynamic response. In particular, for low amplitude excitation levels, SMAs with constant or increasing dissipation capacity behave similarly while for higher and higher load values the latter ones better attenuate the oscillations than the former ones.
- The upper plateau stress level plays a key role in the structural response. The higher is its value, the more difficult is the activation of the martensitic phase. Also for the same level of forward trasnformation, SMAs with constant or increasing dissipation capacity behave similarly.
- Superelastic SMAs can successfully be used as recentring mechanisms for seismic applications because of their intrinsic capacity to undergo large deformations without showing any residual. Also, their ability to generate hysteresis loops makes them good candidates as dissipating materials.
- The possibility of choosing among a variety of alloys with different strength characteristics, allows to realize specific SMA-based devices according to the specific structural needs. Consequently, mechanical properties such as transformation stress levels or the plateau length may be cosidered as design variables.

Appendix A

Basic Concepts of Linear Dynamic Analysis

A.1 Introduction

In this chapter we recall some basic concepts of linear structural dynamics. After a brief description of the components of the single-degree-of-freedom system (SDOF), we formulate the corresponding equation of motion, providing also some comments on the influence of the support excitation. Finally, before the analysis of free-vibrations, we analitycally solve the problem of the simple oscillator undergoing sinusoidal signals.

A.2 Components of the basic dynamic system

The essential physical properties of any linearly elastic structural or mechanical system subjected to an external source of excitation or dynamic loading are its mass, elastic properties (flexibility or stiffness), and energy-loss mechanism or damping.
In the simplest model of a SDOF system, each of these properties are assumed to be concentrated in a single physical element (see Figure A.1).
The entire mass m of this system is included in the rigid block constrained by rollers so that it can move only in simple translation. Consequently, the single displacement coordinate $x(t)$ completely defines its position. The elastic resistance to displacement is provided by the weigthness spring of stiffness k, while the energy-loss mechanism is represented by the damper c.
The external dynamic loading producing the response of this system is the time-varying force $p(t)$.

A.3 Equation of motion of the basic dynamic system

The equation of motion for the simple system of Figure A.1a is most easily formulated by directly expressing the equilibrium of all forces acting on the mass by means of the d'Alembert's principle[1].
As shown in Figure A.1b, the forces acting in the direction of the displacement degree of freedom are the applied load *p(t)* and the three resisting forces resulting from the motion: the inertial force $f_I(t)$, the damping force $f_D(t)$, and the spring force $f_S(t)$. The equation of motion is merely an expression of the equilibrium of these quantities as given by:

$$f_I(t) + f_D(t) + f_S(t) = p(t) \tag{A.1}$$

Each of the terms represented on the left hand side of the previous equation is a function of the displacement *x(t)* or one of its time derivatives. The positive sense of these forces has been deliberately chosen to correspond with the negative-displacement sense so that they oppose a positive applied loading.

In accordance with d'Alembert's principle, the inertial force is the product of the mass and the acceleration:

$$f_I(t) = m\,\ddot{x}(t) \tag{A.2}$$

Assuming a viscous damping mechanism, the damping force is the product of the damping constant c and the velocity:

$$f_D(t) = c\,\dot{x}(t) \tag{A.3}$$

Finally, the elastic force is the product of the spring stiffness and the displacement:

$$f_S(t) = k\,x(t) \tag{A.4}$$

When the last three expressions are introduced into relationship (A.1), the equation of motion for this SDOF system is found to be:

$$m\,\ddot{x}(t) + c\,\dot{x}(t) + k\,x(t) = p(t) \tag{A.5}$$

It would be possible to proof that an alternative formulation procedure of the equation of motion could be carried out by means of the *virtual work approach.*

[1]The concept that a mass develops an inertial force proportional to its acceleration and opposing it is known as *d'Alambert's principle.*

A.4 Influence of support excitation

Dynamic stresses and deflections can be induced in a structure not only by a time-varying applied load, but also by motion of its support points.
Important examples of such excitation are the shaking of a building foundation caused by an earthquake or movements of the base support of a piece of equipment due to vibrations of the building in which it is housed.
Let us suppose now that the horizontal movement $x_g(t)$ of the SDOF system's base relative to the fixed reference axis, be generated by an earthquake. Then the equilibrium of forces for the system is written as:

$$f_I(t) + f_D(t) + f_S(t) = 0 \tag{A.6}$$

In this case the inertial force is given by:

$$f_I(t) = m\,\ddot{x}^t(t) \tag{A.7}$$

where $x^t(t)$ represents the total displacement of the mass from the fixed reference axis. After substituting the inertial, damping, and elastic forces in equation (A.6), it is possible to write:

$$m\,\ddot{x}^t(t) + c\,\dot{x}(t) + k\,x(t) = 0 \tag{A.8}$$

Before this equation can be solved, all forces must be expressed in terms of a single variable, which can be accomplished by noting that the total motion of the mass can be expressed as the sum of the ground motion and that due to the spring deformation:

$$x^t(t) = x(t) + x_g(t) \tag{A.9}$$

Expressing the inertial force in terms of the two acceleration components obtained by double differentation of the previous equation and substituting the result into equation (5.8) yields

$$m\,\ddot{x}(t) + m\,\ddot{x}_g(t) + c\,\dot{x}(t) + k\,x(t) = 0 \tag{A.10}$$

or, since the gound acceleration represents the specific dynamic input to the structure, the same expression can more conveniently be written:

$$m\,\ddot{x}(t) + c\,\dot{x}(t) + k\,x(t) = -m\,\ddot{x}_g(t) \equiv p_{eff}(t) \tag{A.11}$$

In this equation, $p_{eff}(t)$ denotes the effective support excitation loading. In other words, the structural deformations caused by ground acceleration $\ddot{x}_g(t)$ are exactly the same as those which would be produced by an external load $p(t)$ of intensity equal to $-m\,\ddot{x}_g(t)$. The negative sign in this effective load definition indicates that the effective force opposes the sense of the ground acceleration.

A.5 Response of a SDOF system to harmonic loading: undamped case

Let us assume that the system of Figure A.1 be subjected to a harmonically varying load *p(t)* of sine-wave form having an amplitude p_0 and circular frequency $\bar{\omega}$. In this case the equation of motion of the system is of the form:

$$m\,\ddot{x}(t) + c\,\dot{x}(t) + k\,x(t) = p_0\,sin\,\bar{\omega}t \tag{A.12}$$

Before considering the viscously damped case, it is useful to examine the behavior of an undamped system, which is controlled by:

$$m\,\ddot{x}(t) + k\,x(t) = p_0\,sin\,\bar{\omega}t \tag{A.13}$$

The corresponding *complementary solution* (i.e. solution of the homogeneous differential equation) is the expression:

$$x_c(t) = A\,cos\,\omega t + B\,sin\,\omega t \tag{A.14}$$

where ω is the *natural frequency* of the system[2] and A and B two constants depending on the initial conditions of the equation of motion.
The general solution must also include the *particular solution*, which depends upon the form of the dynamic loading. In this case of harmonic loading, it is reasonable to assume that the corresponding motion is harmonic and in phase with the loading itself. Thus, the particular solution is:

$$x_p(t) = C\,cos\,\bar{\omega}t \tag{A.15}$$

Substituting equation (A.15) into equation (A.13) and dividing through by $sin\,\bar{\omega}t$ (which is nonzero in general) and by k and noting that $k/m = \omega^2$, it is possible to obtain after some rearrangement:

$$C = \frac{p_0}{k}\left[\frac{1}{1-\beta^2}\right] \tag{A.16}$$

in which β is defined as the ratio of the applied loading frequency to the natural frequency of the system:

$$\beta \equiv \frac{\bar{\omega}}{\omega} \tag{A.17}$$

[2]The natural frequency of the system depends on both the mass and the stiffness of the system and is given by the formula $\omega = \sqrt{k/m}$. The *cyclic frequency*, instead, is referred to as the frequency of motion and is given by $f = \omega/2\,\pi$. Its reciprocal $1/f = 2\,\pi/\omega = T$ is the time required to complete one cycle and is called *period* of the motion. Usually for structural and mechanical systems the period T is measured in seconds and the frequency is measured in cycles per second, commonly referred to as Hertz (*Hz*).

The *general solution* of equation (A.13) is now obtained by combining the complementary and the particular solution and also making use of equation (A.16):

$$x(t) = x_c(t) + x_p(t) = [A\,cos\,\omega t + B\,sin\,\omega t] + \frac{p_0}{k}\left[\frac{1}{1-\beta^2}\right]\sin\bar{\omega}t \qquad (A.18)$$

The expression for the velocity is obtained by derivation of the displacement time-history with respect to time:

$$\dot{x}(t) = [-A\omega\,sin\,\omega t + B\omega\,cos\,\omega t] + \frac{p_0}{k}\left[\frac{1}{1-\beta^2}\right]\bar{\omega}\cos\bar{\omega}t \qquad (A.19)$$

while the acceleration is given by double derivation of the displacement time-history with respect to time as well:

$$\ddot{x}(t) = [-A\omega^2\,cos\,\omega t - B\omega^2\,sin\,\omega t] - \frac{p_0}{k}\left[\frac{1}{1-\beta^2}\right]\bar{\omega}^2\sin\bar{\omega}t \qquad (A.20)$$

The values of parameters A and B depend on the conditions with which the response was initiated. In particular, knowing the value of both the displacement and velocity at time zero it is possible to find that:

$$A = x(0) \qquad B = \frac{\dot{x}(0)}{\omega} - \frac{p_0\,\beta}{k}\left[\frac{1}{1-\beta^2}\right] \qquad (A.21)$$

A.6 Response of a SDOF system to harmonic loading: damped case

Returning to the equation of motion including viscous damping[3], equation (A.12), dividing by m, and noting that $c/m = 2\,\xi\omega$ leads to

$$\ddot{x}(t) + 2\,\xi\omega\dot{x}(t) + \omega^2\,x(t) = \frac{p_0}{m}\,sin\,\bar{\omega}t \qquad (A.22)$$

The *complementary solution* of this equation is:

$$x_c(t) = [A\,cos\,\omega_D t + B\,sin\,\omega_D t]\,exp\,(-\xi\omega t) \qquad (A.23)$$

while the *particular solution* is of the form:

$$x_p(t) = C\,cos\,\bar{\omega}t + D\,sin\,\bar{\omega}t \qquad (A.24)$$

in which the cosine term is required as well as the sine term because, in general, the response of a damped system is not in phase with the loading.

[3]It is convenient in this case to express damping in terms of a *damping ratio* ξ which is the ratio of the given damping to the critical value: $\xi = c/c_c = c/2\,m\,\omega$

In equation (A.23), the term ω_D represents the *damped natural frequency* of the system. It is correlated with the natural frequency through the relation:

$$\omega_D \equiv \omega \sqrt{1-\xi^2} \tag{A.25}$$

Substituting equation (A.24) into equation (A.22), separating the multiples of $\cos \bar{\omega} t$ from the multiples of $\sin \bar{\omega} t$ and rearranging the expression, it is possible to find the analytical expressions for C and D:

$$C = \frac{p_0}{k}\left[\frac{-2\,\xi\beta}{(1-\beta^2)^2+(2\xi\beta)^2}\right] \tag{A.26}$$

$$D = \frac{p_0}{k}\left[\frac{1-\beta^2}{(1-\beta^2)^2+(2\xi\beta)^2}\right] \tag{A.27}$$

Introducing the last two relationships into equation (A.24) and combining the result with the complementary solution, the *total response* is then obtained:

$$\begin{aligned} x(t) &= [A\,cos\,\omega_D t + B\,sin\,\omega_D t]\,exp\,(-\xi\omega t) \\ &+ \frac{p_0}{k}\left[\frac{1}{(1-\beta^2)^2+(2\xi\beta)^2}\right]\left[(1-\beta^2) sin\bar{\omega}t - 2\xi\beta\,cos\,\bar{\omega}t\right] \end{aligned} \tag{A.28}$$

The first therm on the right hand side of this equation represents the *transient response*, which damps out in accordance with $exp(-\xi\omega t)$, while the second term represents the *steady-state harmonic response*, which will continue indefenitively. The constants A and B, again, can be evaluated for any given initial condition, $x(0)$ and $\dot{x}(0)$. The term β, as in the undamped case, is defined as the ratio of the applied loading frequency to the natural free-vibration frequency of the system.

The velocity is given by the first derivative of *x(t)* with respect to time:

$$\begin{aligned} \dot{x}(t) &= [cos\,\omega_D t\,(\omega_D B - \xi\omega A) + sin\,\omega_D t\,(\omega_D B - \xi\omega A)]\,exp\,(-\xi\omega t) \\ &+ \frac{p_0}{k}\left[\frac{1}{(1-\beta^2)^2+(2\xi\beta)^2}\right]\left[(1-\beta^2)\bar{\omega}\,cos\,\bar{\omega}t - 2\xi\beta\bar{\omega}\,sin\,\bar{\omega}t\right] \end{aligned} \tag{A.29}$$

The acceleration, instead, is given by the second derivative of *x(t)* with respect to time:

$$\begin{aligned} \ddot{x}(t) &= [cos\,\omega_D t\,(-\omega_D^2 A - 2\xi\omega\omega_D B + \xi^2\omega^2 A) \\ &+ sin\,\omega_D t\,(-\omega_D^2 B - 2\xi\omega\omega_D A + \xi^2\omega^2 B)]\,exp\,(-\xi\omega t) \\ &+ \frac{p_0}{k}\left[\frac{1}{(1-\beta^2)^2+(2\xi\beta)^2}\right]\left[(\beta^2-1)\bar{\omega}^2\,sin\,\bar{\omega}t + 2\xi\beta\bar{\omega}^2\,cos\,\bar{\omega}t\right] \end{aligned} \tag{A.30}$$

The constants A and B, again, depend on the conditions with wich the response was initiated. They assume the following form:

$$A = x(0) + (2\xi\beta)\,\frac{p_0}{k}\left[\frac{1}{(1-\beta^2)^2 + (2\xi\beta)^2}\right] \tag{A.31}$$

$$B = \frac{\dot{x}(0)}{\omega_D} + \frac{(\xi\omega A)}{\omega_D} - \frac{p_0}{\omega_D\,k}\left[\frac{\bar{\omega}}{(1-\beta^2)^2 + (2\xi\beta)^2}\right] \tag{A.32}$$

A.7 Analysis of free vibrations

It has been shown in the preceeding section that the equation of motion of a simple spring-mass system without damping can be expressed as:

$$m\,\ddot{x}(t) + k\,x(t) = p(t) \tag{A.33}$$

in which *x(t)* represents the displacement from the static equilibrium position and *p(t)* represents the effective load acting on the system, either applied directly or resulting from support motions.
Motions taking place when there are no acting force are called *free vibrations*. Mathematically it is possible compute the free-vibration response by solving the homogeneous form (i.e. by setting the right-hand term equal to zero) of the previous equation:

$$m\,\ddot{x}(t) + k\,x(t) = 0 \tag{A.34}$$

In this particular case, the displacement response corresponds to the complementary solution of equation A.12, while the velocity and acceleration time histories still correspond to its first and second derivative computed with respect to time. All quantities are respectively given by the following relationships:

$$x(t) = A\,cos\,\omega t + B\,sin\,\omega t \tag{A.35}$$

$$\dot{x}(t) = [-A\omega\,sin\,\omega t + B\omega\,cos\,\omega t] \tag{A.36}$$

$$\ddot{x}(t) = [-A\omega^2\,cos\,\omega t - B\omega^2\,sin\,\omega t] \tag{A.37}$$

being A and B, again, two constants depending upon the initial conditions (i.e. the displacement and velocity values at time $t = 0$, when the free-vibration was set in motion) and whose expressions are:

$$A = x(0) \qquad B = \frac{\dot{x}(0)}{\omega} \tag{A.38}$$

Similarly, the response quantities of damped free-vibration problems is given by starting from equations (A.29), (A.30) and (A.31) respectively:

$$
\begin{aligned}
x(t) &= [A\,cos\,\omega_D t + B\,sin\,\omega_D t]\,exp\,(-\xi\omega t) && \text{(A.39)}\\
\dot{x}(t) &= [cos\,\omega_D t\,(\omega_D B - \xi\omega A) + sin\,\omega_D t\,(\omega_D B - \xi\omega A)] \\
&\quad \cdot exp\,(-\xi\omega t) && \text{(A.40)}\\
\ddot{x}(t) &= [cos\,\omega_D t\,(-\omega_D^2 A - 2\xi\omega\omega_D B + \xi^2\omega^2 A) \\
&+ \; sin\,\omega_D t\,(-\omega_D^2 B - 2\xi\omega\omega_D A + \xi^2\omega^2 B)]\,exp\,(-\xi\omega t) && \text{(A.41)}
\end{aligned}
$$

where the new values for A and B assume the form:

$$A = x(0) \qquad\qquad B = \frac{\dot{x}(0)}{\omega_D} + \frac{(\xi\omega A)}{\omega_D} \tag{A.42}$$

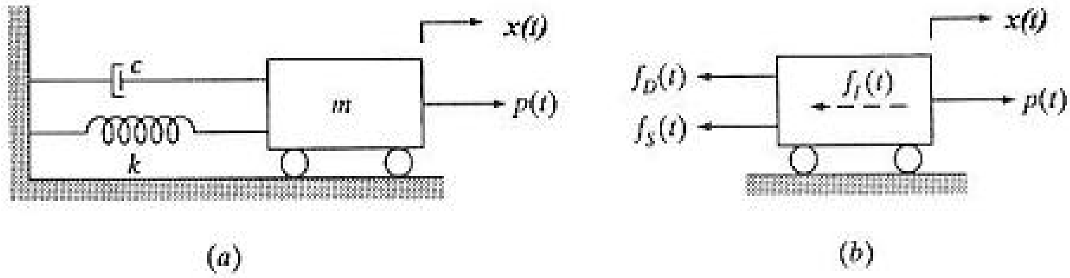

Figure A.1: Single-degree-of-freedom system: (a) basic components and (b) free-body diagram.

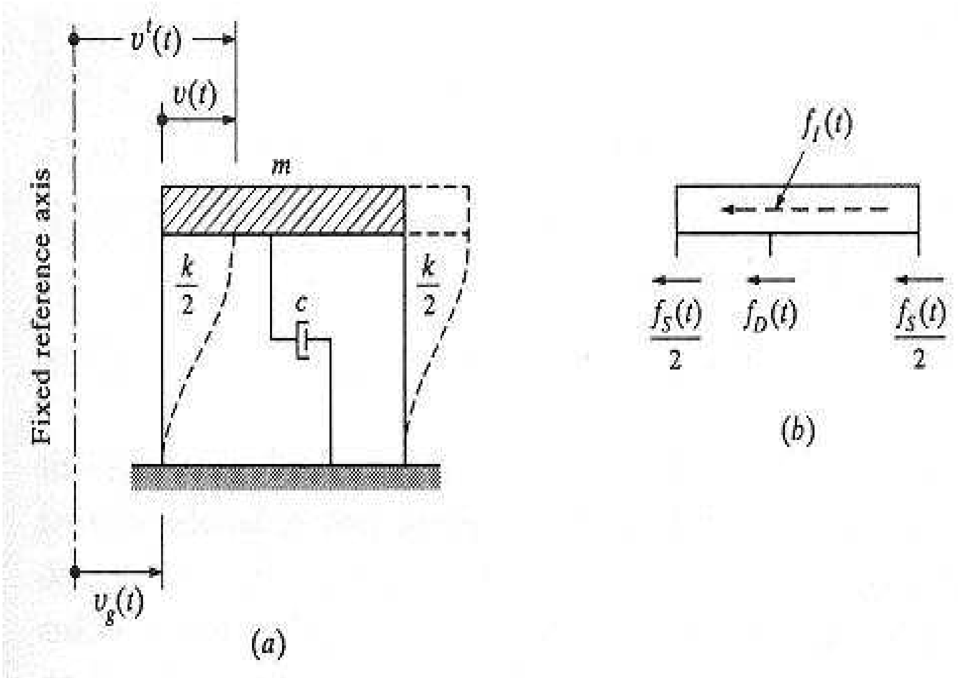

Figure A.2: Influence of support excitation on SDOF equilibrium: (a) motion of system and (b) equilibrium forces.

Appendix B

Basic Concepts of Nonlinear Dynamic Analysis

B.1 Introduction

In this section we focus the attention on the numerical solution of the nonlinear equation of motion. We adopt the well known Newmark method, solving the implicit problem by means of the incremental-iterative approach based on the Newton-Raphson strategy. After a brief introduction concerning the use of numerical tecniques, we give emphasis on the description of the algorithms in view of their implementation in a computer code.

B.2 General comments on numerical approximation procedures

Before the details of the numerical procedure adopted to solve the nonlinear equation of motion, it could be useful to summarize a few basic facts about the numerical approximation provided by step-by-step methods.

- The methods can be classified as either *explicit* or *implicit*. An explicit method is defined as one in which the new response values calculated in each step depend only on quantities obtained in the preceeding step, so that the analysis proceeds directly from one step to the next. In an implicit method, on the other hand, the expressions giving the new values for a given step include one or more values pertaining to that same step, so that trial values of the necesary quantities must be assumed and then these are refined by successive iterations.
- The primary factor to be considered in selecting a step-by-step method is *efficiency*, which concerns the computational effort required to achieve the desired level of *accuracy* over the range of time for which the response

is needed. Accuracy alone cannot be a criterion for method selection because, in general, any desired degree of accuracy can be obtained by any method if the time step is made short enough (but with obvious corresponding increases of costs). In any case, the time steps must be short enough to provide adequate definition of the loading and the response history.

- Factors that may contribute to errors in the results obtained from well-defined loading include:
  - *Roundoff*, resulting from calculations being done using numbers expressed by too few digits.
  - *Instability*, caused by amplification of the errors from one step during the calculations in subsequent steps. Stability of any method is improved by reducing the length of the time step.
  - *Truncation*, using too few terms in series expressions of quantities.
- Errors resulting from any causes may be manifested by either or both of the following effects:
  - *Phase shift* or apparent change of frequency in cyclic results.
  - *Artificial damping*, in which the numerical procedure removes or adds energy to the dynamically responding system.

All of the above mentioned topics would be worth of further discussion which is not the main task of this work. Anyway, a vast body of literature dealing with a large number of both theoretical and practical applications has been written on these subjects. For additional information the reader, for example, may consult references [10] and [28].

B.3 The Newton-Raphson strategy

First, it is needed to start from the nonlinear expression of the equation of motion, where it is highlighted that the internal forces are dependent on the displacement which is the unknown of the problem itself:

$$m\ddot{x} + c\dot{x} + f_s(x) = p(t) \tag{B.1}$$

Since we use a Newton-Raphson approach to solve by ierations the nonlinear problem, it is convenient to rewrite the previous expression in the so-called *residual form*:

$$R(x) = p(t) - m\ddot{x} - c\dot{x} - f_s(x) = 0 \tag{B.2}$$

The main idea to solve the problem is that, given the solution at time step n:

$$R(x_n) = p_n - m\ddot{x}_n - c\dot{x}_n - f_s(x_n) = 0 \tag{B.3}$$

the goal is to find the solution at time step *n+1*:

$$R(x_{n+1}) = p_{n+1} - m\ddot{x}_{n+1} - c\dot{x}_{n+1} - f_s(x_{n+1}) = 0 \tag{B.4}$$

by means of an iterative procedure.
To do so, it is assumed that, for the time step *n+1*, an estimate of the solution x_{n+1}^k is known and an improved estimate x_{n+1}^{k+1} is sought.
To formalize mathematically these concepts, the Newton-Raphson algorithm is based on a Taylor series expansion of the residual function, in terms of the displacement value about x_{n+1}^k:

$$R(x_{n+1}^{k+1}) = R(x_{n+1}^k) + \frac{\partial R}{\partial x}_{|x_{n+1}^k}\left(x_{n+1}^{k+1} - x_{n+1}^k\right) + \frac{1}{2}\frac{\partial^2 R}{\partial x^2}_{|x_{n+1}^k}\left(x_{n+1}^{k+1} - x_{n+1}^k\right) + ... \tag{B.5}$$

For x_{n+1}^k close to the solution, the change in x is small and second order terms may be neglected:

$$R(x_{n+1}^{k+1}) = R(x_{n+1}^k) + \frac{\partial R}{\partial x}_{|x_{n+1}^k}\Delta x + O\left(\|x\|^2\right) \tag{B.6}$$

Within second-order accuracy, the change in x needed to give a zero residual is given by the linearized equation:

$$R(x_{n+1}^{k+1}) = R(x_{n+1}^k) + \frac{\partial R}{\partial x}_{|x_{n+1}^k}\Delta x \approx 0 \tag{B.7}$$

As we can see, in order to evaluate the residual in the *k+1* iteration, we need to compute the residual and the derivative of the residual with respect to x (i.e. *consistent tangent*) in the previous trial solution.
As a consequence the following expression yields:

$$R(x_{n+1}^k) = p_{n+1} - m\ddot{x}_{n+1}^k - c\dot{x}_{n+1}^k - f_s(x_{n+1}^k) \tag{B.8}$$

and also

$$\frac{\partial R}{\partial x}_{|x_{n+1}^k} = -m\frac{\partial \ddot{x}}{\partial x}_{|x_{n+1}^k} - c\frac{\partial \dot{x}}{\partial x}_{|x_{n+1}^k} - \underbrace{\frac{\partial f_s(x)}{\partial x}_{|x_{n+1}^k}}_{k_t(x_{n+1}^k)} \tag{B.9}$$

B.4 Newmark solution of the nonlinear equation of motion

In this section we illustrate the solution of the equation of motion by a time marching process using the classical Newmark method of solution.

The initial value problem for equation (B.1) consists of finding a displacement *x=x(t)* satisfying both equation (B.1) and the given initial data:

$$x(0) = d_0 \qquad \dot{x}(0) = v_0 \tag{B.10}$$

where d_0 and v_0 are the initial displacement and velocity values (i.e. vectors when dealing with multi-degree-of-freedom systems).
The intial state is completed by solving the residual equation at time zero. Accordingly:

$$R = p(0) - m\ddot{x}(0) - c\dot{x}(0) - f_s(x(0)) = 0 \tag{B.11}$$

which yields the solution:

$$\ddot{x}(0) = m^{-1}[c\dot{x}(0) + f_s(u(0)) - p(0)] = a_0 \tag{B.12}$$

which, combined with the initial conditions (B.1), gives a complete state at time zero. The Newmark formulas to advance a solution are given by:

$$x_{n+1} = x_n + \Delta t\dot{x_n} + \frac{1}{2}\Delta t^2 \left[(1-2\beta)\ddot{x}_n + 2\beta\ddot{x}_{n+1}\right] \tag{B.13}$$

$$\dot{x}_{n+1} = \dot{x}_n + \Delta t \left[(1-\gamma)\ddot{x}_n + \gamma\ddot{x}_{n+1}\right] \tag{B.14}$$

where x_n, $\dot{x}_n$ and $\ddot{x}_n$ are the approximation of $x(t_n)$, $\dot{x}(t_n)$ and $\ddot{x}(t_n)$ respectively. Equations (B.13) and (B.14) represent finite difference formulas describing the evolution of the approximate solution.
Parameters β and γ determine the *stability* and the *accuracy* characteristics of the algorithm under consideration.
The Newmark family contains as special cases many well-known and widely used numerical methods (see Table A.1 for a summary of the main methods).
Among several possible implementations ([28]), we consider the *predictor corrector form*, a very often used tecnique to solve nonlinear structural dynamic problems. First we define *predictors*:

$$\tilde{x}_{n+1} = x_n + \dot{x}_n\Delta t + \frac{1}{2}(1-2\beta)\ddot{x}_n\Delta t^2 \tag{B.15}$$

$$\tilde{\dot{x}}_{n+1} = \dot{x}_n + (1-\gamma)\ddot{x}_n\Delta t \tag{B.16}$$

and then we compute *correctors*

$$x_{n+1} = \tilde{x}_n + \beta\Delta t^2\ddot{x}_{n+1} \tag{B.17}$$

$$\dot{x}_{n+1} = \tilde{\dot{x}}_n + \gamma\Delta t\ddot{x}_{n+1} \tag{B.18}$$

The predictions of velocity and displacement are known at the beginning of each time step, but iterations are required to determine the proper value of displacement and hence acceleration and velocity:

$$
\begin{aligned}
x_{n+1}^k &= \tilde{x}_n + \beta\Delta t^2 \ddot{x}_{n+1}^k && \text{(B.19)}\\
\dot{x}_{n+1}^k &= \tilde{\dot{x}}_n + \gamma\Delta t \ddot{x}_{n+1}^k && \text{(B.20)}
\end{aligned}
$$

Solving for acceleration and substituting for velocity gives:

$$
\begin{aligned}
\ddot{x}_{n+1}^k &= \frac{1}{\beta\Delta t^2}\left(x_{n+1}^k - \tilde{x}_n\right) && \text{(B.21)}\\
\dot{x}_{n+1}^k &= \tilde{\dot{x}}_n + \gamma\Delta t \ddot{x}_{n+1}^k && \text{(B.22)}
\end{aligned}
$$

It is now possible to perform the gradient computation:

$$
\begin{aligned}
\frac{\partial \ddot{x}}{\partial x}_{|x_{n+1}^k} &= \frac{1}{\beta\Delta t^2} && \text{(B.23)}\\
\frac{\partial \dot{x}}{\partial x}_{|x_{n+1}^k} &= \gamma\Delta t\, \frac{\partial \ddot{x}}{\partial x}_{|x_{n+1}^k} = \frac{\gamma}{\beta\Delta t} && \text{(B.24)}
\end{aligned}
$$

According to equation (B.9), the expression of the residual assumes the form:

$$
-\frac{\partial R}{\partial x}_{|x_{n+1}^k} = \frac{1}{\beta\Delta t^2}\, m + \frac{\gamma}{\beta\Delta t}\, c + k_t(x_{n+1}^k) = k_d \tag{B.25}
$$

which, upon substitution into equation (B.8), allows to compute the displacement increment between iteration *k* and iteration *k+1*:

$$
k_d \Delta x = R(x_{n+1}^k) \tag{B.26}
$$

Obvsiouly, in view of the implementation of the above algorithm, we remind that Newton-Raphson iterations are required until the residual is less than a tolerance. A summary of the steps to be perfermed are given in Table B.2.

B.5 Algorithmic considerations on the Newmark integration method

As already stated above, the parameters β and γ determine the stability and accuracy characteristics of the method under consideration.
In particular, an algorithm for which *stability* imposes a time step restriction is called *conditionally stable*, while an algorithm for which there is no time step restriction imposed by stability is called *unconditionally stable*.
From a mathematical point of view these features can be expressed in the following form:

$$
2\beta \geq \gamma \geq \frac{1}{2} \tag{B.27}
$$

for the method to be unconditionally stable, while the method is conditionally stable if:

$$\gamma \geq \frac{1}{2} \qquad \text{and} \qquad \beta < \frac{\gamma}{2} \tag{B.28}$$

In the last case, it is possible to define the *critical sampling frequency* that gives the critical time step below which the algorithm is stable:

$$\omega \Delta t \leq \Omega_{crit} \tag{B.29}$$

where

$$\Omega_{crit} = \frac{\xi(\gamma - \frac{1}{2}) + \left[\gamma/2 - \beta + \xi^2(\gamma - \frac{1}{2})^2\right]^{1/2}}{(\gamma/2 - \beta)} \tag{B.30}$$

From equation (B.29) it follows that:

$$\frac{\Delta t}{T} \leq \frac{\Omega_{crit}}{2\pi} \tag{B.31}$$

being T the period of vibration of the SDOF system.
When dealing with multi-degree-of-freedom systems, the value of ω to be used in equation (B.29) is the maximum natural frequency of the system which, trivially, corresponds to the minimum structural period of vibration.

The terms *accuracy*, instead, introduces the concept of *order of accuracy* or *rate of convergence*. It is strictly connected with the *consistency* of an algorithm and it comes from the spectral analysis of the algorithm[1] itself ([28]).
It would be possible to show that, once stability and consistency are verified, *convergence*, which is the primary requirement that an algorithm should possess, is automatically achieved ([28]).

Finally, it is worth recalling some considerations concerning the possible numerical dissipation produced by the algorithm. As long as the method is stable, $\gamma = \frac{1}{2}$ implies no numerical dissipation for physically undamped Newmark methods, whereas for $\gamma \geq \frac{1}{2}$ numerical dissipation is introuced reducing accuracy to first order. When parameters β and γ assume values 0.3025 and 0.6 respectively, the method is said to be damped.

[1]There are several techniques that can be employed to study the characteristics of an algorithm. One of the most used is the *modal approach*, sometimes called spectral or Fourier analysis, which enables to decompose the whole problem into uncoupled scalar equations.

Name	**Type**	$\boldsymbol{\beta}$	$\boldsymbol{\gamma}$	**Stability condition**	**Order of accuracy**
Average acceleration	Implicit	1/4	1/2	Unconditional	2
Linear acceleration	Implicit	1/6	1/2	$\Omega_{crit} \approx 3.464$	2
Fox-Goodwin	Implicit	1/12	1/2	$\Omega_{crit} \approx 2.449$	2
Central difference	Explicit	0	1/2	$\Omega_{crit} = 2$	2

Table B.1: Properties of selected members of the Newmark family of methods.

1. Newton-Raphson iteration counter

$$k = 0$$

2. Predictor phase

$$\begin{aligned} x_{n+1}^{(k)} &= \tilde{x}_{n+1} \\ \dot{x}_{n+1}^{(k)} &= \tilde{\dot{x}}_{n+1} \\ \ddot{x}_{n+1}^{(k)} &= 0 \end{aligned}$$

3. Evaluate residual, effective stiffness and solution increment

$$\begin{aligned} R &= p_{n+1} - m\,\ddot{x}_{n+1}^{(k)} - c\,\dot{x}_{n+1}^{(k)} - f(x_{n+1}^{(k)}) \\ k_d &= \frac{1}{\beta \Delta t^2}\,m + \frac{\gamma}{\beta \Delta t}\,c + k_t(x_{n+1}^{(k)}) \\ \Delta x &= \frac{R}{k_d} \end{aligned}$$

4. Corrector phase

$$\begin{aligned} x_{n+1}^{(k+1)} &= x_{n+1}^{(k)} + \Delta x \\ \ddot{x}_{n+1}^{(k+1)} &= \frac{1}{\beta \Delta t^2}\,(x_{n+1}^{(k+1)} - \tilde{x}_{n+1}) \\ \dot{x}_{n+1}^{(k+1)} &= \tilde{\dot{x}}_{n+1} + \gamma \Delta t \ddot{x}_{n+1}^{(k+1)} \end{aligned}$$

5. Check convergence

If $R >$ *tolerance* then $k \longleftarrow k+1$, go to (3)

If $R \leq$ *tolerance* then go to (6)

6. Update solution

$$\begin{aligned} x_{n+1} &= x_{n+1}^{(k+1)} \\ \dot{x}_{n+1} &= \dot{x}_{n+1}^{(k+1)} \\ \ddot{x}_{n+1} &= \ddot{x}_{n+1}^{(k+1)} \end{aligned}$$

7. Advance to next load step

$n \longleftarrow n+1, \quad$ go to (1)

Table B.2: The Newmark predictor-corrector implicit algorithm.

Appendix C

Basic Concepts of Earthquake Enigineering

C.1 Introduction

In this section we review some basic topics of earthquake engineering. Without the claim of being exhaustive, we briefly discuss the main concepts needed for the construction of elastic and inelastic response spectra, addressing the reader to the textbooks [10] and [11] for further details. We also present some applications.

C.2 Elastic response spectra

The most common way to describe a seismic event is given by its acceleration response spectrum, which condenses information about amplitude and frequency content of the ground motion. On the other hand, any information about duration or number of cycles is not represented. The *response spectrum* is defined as the maximum response of a SDOF system with damping to dynamic motion or forces. It therefore depends on the characteristics of the system and on the nature of the ground motion. If a linear response and a constant viscous damping are assumed, the response spectrum becomes a function of the dynamic input and of the period of vibration of the system (i.e. it depends only on the dynamic input amplitude and frequency content).

The quantities commonly studied in terms of response spectra are displacements, velocities and accelerations, which can be expressed by absolute values (taken with respect to the ground before the earthquake) or relative values (taken with respect to the ground during the earthquake). In seismic design absolute accelerations, and relative displacements and velocities are of interest and, as a consequence, a variety of response spectra can be defined.

Let us, for instance, consider the following peak responses:

$$u_0(T,\xi) = \max|u(t,T,\xi)| \tag{C.1}$$
$$\dot{u}_0(T,\xi) = \max|\dot{u}(t,T,\xi)| \tag{C.2}$$
$$\ddot{u}_0(T,\xi) = \max|\ddot{u}(t,T,\xi)| \tag{C.3}$$

The *displacement response spectrum* is a plot of u_0 against T (period of vibration) for a fixed value of ξ (damping ratio). A similar plot for $\dot{u}_0$ is the *relative velocity response spectrum* and for $\ddot{u}_0$ is the *acceleration response spectrum*.
Instead of true velocity and acceleration, however, slightly different values are commonly used in practice applications. These new quantities are named as *pseudo-velocity* (PSV) and *pseudo-acceleration* (PSA) and they are strictly correlated with the concept of displacement response spectrum. Their mathematical expressions are the following:

$$D = u_0 \tag{C.4}$$
$$PSV = \left(\frac{2\pi}{T}\right) D \tag{C.5}$$
$$PSA = \left(\frac{2\pi}{T}\right)^2 D \tag{C.6}$$

The previous formulas, evaluated for a period range of engineering interest as well as for different values of damping ratio, enable to graphically represent the response spectra, either in three different graphs, or in the common tripartite plot, which provides the interelations of all three quantities.
Finally, it is also useful to remind the definition of *elastic seismic coefficient*:

$$C_{se} = \frac{PSA}{g} W = m \left(\frac{2\pi}{T}\right)^2 D \tag{C.7}$$

being W the weight of the SDOF system.

C.3 Inelastic response spectra

If the system responds to a dynamic excitation with nonlinear behavior, the initial period of vibration and the elastic equivalent viscous damping of the system are not sufficient to obtain the maximum response, which will depend on the actual shape of the force-displacement curve of the system. To reduce the problem to manageable proportions, it is common in practice to assume a linear elastic-perfectly-plastic response, as being equivalent to the actual response of the system. The significant parameters of the system will then be the initial stiffness (k), the mass (m), the yield strength (f_y) and the displacement capacity Δ_y. Mass and stiffness can also be condensed in a single parameter which is the initial period of vibration (T).

The response spectra quantities can also be determined for elasto-plastic systems as well, with the property of consitency with the analogous ones related to the linear case:

$$D_y = u_y \tag{C.8}$$

$$PSV_y = \frac{2\pi}{T} D_y \tag{C.9}$$

$$PSA_y = \left(\frac{2\pi}{T}\right)^2 D_y \tag{C.10}$$

being D_y the *yield deformation*, PSV_y the *pseudo-velocity* and PSA_y the *pseudo-acceleration*.

To understand the properties of inelastic spectra, we have anyway to introduce four new quantities, which are of foundamental importance also in view of practical applications. They are the normalized yield strength, the yield strength reduction factor, the inelastic seismic coefficient and the ductility factor.

The *normalized yield strength* $\overline{f}_y$ of an elasto-plastic system is defined as:

$$\overline{f}_y = \frac{f_y}{f_0} = \frac{u_y}{u_0} \tag{C.11}$$

where f_0 and u_0 are the peak values of the earthquake induced resisting force and deformation, respectively, in the corresponding linear system[1]. We may interprete f_0 as the minimum strength required for the structure to remain linearly elastic during the ground motion. If the normalized yield strength of a system is less than unity, the system will yield and deform into the inelastic range while, for a system that remains elastic, it will be equal to one because such a system can be interpreted as an elasto-plastic system with $f_y = f_0$.
Alternatively, we can relate f_y to f_0 through a *yield strength reduction factor* R_y defined by:

$$R_y = \frac{f_0}{f_y} = \frac{u_0}{u_y} \tag{C.12}$$

Obviously, as we can observe, R_y is the reciprocal of $\overline{f}_y$. In particular it is equal to one for linearly elastic systems and greater than one for system deforming into the inelastic range.
Similarly to equation C.7, we define for elasto-plastic system the *inelastic*

[1]The *corresponding linear system* is a system with the same mass, damping and stiffness of the elasto-plastic one. For this reason the period of vibration of the corresponding linear system is the same as the period of the elasto-plastic one undergoing small oscillations ($u \leq u_y$). Anyway, at larger amplitudes of motion, the natural period of vibration is not defined for inelastic systems.

seismic coefficient, which correlates the elastic seismic coefficient and the yield strength reduction factor:

$$C_s = \frac{C_{se}}{R_y} \tag{C.13}$$

We may observe that when the yield strength reduction factor is equal to unity, there is no difference between elastic and inelastic seismic coefficient.
Finally, we introduce the concept of *ductility factor*, which is given by the following ratio:

$$\mu = \frac{u_m}{u_y} \tag{C.14}$$

being u_m the peak, or absolute (without considering the algebraic sign) maximum, deformation of the elasto-plastic system due to the ground motion and u_y the displacement at which the system starts yielding.
The ductility factor is greater than unity for systems which experience inelastic deformations.
From equations C.7, C.8 and C.9 we can also express the relationships correlating the three introduced quantities:

$$\frac{u_m}{u_0} = \mu \, \overline{f}_y = \frac{\mu}{R_y} \tag{C.15}$$

We also remind that an interpolative procedure is necessary to obtain the yield strength of an elasto-plastic system for a specified ductility factor since the response of a system with arbitrary selected yield strength will seldom correspond to the desired ductility value ([10]).

C.4 Examples of application

In this final part we study some applications related to the construction of both elastic and inelastic spectra. In particular, we study a SDOF system as excited, respectively, by the same base accelerations already considered in Chapter 5:

- Pulse acceleration of intensity 0.5g, period equal to 0.5 seconds and duration of 0.5 seconds.
- Sinusoidal acceleration of intensity 0.2g, period equal to 1 second and duration of 10 seconds.
- Exponential-sinusoidal acceleration of peak ground acceleration of 0.25g and duration of 5 seconds.
- El Centro ground motion.

For each load conditions we present the following plots:

- Ground acceleration, ground velocity and ground displacement, the latter two obtained numerically by integration of the first signal.
- Elastic displacement, pseudo-velocity and pseudo-acceleration response spectra for selected values of damping ratio.
- Relationships between SDOF period and ductility factor for a value of damping ratio equal to 5% according to selected values of yield strength reduction factor.
- Three-dimensional relationships among SDOF period, yield strength reduction factor and displacement response spectra for a value of damping ratio equal to 5%, showed by means of two different graphs.

Construction of elastic response spectrum

1. Numerically define the ground motion $\ddot{u}_g(t)$.
2. Select the natural period of vibration T and damping ratio ξ of a SDOF system.
3. Compute the deformation response *u(t)* of this SDOF system due to the ground motion $\ddot{u}_g(t)$ by using a numerical integration method.
4. Determine u_0, the peak value of *u(t)*.
5. Compute the spectral ordinates using formulas C.4, C.5 and C.6.
6. Repeat steps 2 to 5 for a range of T and ξ values covering all possible systems of engineering interest.
7. Present the results of steps 2 to 6 graphically to produce either three separate spectra or a combined spectrum.

Table C.1: Steps to follow for the construction of elastic response spectrum.

Construction of constant yield reduction factor response spectrum

1. Numerically define the ground motion $\ddot{u}_g$.
2. Select the natural period of vibration T and a value of damping ratio ξ for a SDOF system.
3. Compute the linear deformation response *u(t)* of this SDOF system due to the ground motion $\ddot{u}_g$ by using a numerical integration method.
4. Determine the maximum displacement D, the pseudo-acceleration PSA and the elastic seismic coefficient C_{se} using formulas C.4, C.6 and C.7 respectively.
5. Select an elasto-plastic consitutive model for the SDOF system.
6. Select a value of yield reduction factor R.
7. Compute the inelastic seismic coefficient C_s with formula C.13, the yielding value $f_y = C_s W$ and the yielding displacement $u_y = f_y/k$, being W the weight of the SDOF system.
8. Compute the maximum displacement $D = \max|u(t)|$ and the ductility factor μ.
9. Repeat steps 6 and 7 for a range of R of engineering interest.
10. Repeat steps 1 to 7 for a range of periods of engineering interest.
11. Present the results graphically to produce bi-dimensional (for example T vs.D) or three-dimensional (for example T vs.R vs.D) plots.

Table C.2: Steps to follow for the construction of constant yield reduction factor response spectrum.

Construction of constant ductility response spectrum

1. Numerically define the ground motion $\ddot{u}_g$.
2. Select and fix the damping ratio ξ for which the spectrum is to be plotted.
3. Select a value of T.
4. Determine the response *u(t)* of the linear system with T and ξ equal to the values selected. From *u(t)* determine the peak deformation u_0 and the peak force $f_0 = ku_0$.
5. Determine the response *u(t)* of an elasto-plastic system with the same T and ξ and yield force $f_y = \overline{f}_y f_0$ with a selected $f_y \leq 1$. From *u(t)* determine the peak deformation u_m and the associated ductility factor from equation C.15. Repeat such an analysis for enough values of $\overline{f}_y$ to develop data points $(\overline{f}_y, \mu)$ covering the ductility range of interest.
6. For a selected μ determine the $\overline{f}_y$ value from the results of step 5. If more than one $\overline{f}_y$ value corresponds to a particular value of μ, the largest value of $\overline{f}_y$ is chosen.
7. Determine the spectral ordinates corresponding to the value of $\overline{f}_y$ computed in step 6 from equations C.8, C.9 and C.10.
8. Repeat steps 3 to 6 for a range of T resulting in the spectrum valid for the μ value chosen in step 6.
9. Repeat steps 3 to 8 for several values of μ.
10. Present the results of steps 3 to 9 graphically to produce either three separate spectra or a combined spectrum.

Table C.3: Steps to follow for the construction of constant ductility response spectrum.

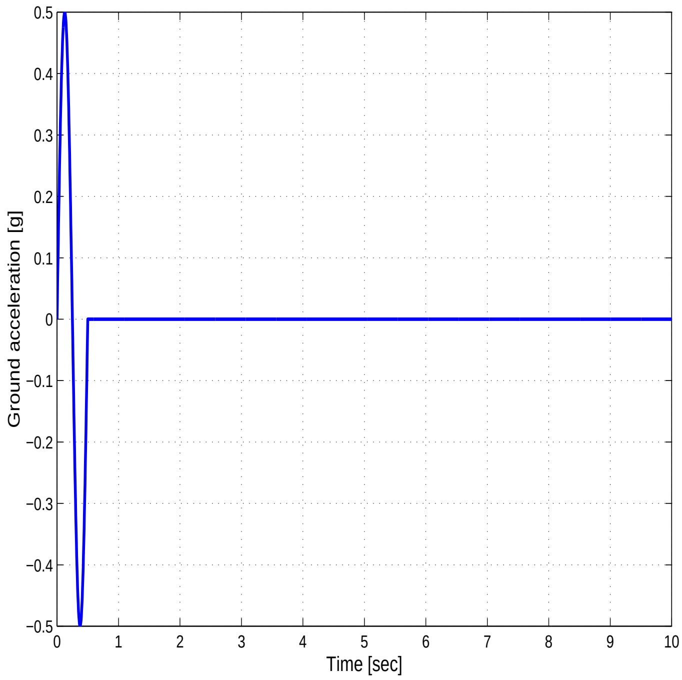

Figure C.1: Acceleration time-history of pulse ground motion.

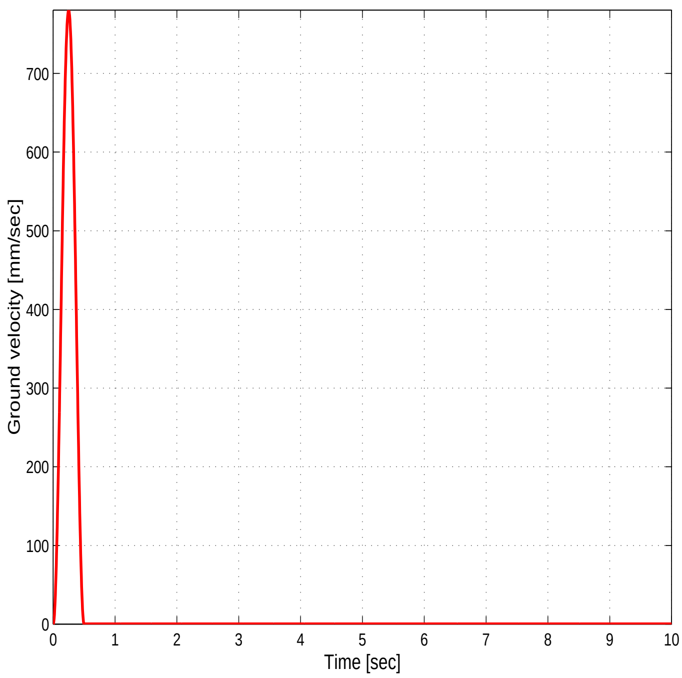

Figure C.2: Velocity time-history of pulse ground motion.

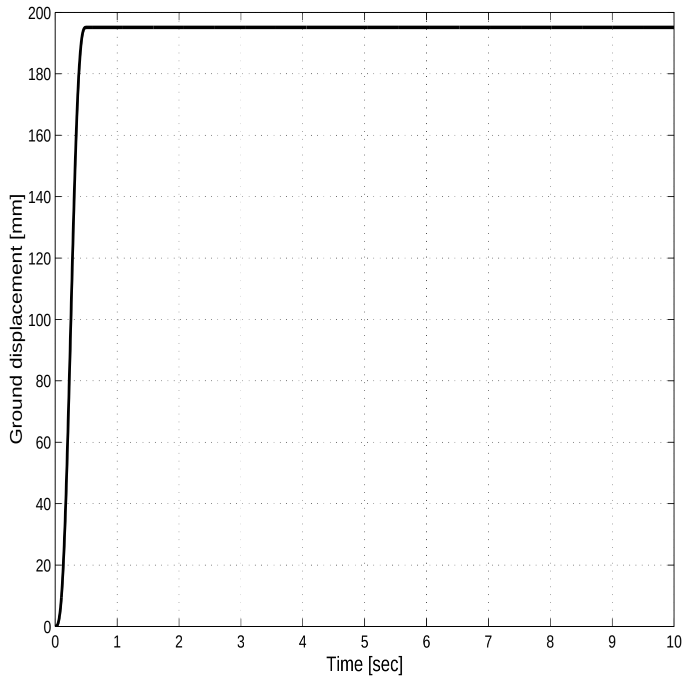

Figure C.3: Displacement time-history of pulse ground motion.

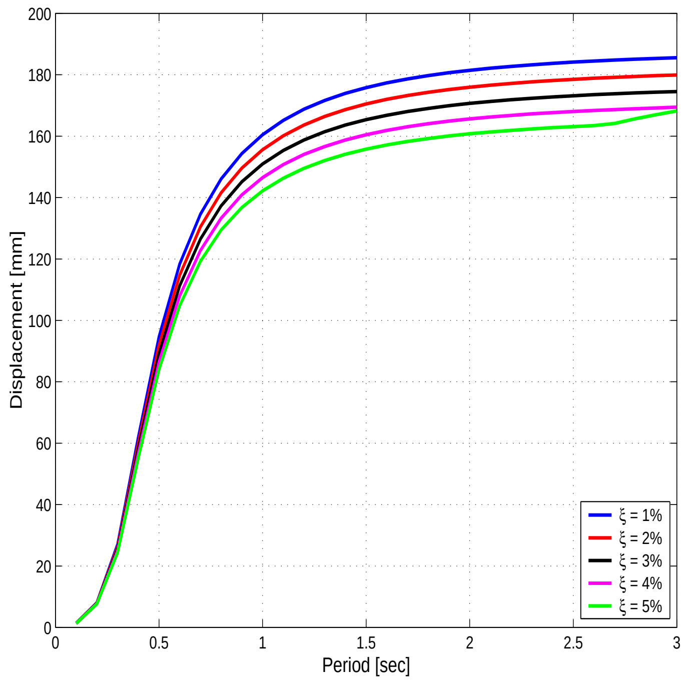

Figure C.4: Elastic deformation response spectrum due to pulse ground motion for selected values of damping ratio.

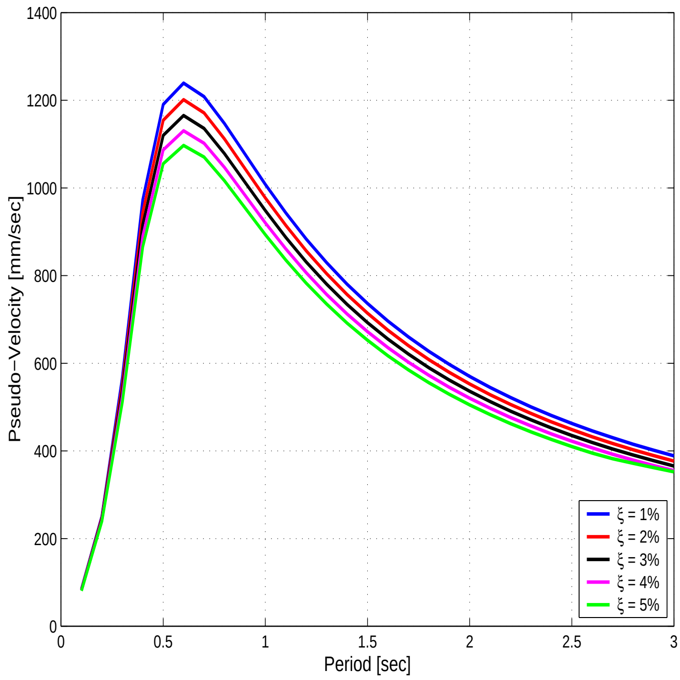

Figure C.5: Elastic pseudo-velocity response spectrum due to pulse ground motion for selected values of damping ratio.

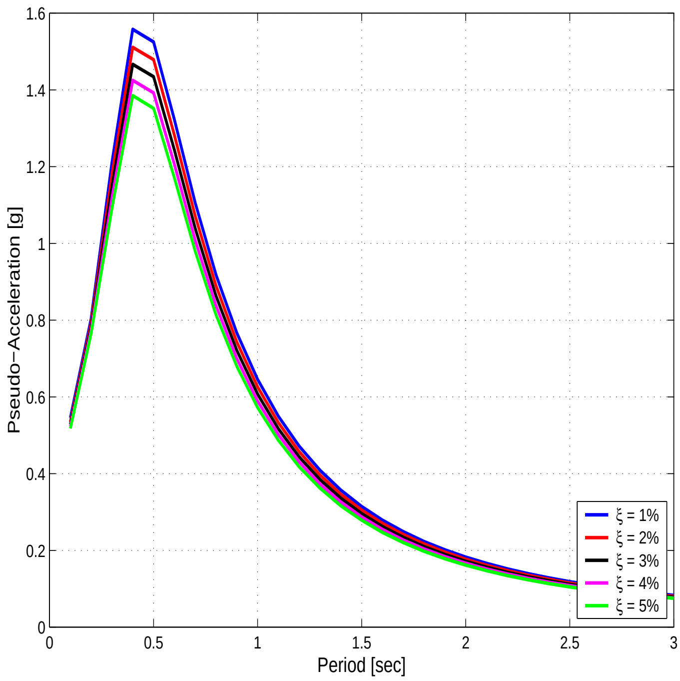

Figure C.6: Elastic pseudo-acceleration spectrum due to pulse ground motion for selected values of damping ratio.

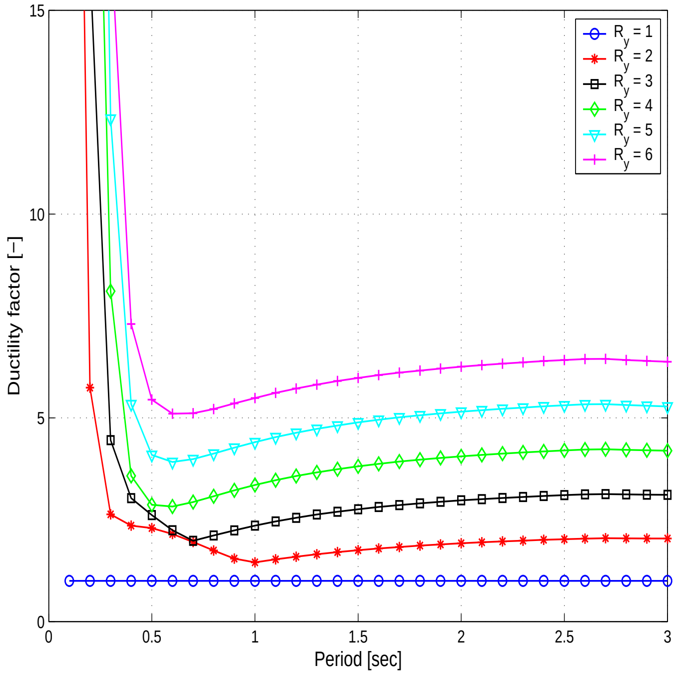

Figure C.7: Ductility demand of elasto-plastic systems due to pulse ground motion as a function of selected values of yield strength reduction factor. The damping ratio is set equal to 5%.

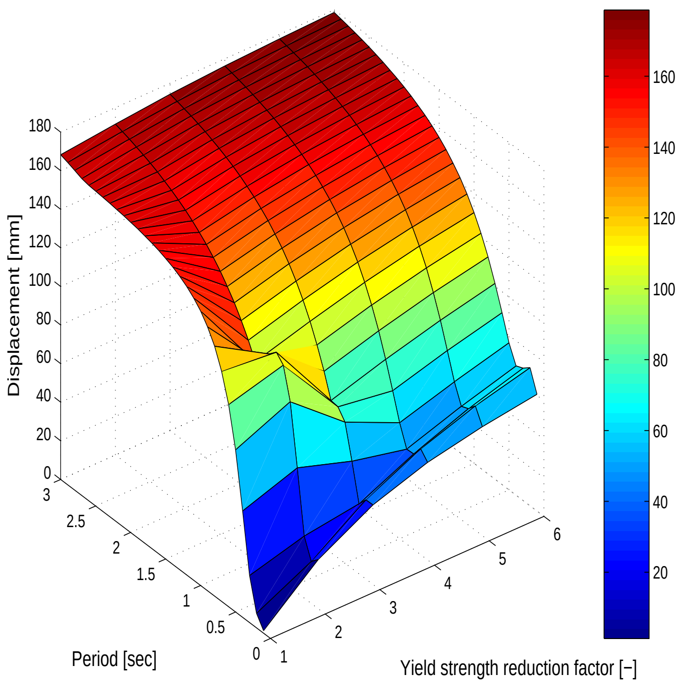

Figure C.8: Displacement spectra of elasto-plastic systems due to pulse ground motion as a function of natural vibration periods and selected values of yield strength reduction factor: 3D perspective view. The damping ratio is set equal to 5%.

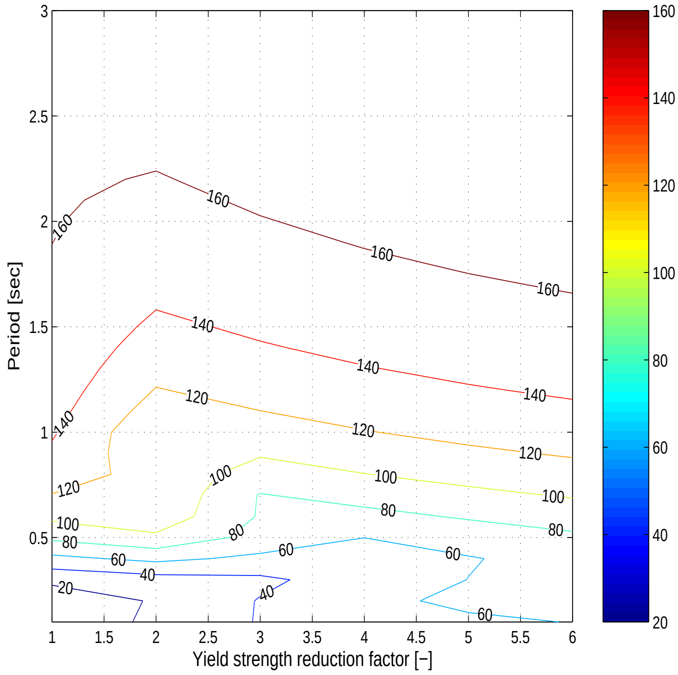

Figure C.9: Displacement spectra of elasto-plastic systems due to pulse ground motion as a function of natural vibration periods and selected values of yield strength reduction factor: contour plot. The damping ratio is set equal to 5%.

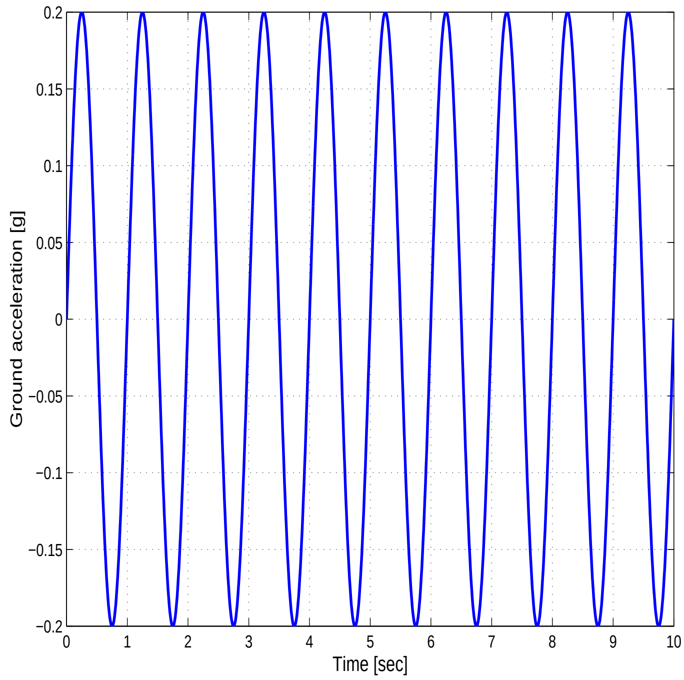

Figure C.10: Acceleration time-history of sinusoidal ground motion.

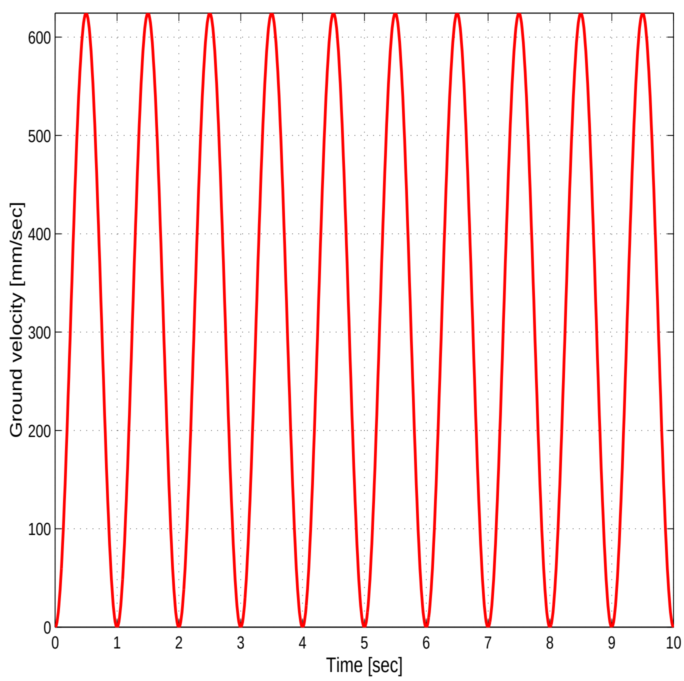

Figure C.11: Velocity time-history of sinusoidal ground motion.

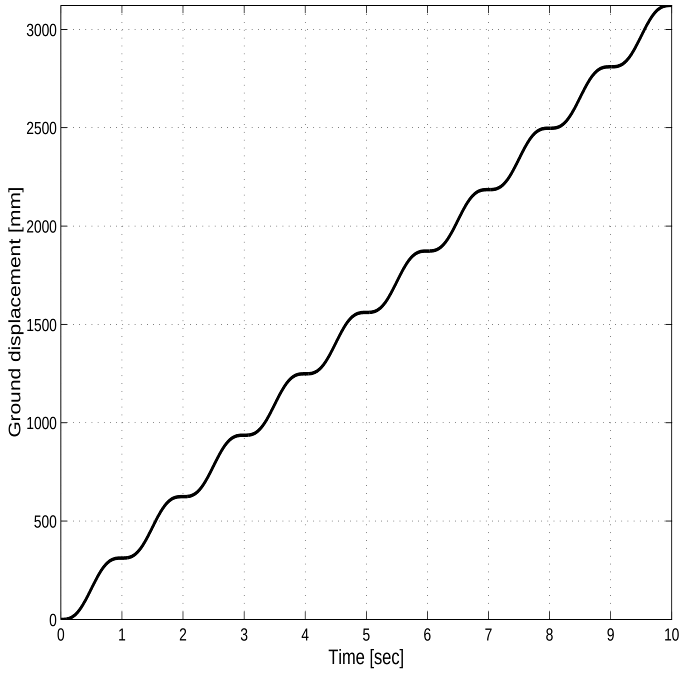

Figure C.12: Displacement time-history of sinusoidal ground motion.

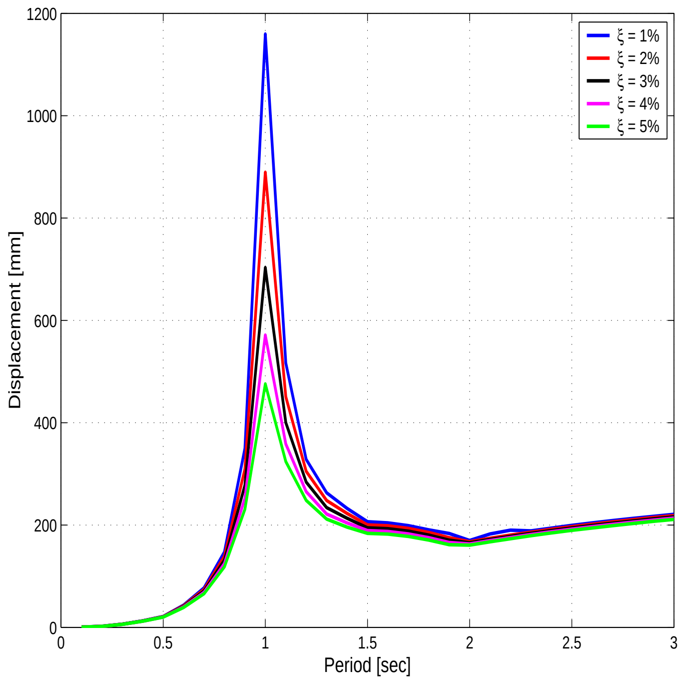

Figure C.13: Elastic deformation response spectrum due to sinusoidal ground motion for selected values of damping ratio.

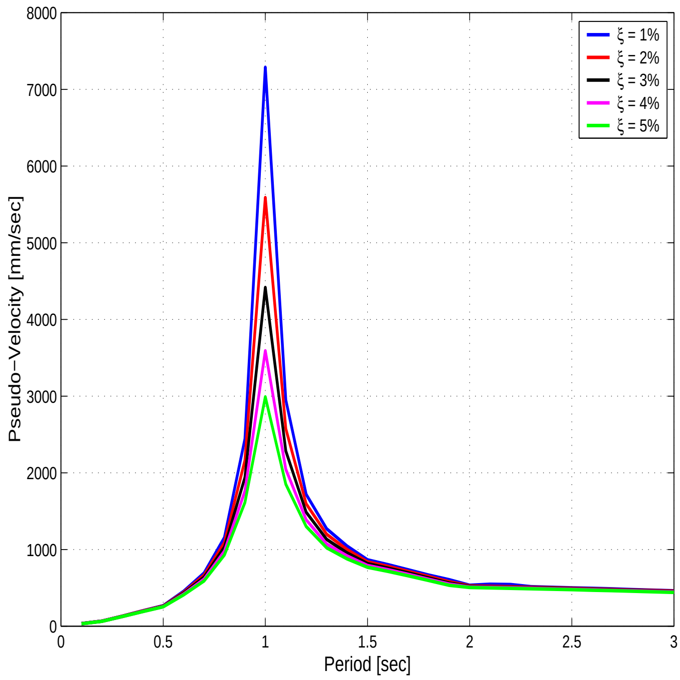

Figure C.14: Elastic pseudo-velocity response spectrum due to sinusoidal ground motion for selected values of damping ratio.

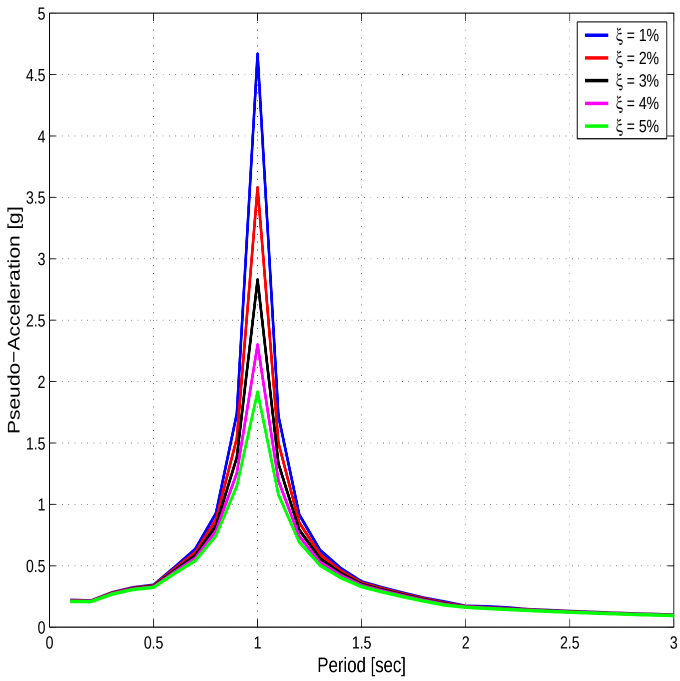

Figure C.15: Elastic pseudo-acceleration spectrum due to sinusoidal ground motion for selected values of damping ratio.

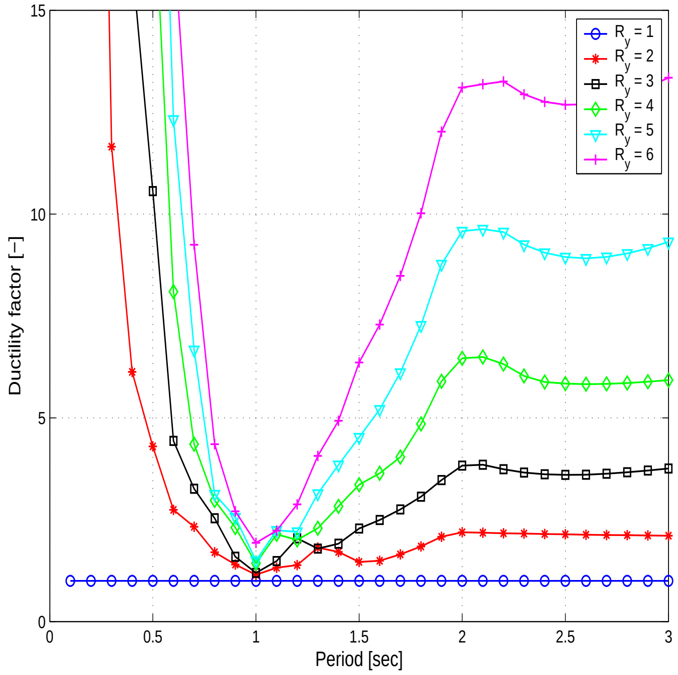

Figure C.16: Ductility demand of elasto-plastic systems due to sinusoidal ground motion as a function of selected values of yield strength reduction factor. The damping ratio is set equal to 5%.

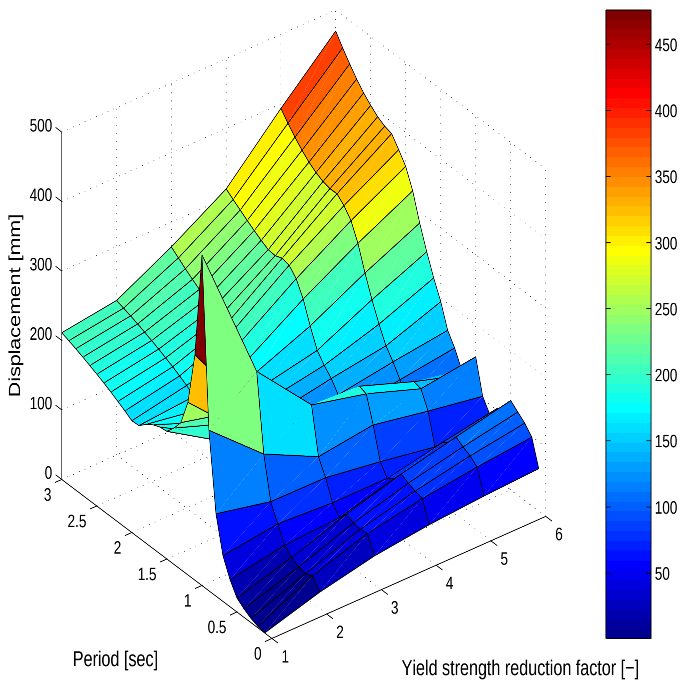

Figure C.17: Displacement spectra of elasto-plastic systems due to sinusoidal ground motion as a function of natural vibration periods and selected values of yield strength reduction factor: 3D perspective view. The value of damping ratio is set equal to 5%.

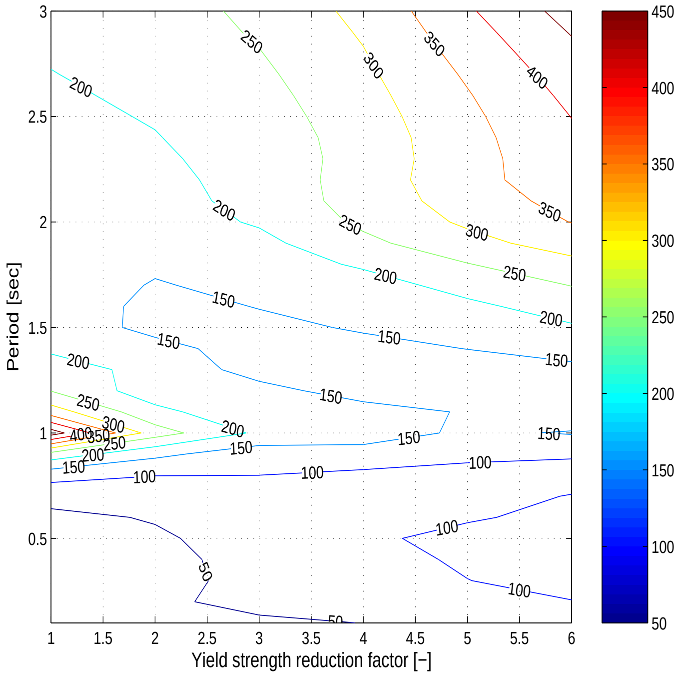

Figure C.18: Displacement spectra of elasto-plastic systems due to sinusoidal ground motion as a function of natural vibration periods and selected values of yield strength reduction factor: contour plot. The damping ratio is set equal to 5%.

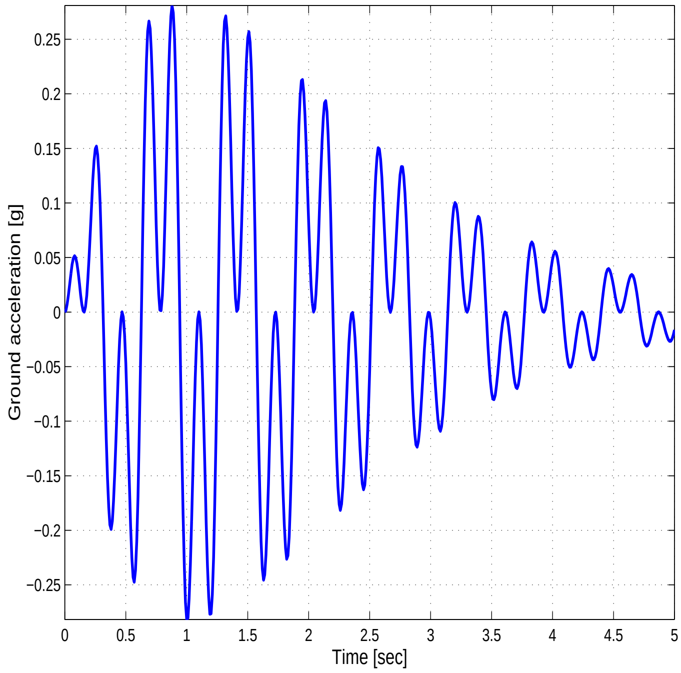

Figure C.19: Acceleration time-history of exponential-sinusoidal ground motion.

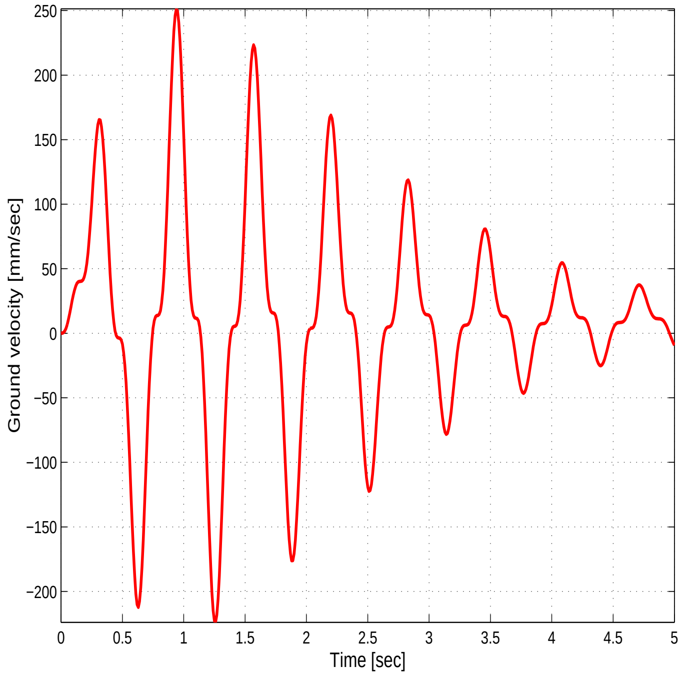

Figure C.20: Velocity time-history of exponential-sinusoidal ground motion.

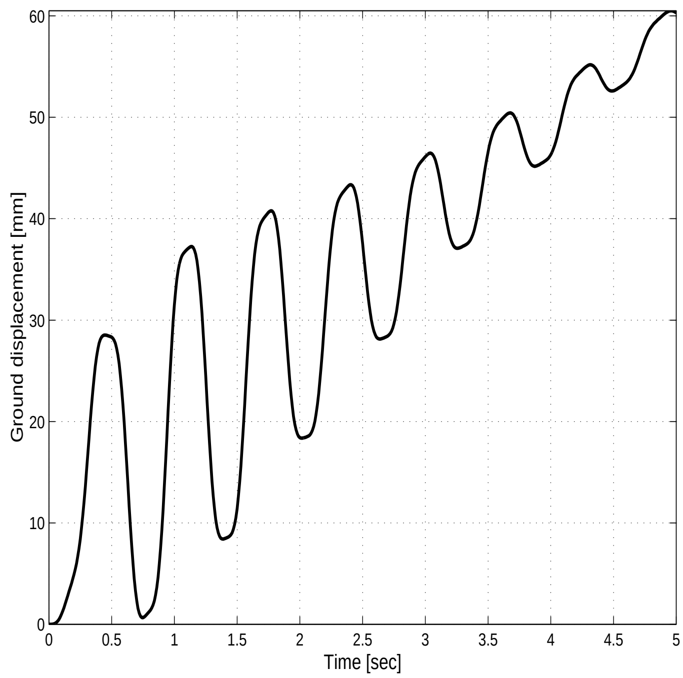

Figure C.21: Displacement time-history of exponential-sinusoidal ground motion.

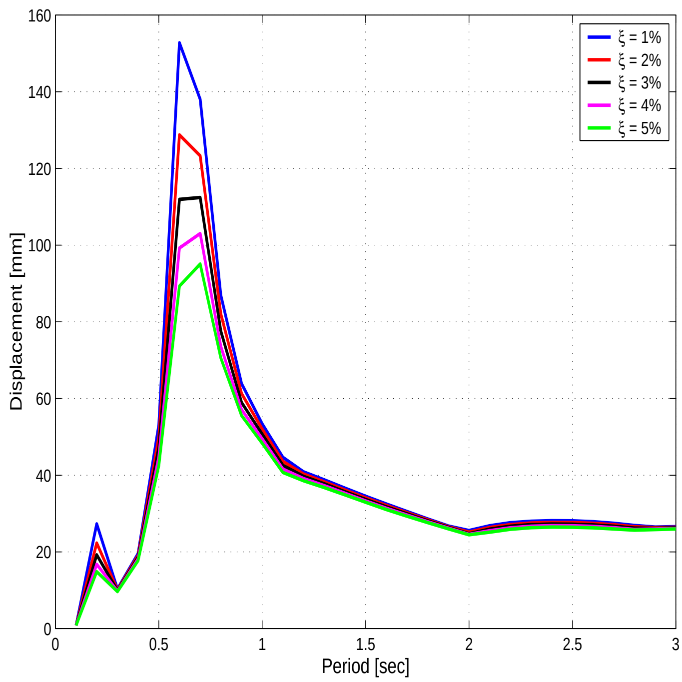

Figure C.22: Elastic deformation response spectrum due to exponential-sinusoidal ground motion for selected values of damping ratio.

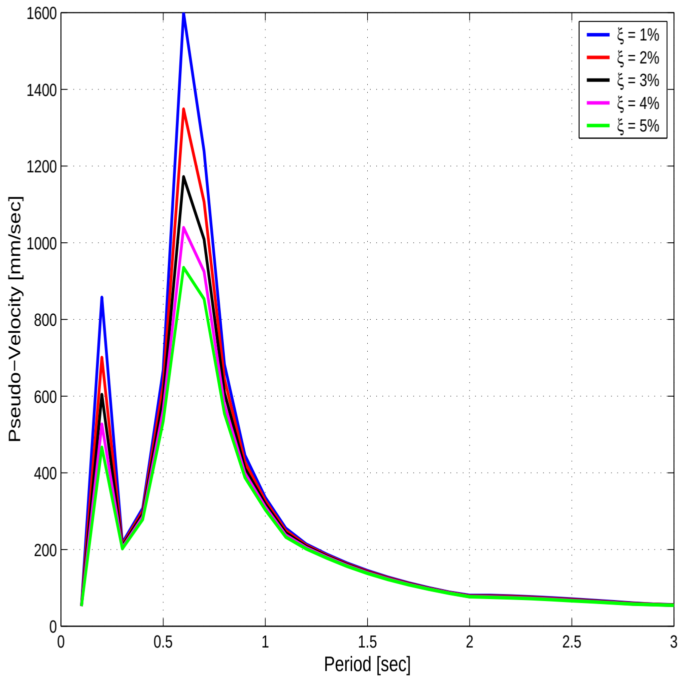

Figure C.23: Elastic pseudo-velocity response spectrum due to exponential-sinusoidal ground motion for selected values of damping ratio.

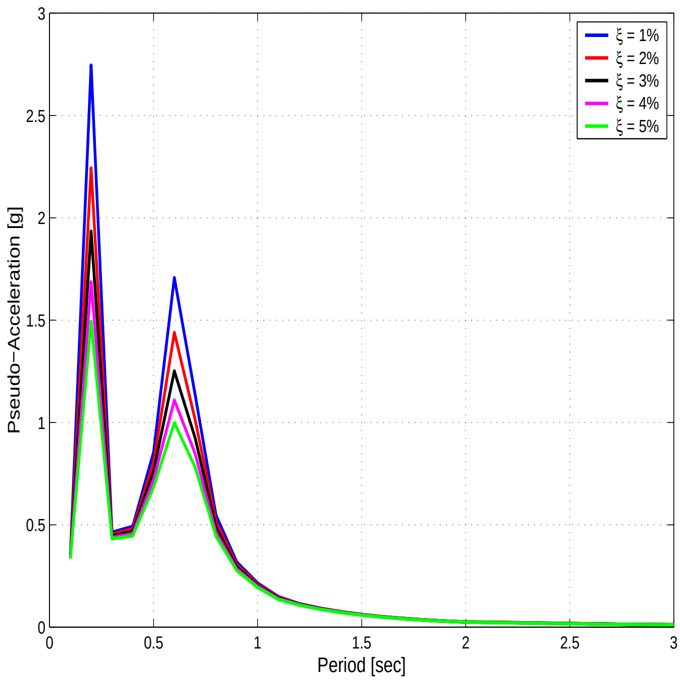

Figure C.24: Elastic pseudo-acceleration spectrum due to exponential-sinusoidal ground motion for selected values of damping ratio.

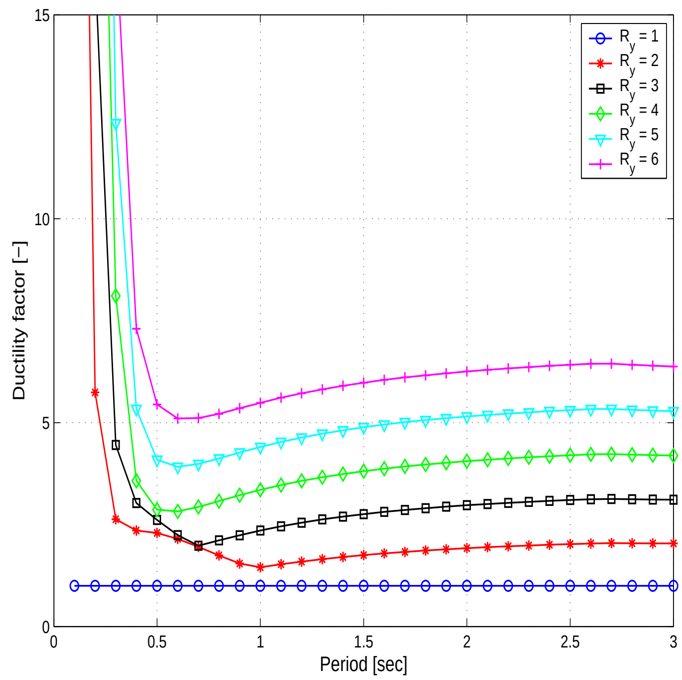

Figure C.25: Ductility demand of elasto-plastic systems due to exponential-sinusoidal ground motion as a function of selected values of yield strength reduction factor. The damping ratio is set equal to 5%.

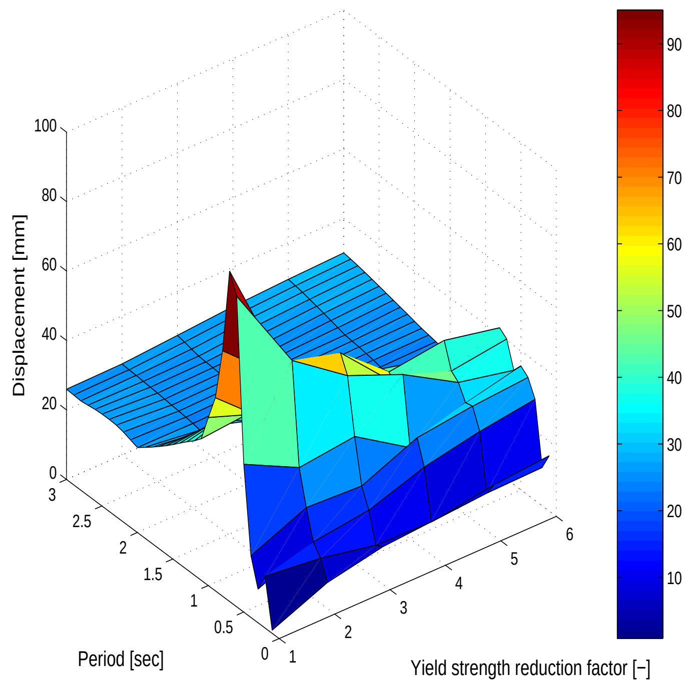

Figure C.26: Displacement spectra of elasto-plastic systems due to exponential-sinusoidal ground motion as a function of natural vibration periods and selected values of yield strength reduction factor: 3D perspective view. The damping ratio is set equal to 5%.

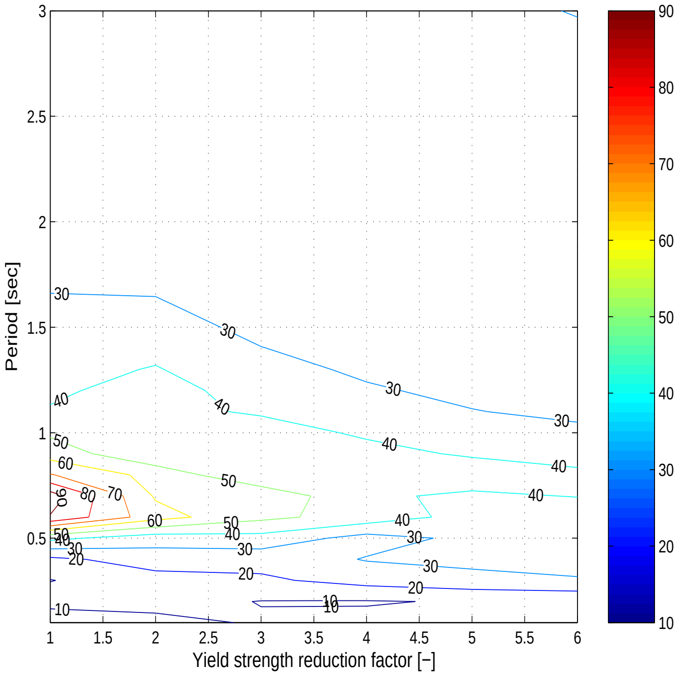

Figure C.27: Displacement spectra of elasto-plastic systems due to exponential-sinusoidal ground motion as a function of natural vibration periods and selected values of yield strength reduction factor: contour plot. The damping ratio is set equal to 5%.

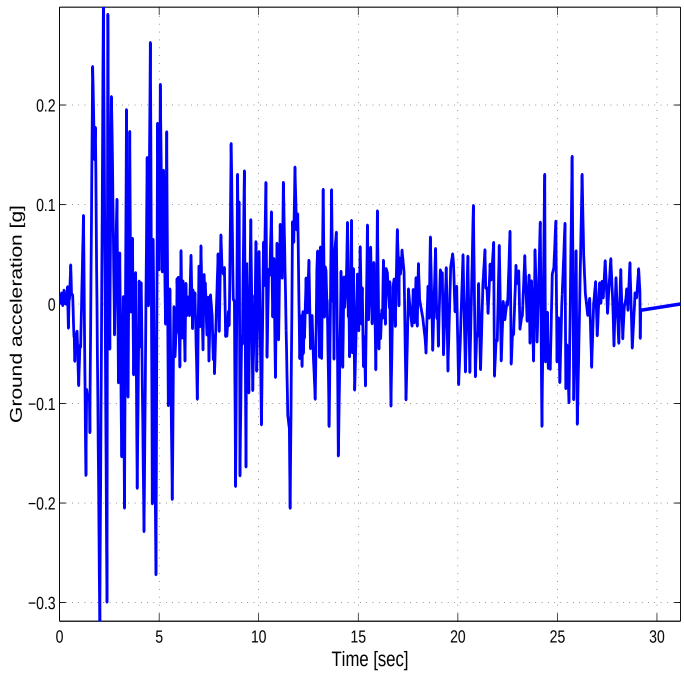

Figure C.28: Acceleration time-history of El Centro ground motion.

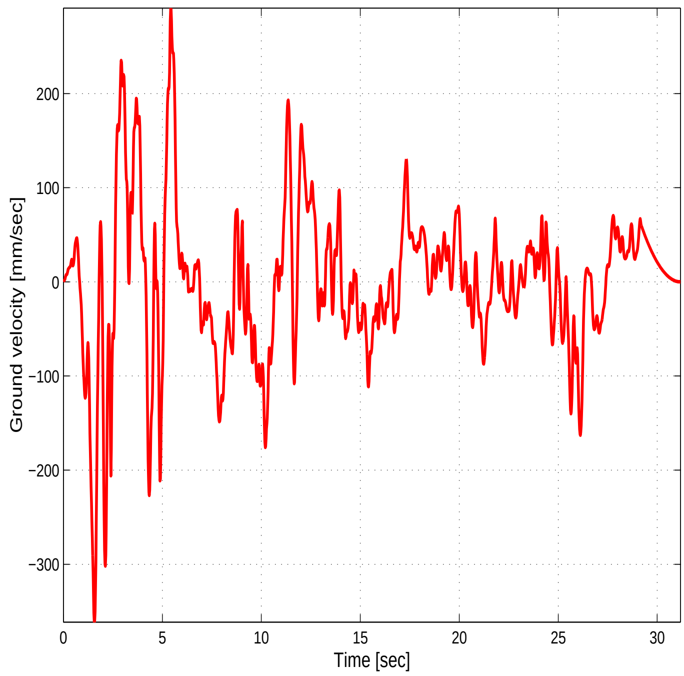

Figure C.29: Velocity time-history of El Centro ground motion.

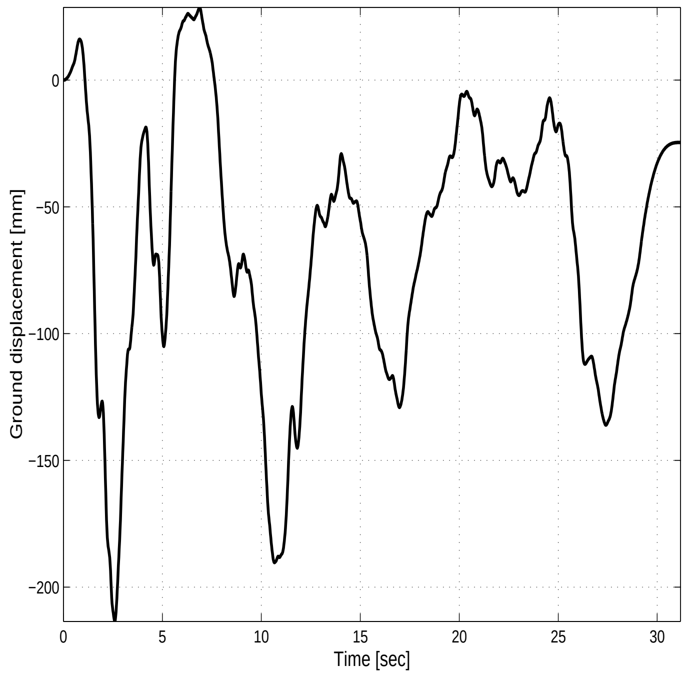

Figure C.30: Displacement time-history of El Centro ground motion.

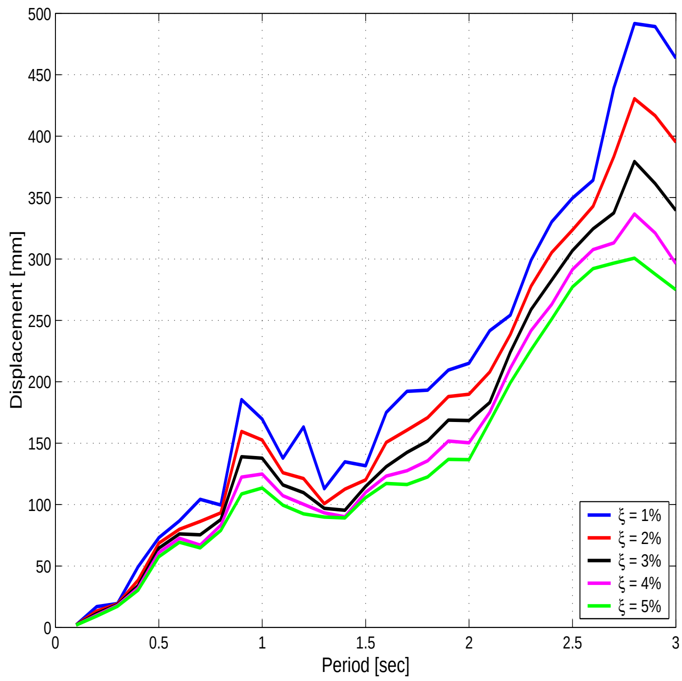

Figure C.31: Elastic deformation response spectrum due to El Centro ground motion for selected values of damping ratio.

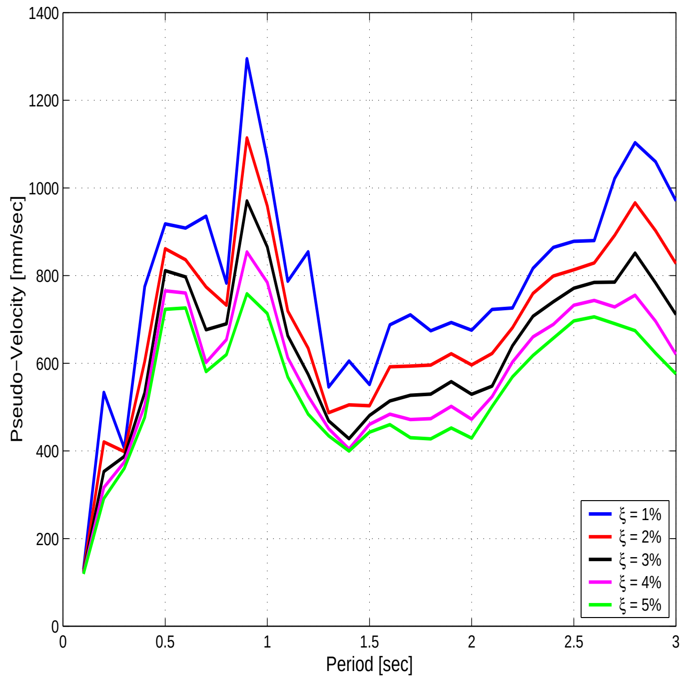

Figure C.32: Elastic pseudo-velocity response spectrum due to El Centro ground motion for selected values of damping ratio.

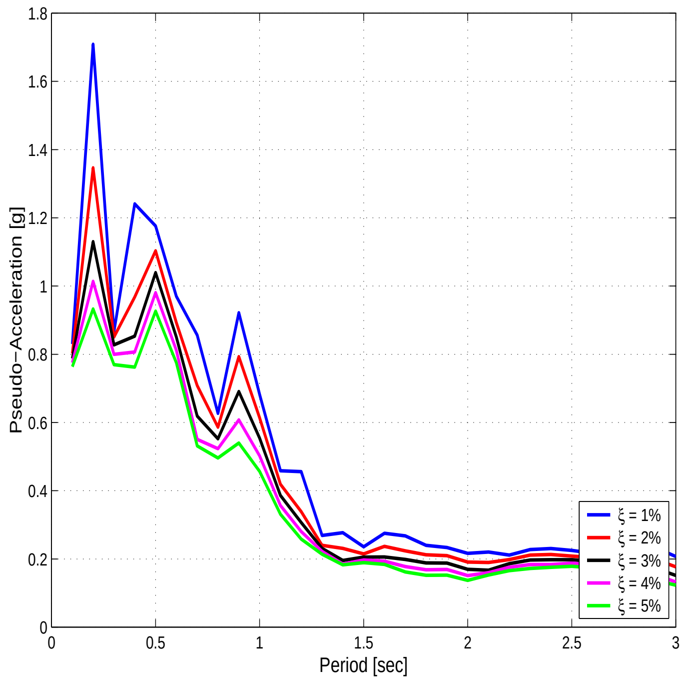

Figure C.33: Elastic pseudo-acceleration response spectrum due to El Centro ground motion for selected values of damping ratio.

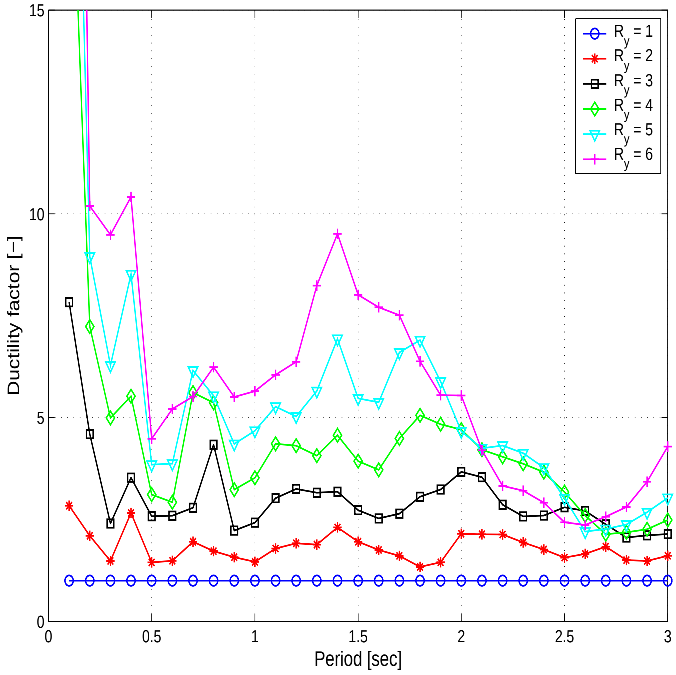

Figure C.34: Ductility demand of elasto-plastic systems due to El Centro ground motion as a function of selected values of yield strength reduction factor. The damping ratio is set equal to 5%.

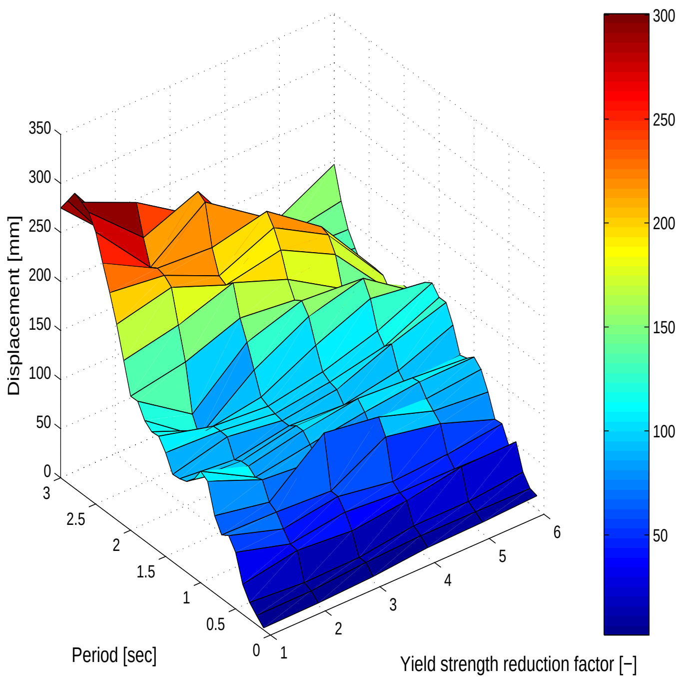

Figure C.35: Displacement spectra of elasto-plastic systems due to El Centro ground motion as a function of natural vibration periods and selected values of yield strength reduction factor: 3D perspective view. The damping ratio is set equal to 5%.

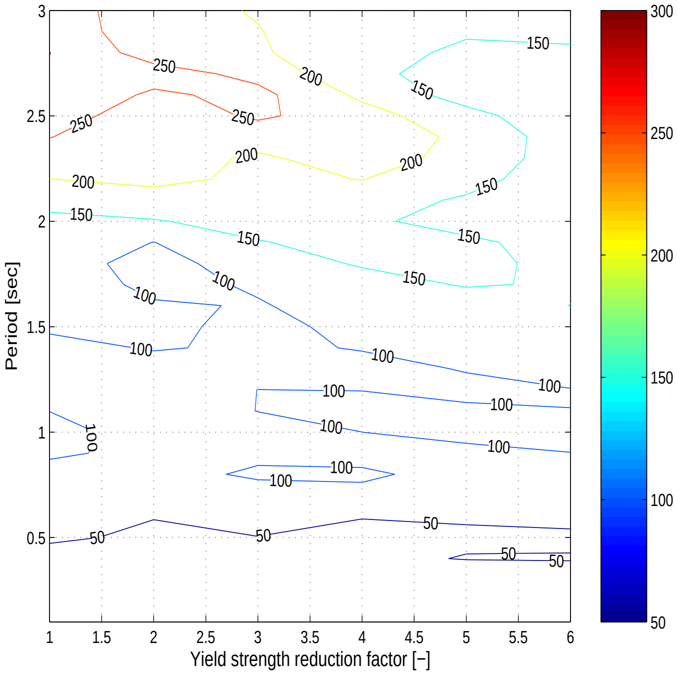

Figure C.36: Displacement spectra of elasto-plastic systems due to El Centro ground motion as a function of natural vibration periods and selected values of yield strength reduction factor: contour plot. The damping ratio is set equal to 5%.

Conclusions

The present dissertation focuses on the possibility of using *shape-memory alloys* as new materials for seismic protection devices.
Despite the large quantity of information concerning their mechanical behavior under static conditions, only in the last few years their capability to attenuate the response of civil engineering structures due to seismic excitations has successfully been demonstrated experimentally.

In the first part of the work a state-of-the-art on the use of SMA-based devices in earthquake engineering is given. In particular, the most promising numerical and experimental applications performed on structures equipped with SMAs have been given and discussed.

Even if in the literature there exists a large number of refined formulation, few works deal with the SMA constitutive modelling for earthquake engineering purposes and a small number of studies examine their response under dynamic loading conditions. As a consequence, the main aim of the present work has been to provide an effort to cover this lack of information. For this reason, a critical overview of the most frequently used material models for seimic applications has been provided. Besides the basic set of equations needed for their implementation into a finite element code, advantages and drawbacks have been highlighted.

A one-dimensional constitutive model for superelastic SMAs has been adopted and implemented. For its characteritics of simplicity and robustness, the presented formulation allows for a detailed investigation of the response of such materials under complex static and dynamic loading paths.

Finally, a large number of parametric analyses have been proposed. Since SMAs may be produced with specific strength characteristics depending on the actual structural needs, mechanical properties, such as stress transformation levels and plateau length, have been intentionally considered as design variables. As a consequence, a large overview of the dynamic performances of such smart materials have been collected and compared. The results confirm that the best use of SMAs in earthquake engineering is for recentring mechanisms since their pseudolastic behavior is effective for very large ranges of deformation. Furthermore, their ability to dissipate energy allows for a reduction of the structural oscillations and their capacity to provide further stiffness after completition of the pseudoelastic phase guarantees good displacement control in case of unexpected strong seismic events. However, an interesting alternative use of SMA-based devices can rely on a combined use with traditional dissipative materials such as steel. In this way, both the recentring and the energy dissipation mechanisms can be activated simultaneously.

Further research is mainly needed in both numerical modelling and experimental investigations.
Refined rate and temperature dependent constitutive models are required to better capture the real behavior of SMAs during seismic events. In this way, it would be possible to improve the accuracy of computational tools to support the design process of SMA-based devices.
Laboratory tests should be aimed at identifying the material behavior under high-frequency rate of loading to really simulate the effect of dynamic excitations. Particular attention should be devoted to temperature effects, which strongly affect the response. Also, the influence of the alloys' chemical composition as well as the specimen size would require particular consideration.

Bibliography

[1] F. Auricchio. *SHAPE MEMORY ALLOYS: micromechanics, macromodeling and numerical simulations*. PhD thesis, Department of Civil and Environmental Engineering, University of California at Berkeley, 1995.

[2] F. Auricchio and E. Sacco. A one-dimensional model for superelastic shape-memory alloys with different elastic properties between martensite and austenite. *International Journal of Non-Linear Mechanics*, 32:1101–1114, 1997.

[3] A. Baratta and O. Corbi. On the dynamic behaviour of elastic-plastic structures equipped with pseudoelastic sma reinforcements. *Computational Materials Science*, 25:1–13, 2002.

[4] C. Barns. Shape Memory and Superelastic Alloys. http://www.copper.org.

[5] D. Bernardini and F. Brancaleoni. Shape memory alloys modelling for seismic applications. *Atti del MANSIDE Project - Final Workshop - Memory Alloys for Seismic Isolation and Energy Dissipation Devices*, pages 73–84, part II, 1999.

[6] D. Bernardini and F. Vestroni. Non-isothermal oscillations of pseudoelastic devices. *International Journal of Non-Linear Mechanics*, 38:1297–1313, 2003.

[7] L. C. Brinson. One-dimensional constitutive behavior of shape memory alloys: thermomechanical derivation with non-constant material functions and redefined internal variable. *Journal of Intelligent Material Systems and Structures*, 3:229–242, 1993.

[8] S. Bruno and C. Valente. Comparative response analysis of conventional and innovative seismic protection strategies. *Earthquake Engineering and Structural Dynamics*, 31:1067–1092, 2002.

[9] D. Cardone, M. Dolce, A. Bixio, and D. Nigro. Experimental tests on SMA elements. *Atti del MANSIDE Project - Final Workshop - Memory Alloys for Seismic Isolation and Energy Dissipation Devices*, pages 85–104, part II, 1999.

[10] A. K. Chopra. *Dynamics of Structures: theory and applications to earthquake engineering.* Prentice Hall, 2000.

[11] R. W. Clough and J. Penzien. *Dynamics of Structures.* McGraw-Hill, 1993.

[12] M. Collet, E. Foltete, and C. Lexcellent. Analysis of the behavior of a shape memory alloy beam under dynamical loading. *European Journal of Mechanics and Solids*, pages 615–630, 2001.

[13] O. Corbi. Shape memory alloys and their application in structural oscillations attenuation.

[14] R. DesRoches and M. Delemont. Seismic retrofit of simply supported bridges using shape memory alloys. *Engineering Structures*, 24:325–332, 2003.

[15] R. DesRoches, R. Leon, G. Hess, and J. Ocel. Seismic design and retrofit using shape memory alloys.

[16] R. DesRoches, J. McCormick, and M. Delemont. Cyclic properties of shape memory alloy wires and bars. *In press on the ASCE Journal of Structural Engineering*, August 2002.

[17] R. DesRoches and B. Smith. Shape memory alloys in seismic resistant design and retrofit: a critical review of the state of the art, potential and limitations. *In press on the Journal of Earthquake Engineering*, August 2002.

[18] M. Dolce and D. Cardone. Mechanical behaviour of shape memory alloys for seismic applications 1. Martensite and austenite bars subjected to torsion. *International Journal of Mechanical Sciences*, 43:2631–2656, 2001.

[19] M. Dolce and D. Cardone. Mechanical behaviour of shape memory alloys for seismic applications 2. Austenite niti wires subjected to tension. *International Journal of Mechanical Sciences*, 43:2657–2677, 2001.

[20] M. Dolce, D. Cardone, and R. Marnetto. Implementation and testing of passive control devices based on shape memory alloys. *Earthquake Engineering and Structural Dynamics*, 29:945–968, 2000.

[21] M. Dolce, M. Nicoletti, and F. C. Ponzo. Protezione sismica con dispositivi basate sulle leghe a memoria di forma: il progetto MANSIDE e gli ulteriori sviluppi. *Ingegneria Sismica*, 1:66–78, 2001.

[22] T. W. Duerig, K. N. Melton, and C. M. Wayman. *Engineering aspects of shape memory alloys.* Butterworth-Henemann Ltd, London, 1990.

[23] Z. C. Feng and D. Z. Li. Dynamics of a mechanical system with a shape memory alloy bar. *Journal of Intelligent Material Systems and Structures*, 7:399–410, 1996.

[24] E. J. Graesser and F. A. Cozzarelli. Shape-memory alloys as new materials for aseismic isolation. *Journal of Engineering Mechanics*, 117:2590–2608, 1991.

[25] E. J. Graesser and F. A. Cozzarelli. A proposed three-dimensional constitutive model for shape memory alloys. *Journal of Intelligent Material Systems and Structures*, 5:78–89, 1994.

[26] Yu-Lin Han, Q. S. Li, Ai-Qun Li, A. Y. Y. Leung, and Ping-Hua Lin. Structural vibration control by shape memory alloy damper. *Earthquake Engineering and Structural Dynamics*, 32:483–494, 2003.

[27] O. Heintze and S. Seelecke. Interactive www page for the simulation of shape memory alloys, http://www.mae.ncsu/homepages/seelecke, 2000.

[28] T. J. R. Hughes. *The Finite element Method: linear static and dynamic finite element analysis*. Dover, 2000.

[29] J. Van Humbeeck. General aspects of shape memory alloys. *Atti del MANSIDE Project - Final Workshop - Memory Alloys for Seismic Isolation and Energy Dissipation Devices*, pages 9–44, part II, 1999.

[30] J. Van Humbeeck. Non-medical applications of shape memory alloys. *Materials Science and Engineering*, pages 134–148, A273–275, 1999.

[31] Y. Ivshin and T. J. Pence. A thermomechanical model for a one variant shape memory material. *Journal of Intelligent Material Systems and Structures*, 5:455–473, 1994.

[32] Johnson Matthey. http://www.jmmedical.com.

[33] M. M. Khan and D. C. Lagoudas. Modeling of shape memory alloy pseudoelastic spring elements using preisach model for passive vibration isolation.

[34] D. C. Lagoudas, J. J. Mayes, and M. M. Khan. Simplified shape memory alloy (SMA) material model for vibration isolation.

[35] D. C. Lagoudas, J. J. Mayes, and M. M. Khan. Modelling of shape memory alloy springs for passive vibration isolation. *Proceedings of IMECE 2001, 2001 International Mechanical Engineering Congress and Exposition*, November 11-16, 2001, New York, New York, USA.

[36] C. Liang and C. A. Rogers. Design of shape memory alloy coils and their applications in vibration control.

[37] C. Liang and C. A. Rogers. One-dimensional thermomechanical constitutive relations for shape memory materials. *Journal of Intelligent Material Systems and Structures*, 1:207–234, 1990.

[38] C. Liang and C. A. Rogers. Design of shape memory alloy springs with applications in vibration control. *Journal of Intelligent Material Systems and Structures*, 8:314–322, 1997.

[39] T. J. Lim and D. L. McDowell. Path dependence of shape memory alloys during cyclic loading. *Journal of Intelligent Material Systems and Structures*, 6:817–830, 1995.

[40] A. Masuda and M. Noori. Optimization of hysteretic characteristics of damping devices based on pseudoelastic shape memory alloys. *International Journal of Non-Linear Mechanics*, 6:817–830, 1995.

[41] J. J. Mayes, D. C. Lagoudas, and B. K. Anderson. An experimental investigation of shape memory alloy springs for passive vibration isolation. *AIAA Space 2001 Conference and Exposition*, August 28-30, 2001, Albuquerque, NM.

[42] F. M. Mazzolani and A. Mandara. Modern trends in the use of special metals for the improvement of historical and monumental structures. *Engineering Structures*, 24:843–856, 2002.

[43] Memory-Metalle GmbH. http://www.memory-metalle.de.

[44] Memry Corporation. http://www.memry.com.

[45] M. O. Moroni, R. Saldivia, M. Sarrazin, and A. Sepulveda. Damping characteristics of a CuZnAlNi shape memory alloy. *Materials Science and Engineering*, pages 313–319, A335, 2002.

[46] Nitinol Devices and Components (NDC). http://www.nitinol.com.

[47] J. Ocel. Steel connections utilizing shape memory alloys. *A Report presented to the Mid-America Earthquake Center as requirement of REU Program*, August 2000.

[48] J. Ocel, R. DesRoches, R. T. Leon, W. G. Hess, R. Krumme, J. R. Hayes, and S. Sweeney. Steel beam-column connections using shape memory alloys. *In press on the ASCE Journal of Structural Engineering*, July 2002.

[49] T. J. Pence. Mathematical modelling of shape memory alloys. *Atti del MANSIDE Project - Final Workshop - Memory Alloys for Seismic Isolation and Energy Dissipation Devices*, pages 45–58, part II, 1999.

[50] M. C. Piedboeuf and R. Gauvin. Damping behaviour of shape memory alloys: strain amplitude, frequency and temperature effects. *Journal of Sound and Vibration*, 214:885–901, 1998.

[51] S. Seelecke. Modeling the dynamic behavior of shape memory alloys. *International Journal of Non-Linear Mechanics*, 37:1363–1374, 2002.

[52] Shape Memory Applications Inc.. http://www.sma-inc.com.

[53] Special Metals Corporation. http://www.specialmetals.com.

[54] B. Strnadel, S. Ohashi, H. Ohtsuka, T. Ishihara, and S. Miyazaki. Cyclic stress-strain characteristics of ti-ni and ti-ni-cu shape memory alloys. *Materials Science and Engineering*, pages 148–156, A202, 1995.

[55] H. Tamai and Y. Kitagawa. Pseudoelastic behavior of shape memory alloy wire and its application to seismic resistance member for building. *Computational Materials Science*, 25:218–227, 2002.

[56] The A to Z of Materials (AZoM). http://www.azom.com.

[57] H. Tobushi, Y. Shimeno, T. Hachisuka, and K. Tanaka. Influence of strain rate on superelastic properties of tini shape memory alloy. *Mechanics of Materials*, 30:141–150, 1998.

[58] Berlin Technical University. http://www.thermodynamik.tu-berlin.de.

[59] C. Valente, D. Cardone, B. G. Lamonaca, and F. M. Ponzo. Shaking table tests of structures with conventional and sma based protection devices. *Atti del MANSIDE Project - Final Workshop - Memory Alloys for Seismic Isolation and Energy Dissipation Devices*, pages 177–194, part II, 1999.

[60] K. Wilde, P. Gardoni, and Y. Fujino. Base isolation system with shape memory alloy device for elevated highway bridges. *Engineering Structures*, 22:222–229, 2000.

[61] D. Wolons, F. Gandhi, and B. Malovrh. Experimental investigation of the pseudoelastic hysteresis damping characteristics of shape memory alloy wires. *Journal of Intelligent Material Systems and Structures*, 9:116–126, 1998.